Available online at www.sciencedirect.com
SCIENCE DIRECT
ELSEVIER
Earth-Science Reviews 74 (2006) 127–196
EARTH-SCIENCE REVIEWS
www.elsevier.com/locate/earscirev

Neotectonics and intraplate continental topography of the northern Alpine Foreland

S. Cloetingh [a,*], T. Cornu [a], P.A. Ziegler [b], F. Beekman [a]

Environmental Tectonics (ENTEC) Working Group[1]

[a] *Netherlands Research Centre for Integrated Solid Earth Sciences, Faculty of Earth and Life Sciences, Vrije Universiteit, De Boelelaan 1085, 1081 HV Amsterdam, The Netherlands*
[b] *Department of Earth Sciences, University of Basel, Bernoullistrasse 32, 4056 Basel, Switzerland*
[c] *Department of Geological Sciences, Geo-Center, University of Vienna, Althanstrasse 14, 1090 Vienna, Austria*
[d] *Ecole et Observatoire des Sciences de la Terre, Institut de Physique du Globe de Strasbourg, 5 rue René Descartes, 67084 Strasbourg, France*
[e] *Geologisches Institut, Albert Ludwigs Universität, Freiburg i.Br., Albertstrasse 23-B, 79104 Freiburg i.Br., Germany*
[f] *Netherlands Institute of Applied Geosciences, Princetonlaan 63584 CB Utrecht, The Netherlands*
[g] *Geodätisches Institut, Universität Fredericiana Karlsruhe, Englerstrasse 7, 76128 Karlsruhe, Germany*
[h] *Geodesy and Geodynamics Laboratory, ETH-Hönggerberg HPV G53, 8093 Zürich, Switzerland*
[i] *Bureau de Recherches Geologiques et Minières, Land Use Planning and Natural Risk Division, 3 Avenue Claude Guillemin, 45060 Orléans, France*
[j] *Royal Netherlands Meteorological Institute (KNMI), P.O. Box 201, 3730AE De Bilt, The Netherlands*

Received 1 July 2004; accepted 2 June 2005
Available online 4 January 2006

Abstract

Research on neotectonics and related seismicity has hitherto been mostly focused on active plate boundaries that are characterized by generally high levels of earthquake activity. Current seismic hazard estimates for intraplate domains are mainly based on probabilistic analyses of historical and instrumental earthquake catalogues. The accuracy of such hazard estimates is limited by the fact that available catalogues are restricted to a few hundred years, which, on geological time scales, is insignificant and not suitable for the assessment of tectonic processes controlling the observed earthquake activity. More reliable hazard prediction requires access to high quality data sets covering a geologically significant time span in order to obtain a better understanding of processes controlling on-going intraplate deformation.

The Alpine Orogen and the intraplate sedimentary basins and rifts in its northern foreland are associated with a much higher level of neotectonic activity than hitherto assumed. Seismicity and stress indicator data, combined with geodetic and geomorphologic observations, demonstrate that deformation of the Northern Alpine foreland is still on-going and will continue in the future. This has major implications for the assessment of natural hazards and the environmental degradation potential of this densely populated area. We examine relationships between deeper lithospheric processes, neotectonics and surface processes in the northern Alpine Foreland, and their implications for tectonically induced topography.

* Corresponding author.
E-mail address: sierd.cloetingh@falw.vu.nl (S. Cloetingh).

[1] Members of the Environmental Tectonics (ENTEC) Working Group: K. Ustaszewski[b], S.M. Schmid[b], P. Dèzes[b], R, Hinsch[c], K, Decker[c], G. Lopes Gardozo[d], M. Granet[d], G. Bertrand[e], J. Behrmann[e], R. van Balen[af], L. Michon[f], H. Pagnier[f], S. Rozsa[g], B. Heck[g], M. Tesauro[ah], H.G. Kahle[h], T. Dewez[i], S. Carretier[i], T. Winter[i], N. Hardebol[a], G. Bada[a], B. Dost[j], T. van Eck[j].

0012-8252/$ - see front matter
doi:10.1016/j.earscirev.2005.06.001

For the Environmental Tectonics Project (ENTEC), the Upper and Lower Rhine Graben (URG and LRG) and the Vienna Basin (VB) were selected as natural laboratories. The Vienna Basin developed during the middle Miocene as a sinistral pull-apart structure on top of the East Alpine nappe stack, whereas the Upper and Lower Rhine grabens are typical intracontinental rifts. The Upper Rhine Graben opened during its Late Eocene and Oligocene initial rifting phase by nearly orthogonal crustal extension, whereas its Neogene evolution was controlled by oblique extension. Seismic tomography suggests that during extension the mantle-lithosphere was partially decoupled from the upper crust at the level of the lower crust. However, whole lithospheric folding controlled the mid-Miocene to Pliocene uplift of the Vosges–Black Forest Arch, whereas thermal thinning of the mantle–lithosphere above a mantle plume contributed substantially to the past and present uplift of the Rhenish Massif. By contrast, oblique crustal extension, controlling the late Oligocene initial subsidence stage of the Lower Rhine Graben, gave way to orthogonal extension at the transition to the Neogene.

The ENTEC Project integrated geological, geophysical, geomorphologic, geodetic and seismological data and developed dynamic models to quantify the societal impact of neotectonics in areas hosting major urban and industrial activity concentrations. The response of Europe's intraplate lithosphere to Late Neogene compressional stresses depends largely on its thermo-mechanical structure, which, in turn, controls vertical motions, topography evolution and related surface processes.

Keywords: neotectonics; intraplate deformation; seismicity; topography; European continental rift system; geomorphology

1. Introduction

The dynamics of the Earth system are controlled by a spectrum of processes that operate at a variety of spatial and temporal scales. Reliable prediction of Earth system dynamics in a given area requires a thorough understanding of processes controlling deformation of the lithosphere. This demands the availability of high-quality multi-disciplinary data sets on the basis of which processes can be analysed, identified and verified by data-interactive modelling. The main progress in quantitative geoprediction is expected at the interface between observation and modelling.

The physical shape of the landscape is a sensitive recorder of the interaction between processes taking place in the deep earth, on its surface and in the atmosphere above it. Topography influences society not only in the slow process of landscape change, but also through climate. The present state and behaviour of the shallow Earth system is a consequence of processes operating on a wide range of time scales. These include, amongst others, the long-term tectonic effects of uplift and subsidence and their repercussions on the development of river systems (e.g. Cloetingh and Cornu, 2005). Research will need to focus on the interplay between active tectonics, topographic evolution, related sea level changes and development of the drainage system (river). This includes developing an integrated strategy for observation and analysis, emphasizing large scale changes in vulnerable parts of the globe.

Topography is not only a recorder of deformation but also a source of stress in the lithosphere (e.g. Bada et al., 2001), and plays an important role in the identification of future earthquake sources, using morpho-structural criteria (Gorshkov et al., 2000, 2004; Peresan et al., 2002). Topographic features, such as the elevation and orientation of large landforms and their lateral variation, drainage patters, linear topographic elements, such as rivers, ravines, escarpments, bottom edges of the slopes of terraces and valleys, all have a bearing on mass transfer at the surface of the Earth, and resulting differential vertical motions of the lithosphere caused by its erosional unloading or depositional loading. Moreover, topography preferentially develops at sites where differently oriented block boundaries intersect that are associated with intense fracturing and contrasting neotectonic movements. The link between topography and seismicity is currently an area of active research (e.g. Gorshkov et al., 2000, 2004; Behrmann et al., 2005).

A much higher level of neotectonic activity than hitherto assumed characterizes the Alpine Orogen and the intraplate sedimentary basins and rifts of its northern foreland. Seismicity and stress indicators, combined with geodetic and geomorphologic observations, demonstrate that the northern Alpine foreland is tectonically still active and subject to on-going deformation (Nivière and Winter, 2000). This realization has major implications for the assessment of the natural hazard and environmental degradation potential of Northwest Europe. The lithosphere of this area has undergone a polyphase evolution in which the interplay of stress-induced intraplate deformation (Müller et al., 1992; Ziegler et al., 1995, 2002) and upper mantle thermal perturbations (Granet et al., 1995; Goes et al., 2000a) played an important role (Ziegler et al., 2004; Dèzes et al., 2004). Moreover, recent findings indicate that, apart from stress-induced reactivation of pre-existing crustal discontinuities (Ziegler, 1990; Ziegler et al., 1995),

folding of the thermally weakened Northwest European lithosphere contributed significantly to the spectrum of intraplate deformations (Cloetingh and Burov, 1996; Cloetingh et al., 1999; Dèzes et al., 2004).

The natural laboratory concept is fundamental for the assessment of neotectonic deformations and related environmental implications, as it fosters the dialogue between traditional observational and newly developed dynamic modelling approaches. Natural laboratories are selected to address specific hazard and environmental problems in areas for which an extensive, multidisciplinary database is available or can be acquired. In the context of the Environmental Tectonics (ENTEC) network, which addressed the on-going deformation of the Northern Alpine foreland, the Upper and Lower Rhine Graben (URG and LRG) and the Vienna Basin (VB) were selected as natural laboratories (Fig. 1). These neotectonically active areas offered massive bodies of hitherto not yet integrated geological and geophysical data that could be complemented by the acquisition of additional data dedicated to fill-in the gaps between national data sets and at the interface of the traditional disciplinary border between geology and geophysics. These three natural laboratories permitted to develop a

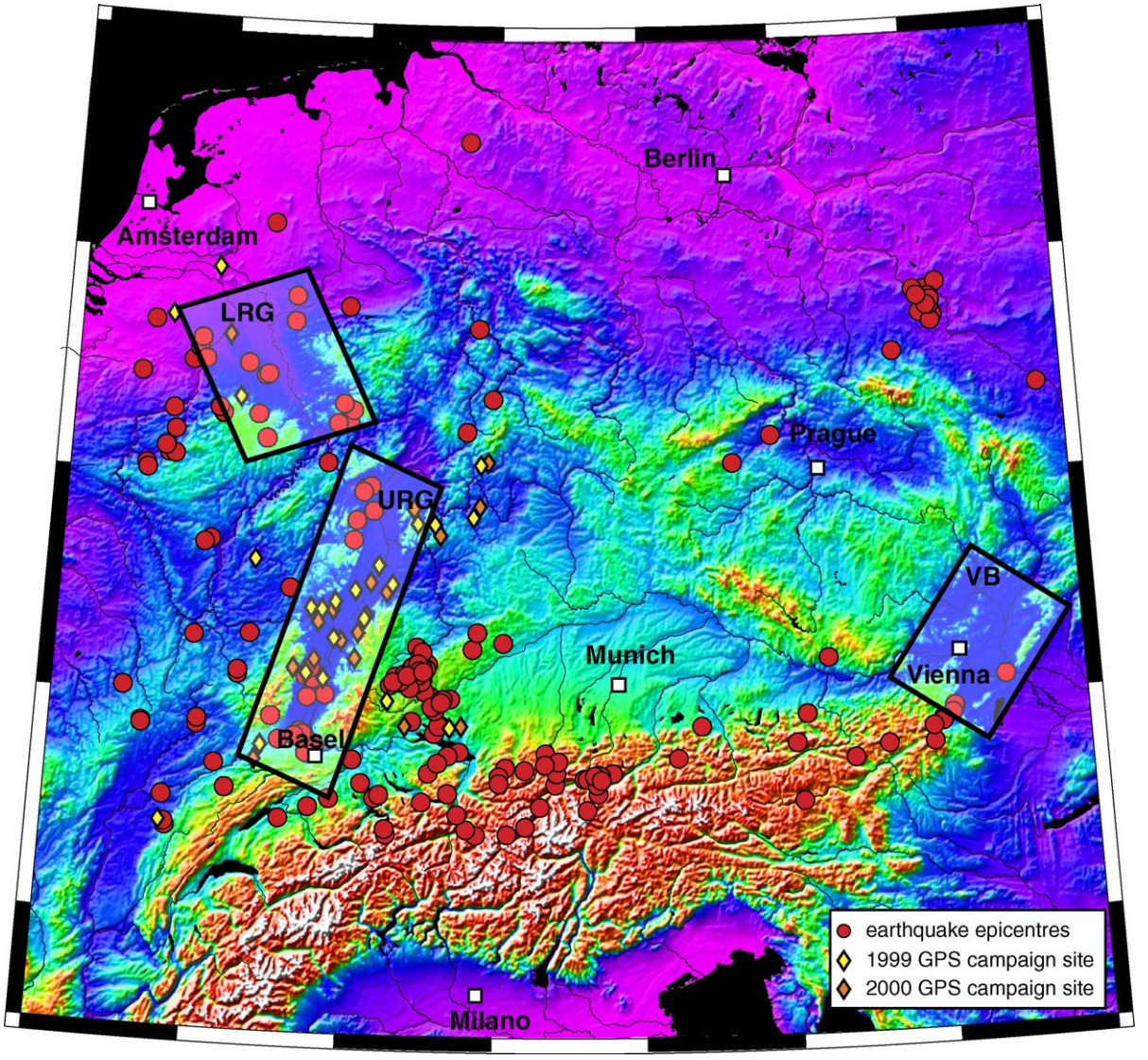

Fig. 1. Topography of the Alpine Mountain chain and its foreland, showing distribution of earthquake activity and location of GPS campaign sites. The seismicity was extracted from online databases (NEIC, 2004; ORFEUS, 2004). Only epicentres of events with a magnitude larger than 3 occurring between 1965 and 1987 are shown. Boxes outline areas selected as ENTEC natural laboratories in the Lower Rhine Graben (LRG), the Upper Rhine Graben (URG) and the Vienna Basin (VB).

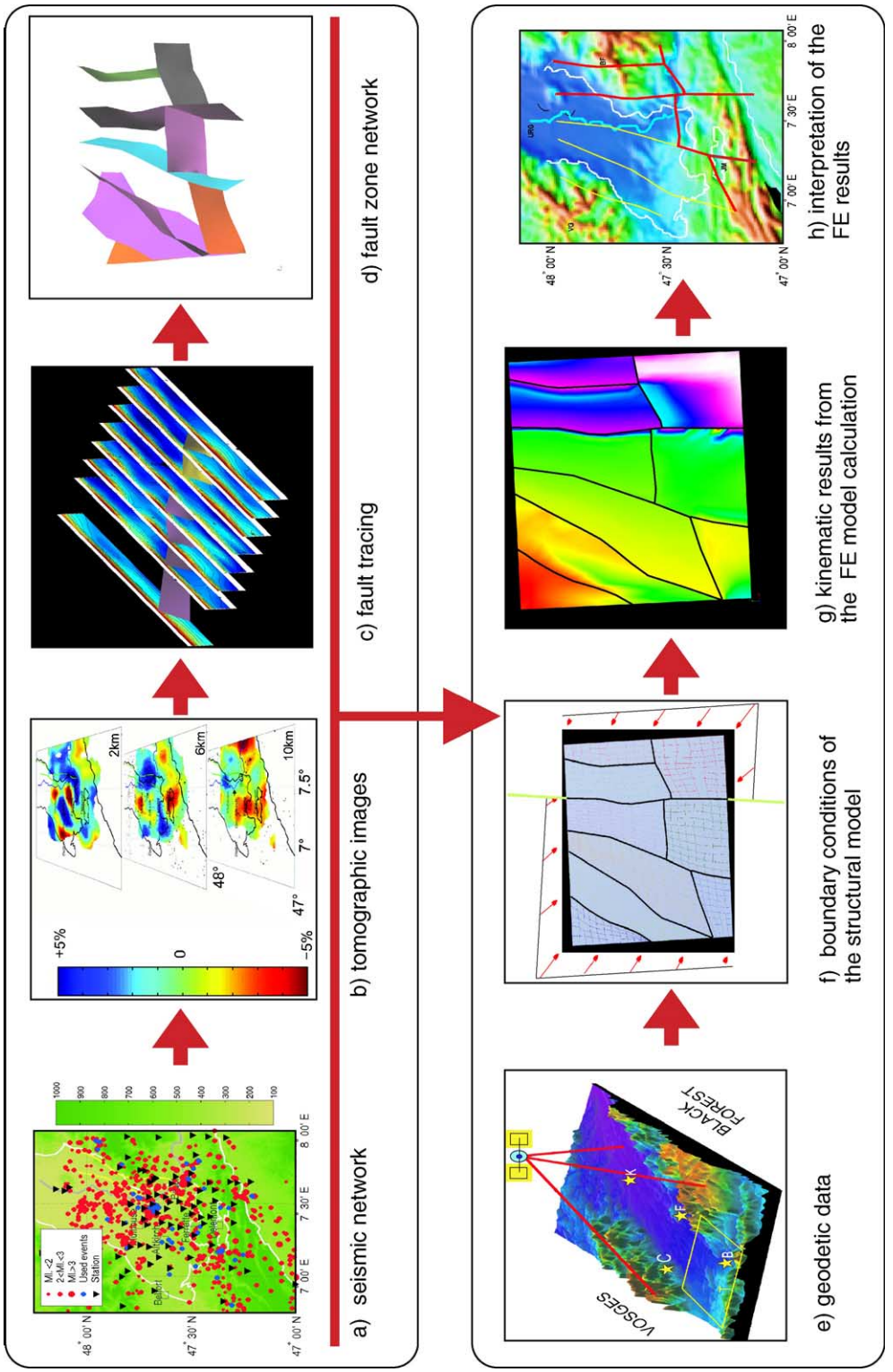

Fig. 2. Steps of the methodology used. Upper panel: synthesis of local earthquake tomography data to construct the structural domain (a) seismic network for tomographic data acquisition, (b) tomographic database, (c) tracing of fault zones through tomographic profiles, (d) final fault zone network. Lower panel: synthesis of regional boundary conditions based on geodetic constraints to be integrated with structural data in a finite element model, and its geological interpretation (e) geodetic data, (f) building of the structural domain and finite element mesh, (g) results from finite element calculation of northward displacement, (h) interpretation of results (active faults in red).

platform for studies addressing deformation of the frontal parts of a still active orogen as well as its immediate and distal forelands. The VB was regarded as a "within-orogen" natural laboratory that focused on the link between the disruption of the frontal parts of the Alpine Orogen and lithospheric dynamics. The URG, located in the immediate Alpine foreland, was regarded as a "near-field" natural laboratory which permits to address the relationship between neotectonics and surface processes and the response of the thermally weakened Northwest European lithosphere to collision-related foreland stresses controlling its deformation, including lithospheric folding. The LRG, located in the distal Alpine foreland, was considered as a "far-field" natural laboratory that addresses the interaction between neotectonics, morphologic evolution, the timing and quantification of processes controlling uplift and denudation that are governed by the response of the lithosphere to intraplate stresses and deep mantle processes.

A fundamental aspect of the ENTEC Project was the integration of geological, geophysical, geomorphologic, geodetic, seismological data, and the development of dynamic models (Fig. 2) in an effort to quantify the societal impact of environmental tectonics in areas hosting major urban and industrial activity concentrations (Fig. 3). The ENTEC Project was centred on multiscale modelling of the past and present evolution of the VB, URG and LRG. In this respect, it specifically addressed the neotectonic deformation and related seismic hazard of these basins, the configuration and evo-

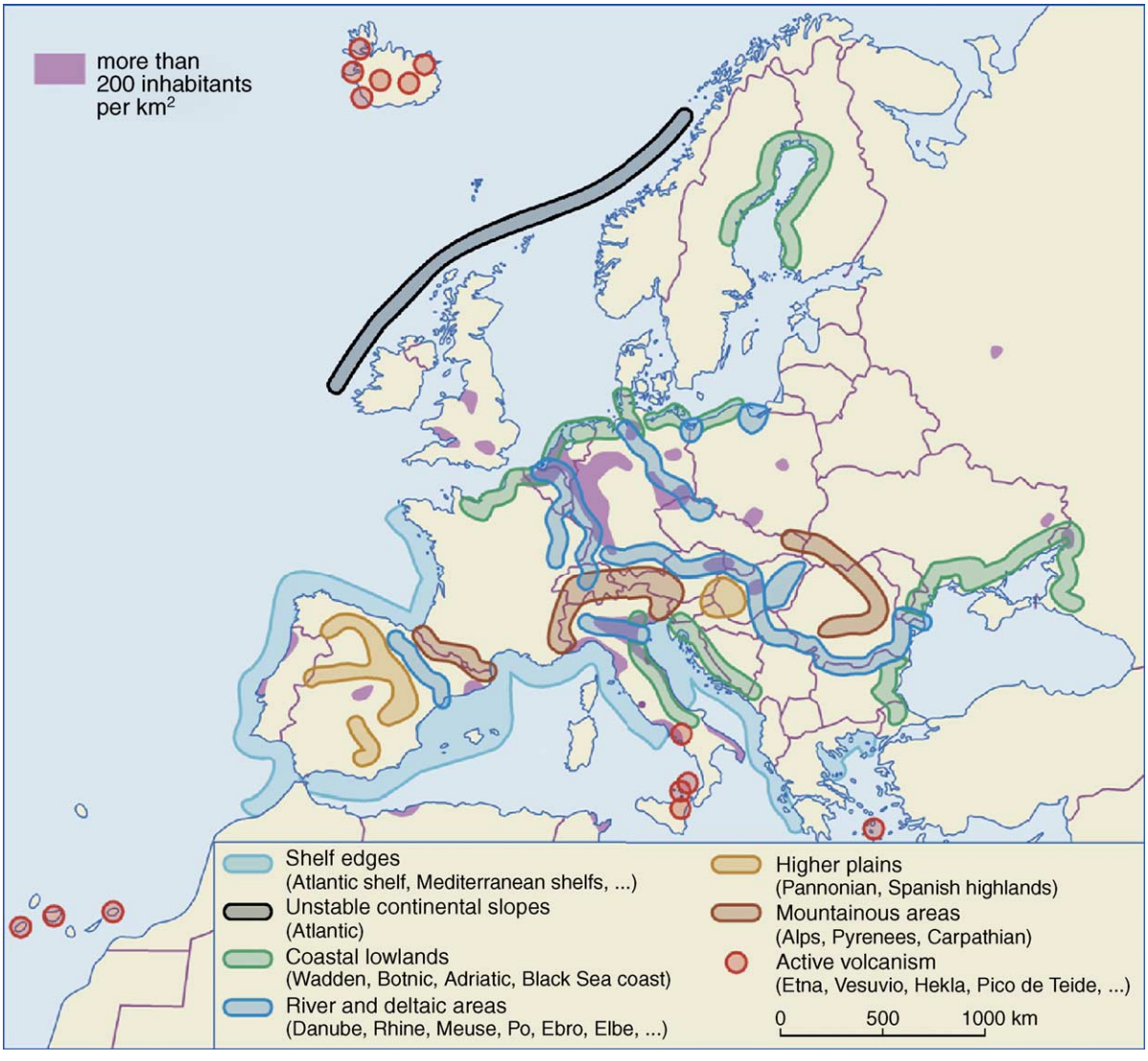

Fig. 3. Link between demography and environmental tectonics in Western and Central Europe.

lution of their sedimentary fill, and their crustal and lithospheric structure. Monitoring, reconstruction and dynamic modelling of the past and present evolution of these basins are strongly connected and leads to better geopredictions. Significant added value was realized by integrated interpretation of multidisciplinary data sets.

2. Rationale for integrated research on dynamic topography

During the last decade, Earth Science research has rapidly evolved, partly owing to the collection of large new 3-D data sets and the intense use of computing technologies in their processing and interpretation. At the same time, modelling of geological processes proved to be a successful vehicle for the integration of different disciplines of the Solid Earth Sciences. There is now a growing demand for integrated Earth Sciences in such strategic domains as the management of energy and water resources and natural environment. Environmental tectonics links neotectonics and continental intraplate topography, focusing on tectonic processes that operate at lithospheric and crustal scales and surface processes and their expression in the record of sedimentary basins and (paleo)seismicity.

2.1. Geoprediction in space and time

Research in the field of neotectonics and continental topography has proven to be an effective mechanism for closing the traditional communication gaps between sedimentary geology, endogene tectonics, geophysics and geotechnology. Results of this type of research, in which tectonic modelling plays a very important role, find widespread application in the exploration for natural resources. The ENTEC Project focused on quantitative methods of geoprediction in space and time. This includes prediction in the sense of forecasting the future behaviour of entire geological systems, as well as of specific subsurface geological features. Such predictions are highly relevant to the current and future needs of humanity, particularly in areas of active tectonics in terms of assessment of natural hazards, water supply damage, environmental degradation potential and disaster mitigation.

2.2. Research objective

The main objective is to gain an understanding of the role played by tectonic activity in the degradation of the environment, taking the North Alpine foreland as a natural laboratory. The research strategy is based on the integration of geological, geomorphologic, geodetic, seismological, geophysical and geotectonic approaches to the assessment of the type, magnitude and rate of tectonic deformation. This permits to look not only at time windows of tens to hundreds of years (geodesy, seismology), which in terms of Earth system dynamics are insignificant, but also at windows of thousands to millions of years (geomorphology, geology, geophysics) which are relevant in terms of analysing on-going dynamic processes. Particularly geomorphologic analyses of the landscape evolution under exogenic (climate, erosion) and endogenic (tectonic) forcing provides data for characterizing on-going deformation patterns, and to back-trace them over a time span of up to a few million years, in terms of (i) localization of active geological structures, (ii) deformation kinematics, segmentation and rates along such structures, and (iii) assessment of endogenic forcing mechanisms.

2.3. Socio-economic objectives

Human use of the outermost solid Earth intensifies at a rapid pace. Increasing utilization of the human habitat carries largely unknown risks. Therefore, there is an urgent need for scientifically advanced geoprediction systems, which can accurately locate subsurface resources and forecast the recurrence time and magnitude of destructive earthquakes, volcanic eruptions, landslides and longer term land subsidence or uplift. This relates particularly to the URG, LRG and VB, each of which hosts major industrial and population centres (Fig. 3). The European Cenozoic rift system, of which the Rhine Graben forms part, corresponds to a zone of elevated seismic activity (Ahorner, 1975; Mueller, 1968; Prodehl et al., 1995; Dèzes et al., 2004), as evidenced by such historical earthquakes as the ones of 1201 and 1356 that destroyed the city of Basel, or the 1992 Roermond earthquake in the LRG. Latent volcanic activity presents an additional hazard, particularly on the Rhenish Massif.

In the URG and LRG, all major cities and industrial centres are located on the flood plain or on terraces of these tectonically active rift valleys. Therefore, they have to contend with elevated seismic hazards (Fig. 1). Moreover, the Quaternary sediments of the URG constitute a major aquifer that plays a very important role in the water supply of population centres, and as such requires management and quality control. Similarly, the densely urbanized and industrialized VB hosts two European capitals (Vienna, Bratislava), about 3 million people and numerous vulnerable facilities (chemical plants, refineries, dams, nuclear power plants).

3. Lithosphere-scale intraplate deformation of Europe

At a larger scale, and as a result of a number of International Lithosphere Program Projects, such as the World Stress Map (Fig. 4; Müller et al., 1992; Zoback and Burke, 1993) and the Task Force Origin of Sedimentary Basins (Cloetingh et al., 1996, 1998), new data sets, such as the Moho map (Fig. 5) (Dèzes and Ziegler, 2004), were generated which document the stress field and recent crustal-scale vertical movements in NW Europe. These studies revealed strong coupling between the stress field and intraplate deformation in NW Europe that is related to mechanical coupling of the European foreland lithosphere with the Alpine Orogen and the North Atlantic sea-floor spreading axes (Ziegler et al., 1995, 1998, 2001). It is now becoming increasingly evident that in intraplate domains (Figs. 4–6) the European lithosphere responds to compression, apart from reactivation of pre-existing crustal discontinuities (basin inversion, upthrusting of basement blocks), primarily by large-scale lithospheric folding

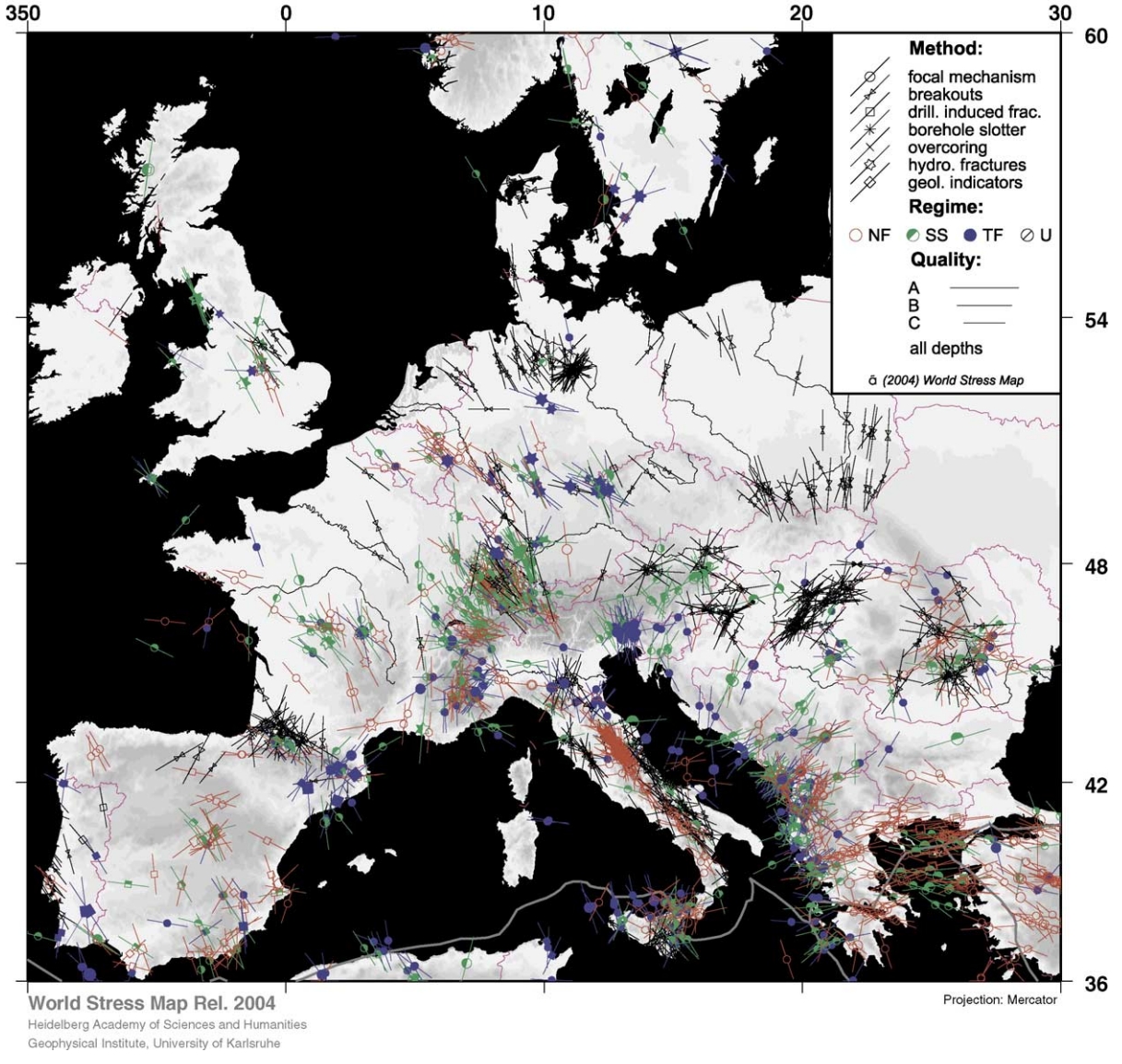

Fig. 4. Stress map for Europe, displaying present-day orientation of the maximum horizontal stress (S_{Hmax}). Different symbols stand for different stress indicators. The length of symbols represents the data quality, 'A' being of highest quality. Background shading indicates topographic elevation (darker is higher). This map was extracted from the World Stress Map database (World Stress Map, 2004).

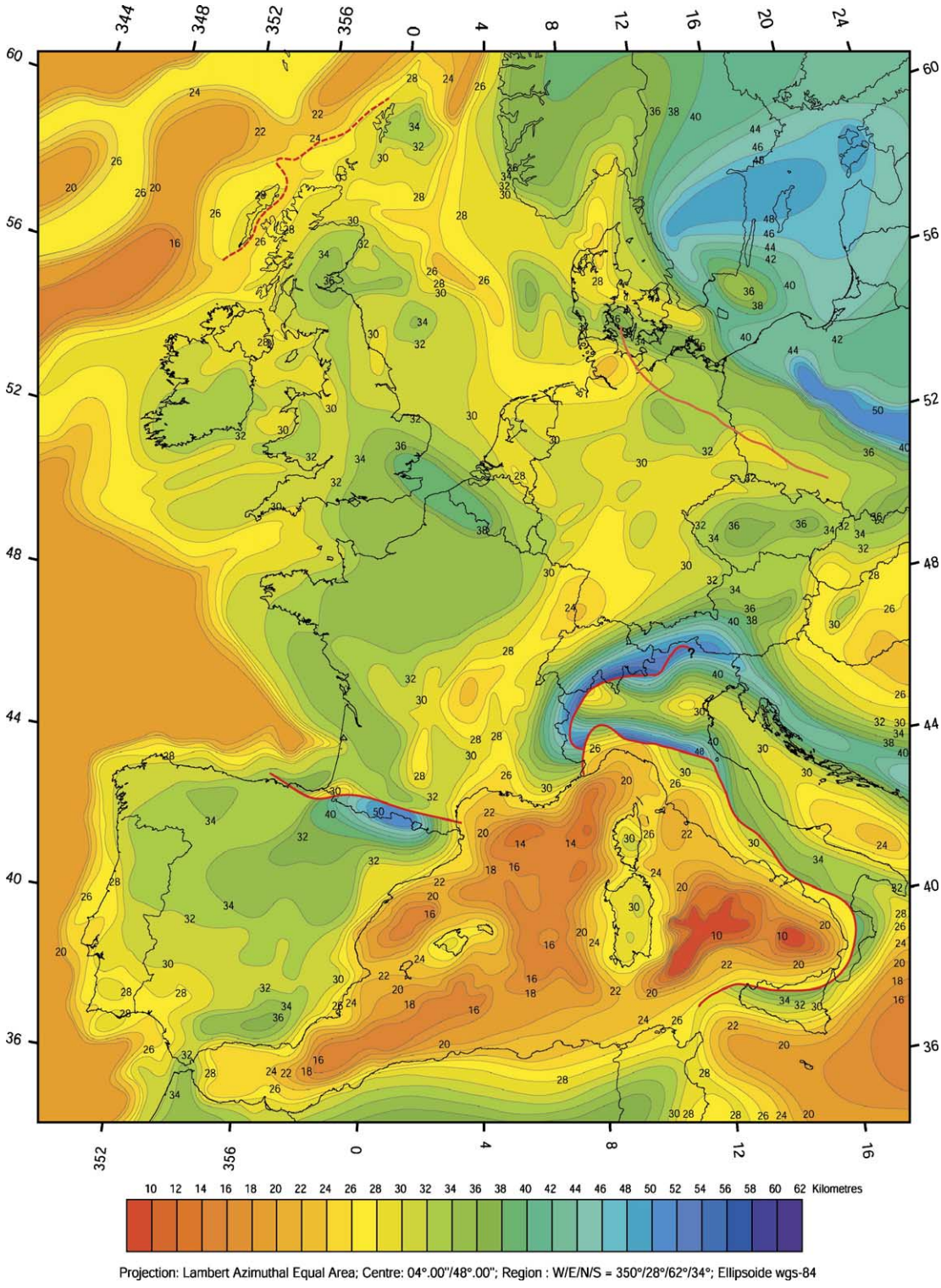

Fig. 5. Depth map of Moho discontinuity (2 km contour interval), constructed by integration of published regional maps (after Dèzes and Ziegler, 2004). For data sources see http://comp1.geol.unibas.ch/. Red lines (solid and stippled) show offsets of the Moho discontinuities.

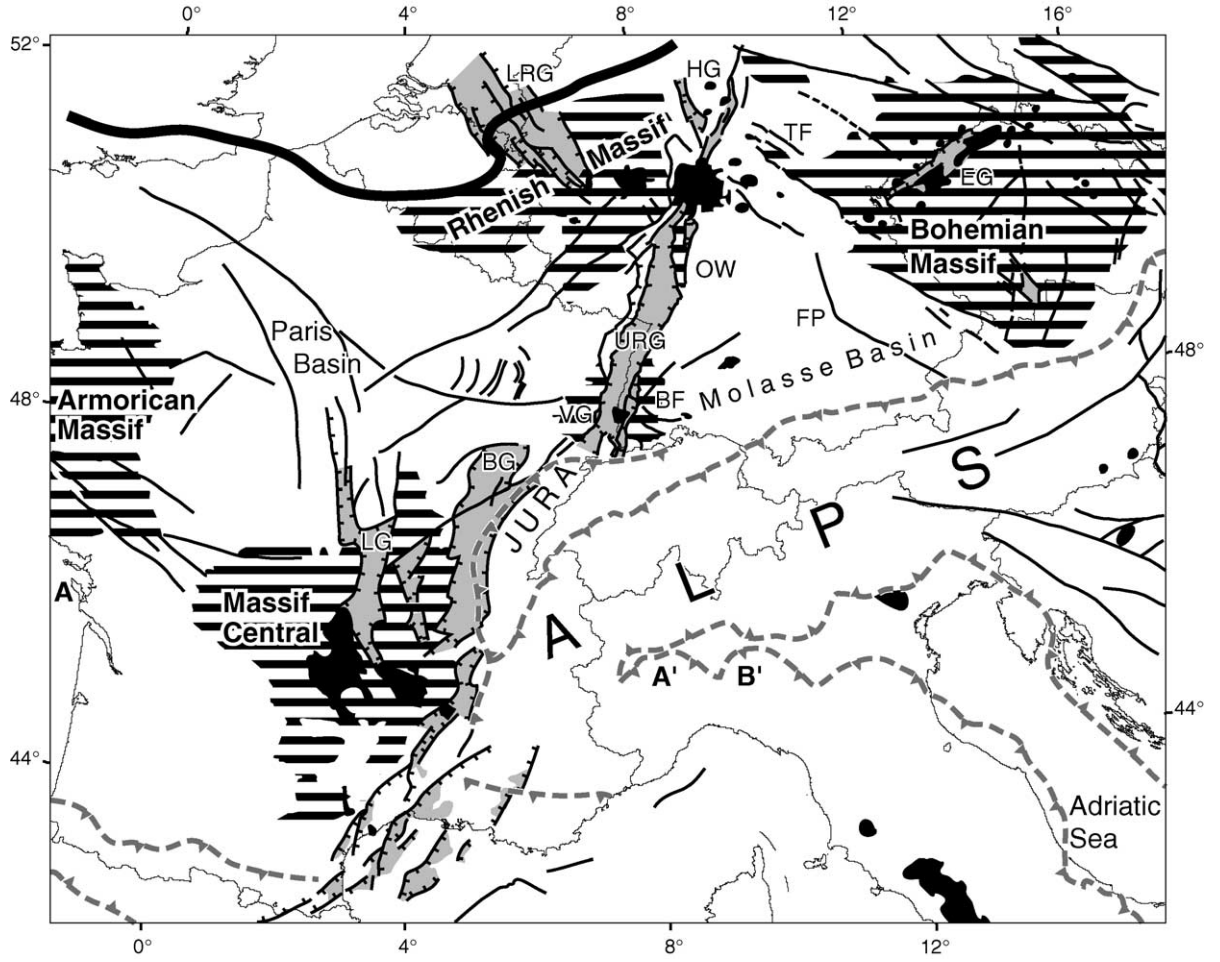

Fig. 6. Location map of ECRIS in the Alpine and Pyrenean foreland, showing Cenozoic fault systems (black lines), rift-related sedimentary basins (light grey), Variscan massifs (line pattern) and volcanic fields (black). Fat solid line: Variscan deformation front. Stippled barbed line: Alpine deformation front. BF, Black Forest; BG, Bresse Graben; EG, Eger (Ohre) Graben; FP, Franconian Platform; HG, Hessian grabens; LG, Limagne Graben; LRG, Lower Rhine (Roer Valley) Graben; URG, Upper Rhine Graben; OW, Odenwald; TF, Thuringian Forest; VG, Vosges (after Dèzes et al., 2004).

(Cloetingh et al., 1999; Ziegler et al., 2002; Dèzes et al., 2004).

3.1. Strength of Europe's intraplate lithosphere

In this context it is interesting to note, that studies on the mechanical properties of the European lithosphere revealed a direct link between its thermo-tectonic age and bulk strength (Cloetingh and Burov, 1996). On the other hand, inferences from P and S wave tomography (Goes et al., 2000a,b; Ritter et al., 2000, 2001) and thermo-mechanical modelling (Garcia-Castellanos et al., 2000) point to a pronounced weakening of the lithosphere in the Lower Rhine area owing to high upper mantle temperatures. However, the late Neogene and Quaternary tectonics of the Ardennes–Lower Rhine area may form part of a much wider deformation system that overprints the Late Palaeozoic and Mesozoic basins of NW Europe. This is supported by geomorphologic evidence and the results of seismicity studies in Brittany (Bonnet et al., 1998, 2000) and Normandy (Lagarde et al., 2000; Van Vliet-Lanoë et al., 2000), partly carried out in the framework of the GeoFrance 3-D project, by data from the Ardennes–Eifel region (Demoulin et al., 1995; Demoulin, 1998; Meyer and Stets, 1998; Sintubin et al., 1999; Van Balen et al., 2000), the southern parts of the URG (Nivière and Winter, 2000) and the North German Basin (Kraus and Möbus, 1981; Ludwig, 1995; Bayer et al., 1999).

Lithosphere-scale folding and buckling, in response to the build up of compressional intraplate stresses, can cause uplift or subsidence of relatively

large areas at time scales of a few My and thus can be an important driving mechanism of neotectonic processes. For instance, the Plio–Pleistocene accelerated subsidence of the North Sea Basin is attributed to its down-buckling in response to the build-up of the present day stress field (Van Wees and Cloetingh, 1996). Similarly, uplift of the Vosges–Black Forest Arch, which at the level of the crust–mantle boundary extends from the Massif Central into the Bohemian Massif (Fig. 6), commenced during the Burdigalian (±18 Ma) and persisted until at least early Pliocene times. Uplift of this arch is attributed to lithospheric folding controlled by compressional stresses originating in the Alpine collision zone (Ziegler et al., 2002; Dèzes et al., 2004). An understanding of the temporal and spatial strength distribution in the NW European lithosphere may offer quantitative insights into the patterns of its intraplate deformation (basin inversion, upthrusting of basement blocks), and particularly into the pattern of lithosphere-scale folding and buckling.

Owing to the large amount of high quality geophysical data acquired during the last 20 years in Europe, its lithospheric configuration is rather well known though significant uncertainties remain in many areas about the seismic and thermal thickness of the lithosphere (Babuska and Plomerova, 1992; Artemieva and Mooney, 2001). Nevertheless, the available data permit to constrain the rheology of the European lithosphere, thus enhancing our understanding of its strength.

So far, strength envelopes and the effective elastic thickness of the lithosphere have been calculated for a number of locations in Europe (e.g. Cloetingh and Burov, 1996). However, as such calculations were made for individual scattered points only, or along transects, they provide limited information on lateral strength variations of the lithosphere. Although lithospheric thickness and strength maps have already been constructed for the Pannonian Basin (Lankreijer et al., 1999) and the Baltic Shield (Kaikkonen et al., 2000), such maps are not yet available for all of Europe.

As evaluation and modelling of the response of the lithosphere to vertical and horizontal loads requires an understanding of its strength distribution, efforts were dedicated to map the strength of the European foreland lithosphere, using the GRASS-GIS system (http://grass.itc.it) for organizing data sets and to serve as development platform for integrated 3D strength calculations based on newly developed routines.

Strength calculations of the lithosphere depend primarily on its thermal and compositional structure and are particularly sensitive to thermal uncertainties (Ranalli and Murphy, 1987; Ranalli, 1995; Burov and Diament, 1995). For this reason, the workflow aimed at the development of a 3D strength model for Europe was two-fold: (1) construction of a 3D compositional model and (2) calculating a 3D thermal cube. The final 3D strength cube was obtained by calculating 1D strength envelopes for each lattice point (x, y) of a regularized raster covering NW-Europe (Fig. 7). For each lattice-point the appropriate input values were obtained from a 3D compositional and thermal cube. A geological and geophysical geographic database was used as reference for the construction of the input models.

For continental realms, a 3D multi-layer compositional model was constructed, consisting of one mantle layer, 2–3 crustal layers and an overlying sedimentary cover layer, whereas for oceanic areas a one-layer model was adopted. For the depth to the different interfaces several regional or European-scale compilations were available, which are based on deep seismic reflection and refraction or surface wave dispersion studies (e.g. Panza, 1983; Calcagnile and Panza, 1987; Suhadolc and Panza, 1989; Blundell et al., 1992; Du et al., 1998; Artemieva et al., in press). For the base of the lower crust, we strongly relied on the European Moho map of Dèzes and Ziegler (2004) (Fig. 5). Regional compilation maps of the seismogenic lithosphere thickness were used as reference to the base of the thermal lithosphere in subsequent thermal modelling (Babuska and Plomerova, 1993, 2001; Plomerova et al., 2002).

Fig. 8a shows the integrated strength under compression of the entire lithosphere of Western and Central Europe, whereas Fig. 8b displays the integrated strength of the crustal part of the lithosphere. As evident from Fig. 8, Europe's lithosphere is characterized by major spatial mechanical strength variations, with a pronounced contrast between the strong Proterozoic lithosphere of the East-European Platform to the east of the Teisseyre–Tornquist line and the relatively weak Phanerozoic lithosphere of Western Europe.

A similar strength contrast occurs at the transition from strong Atlantic oceanic lithosphere to the relatively weak continental lithosphere of Western Europe. Within the Alpine foreland, pronounced northwest–southeast trending weak zones are recognized that coincide with such major geologic structures as the Rhine Graben System and the North Danish–Polish Trough, that are separated by the high-strength North German Basin and the Bohemian Massif. Moreover, a broad zone of weak lithosphere characterizes the Massif Central and surrounding areas.

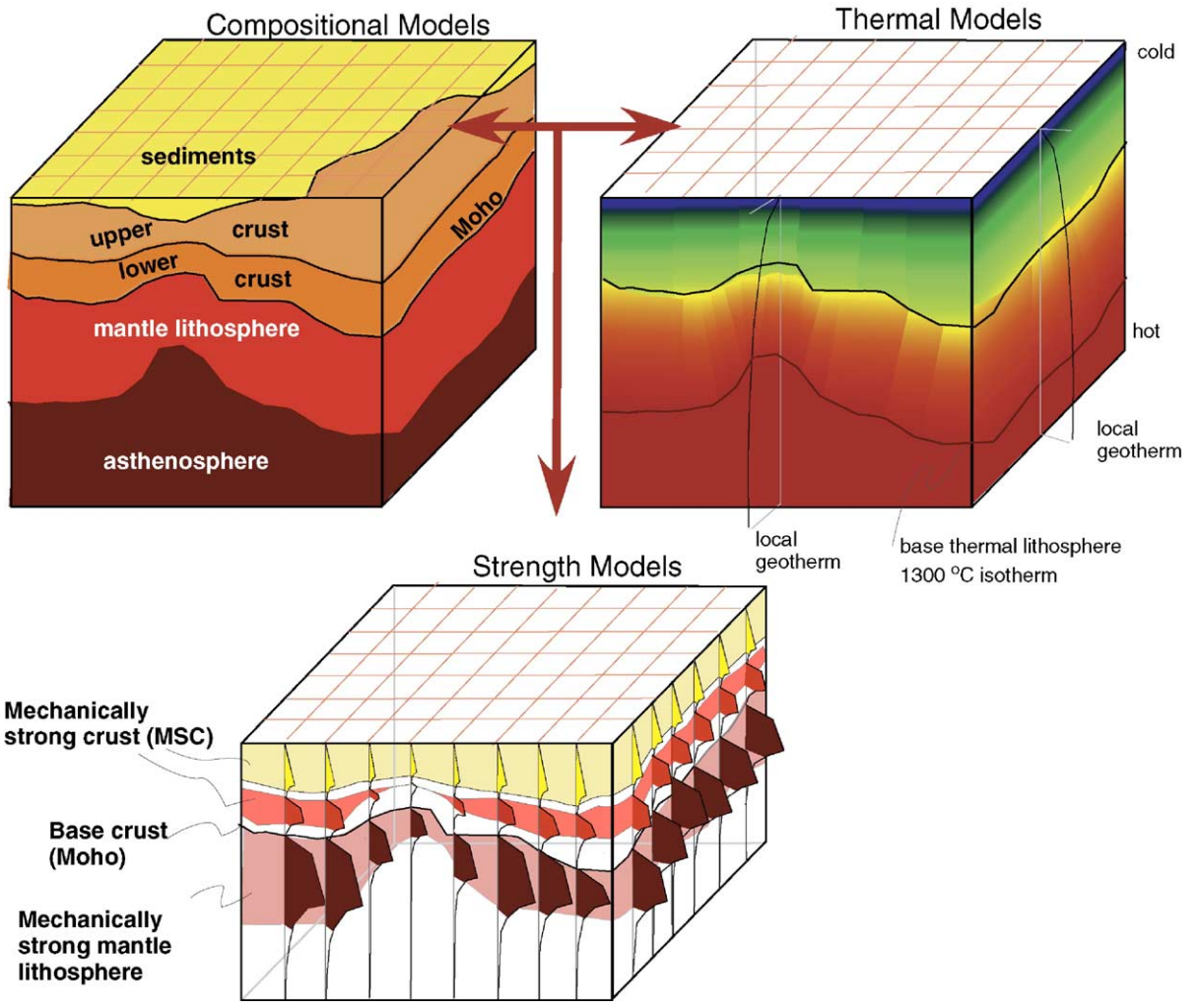

Fig. 7. From crustal thickness (top left) and thermal structure (top right) to lithospheric strength (bottom): conceptual configuration of the thermal structure and composition of the lithosphere, adopted for the calculation of 3D strength models.

The presence of thickened crust in the area of the Teisseyre–Tornquist suture zone (Fig. 5) gives rise to a pronounced mechanical weakening of the lithosphere, particularly of its mantle part.

Whereas the lithosphere of Fennoscandia is characterized by a relatively high strength, the North Sea rift system corresponds to a zone of weakened lithosphere. Other areas of high lithospheric strength are the Bohemian Massif and the London–Brabant Massif which both exhibit low seismicity (Fig. 9).

A pronounced contrast in strength can also be noticed between the strong Adriatic indenter and the weak Pannonian Basin area (see also Fig. 8).

Comparing Fig. 8a and b reveals that the lateral strength variations of Europe's intraplate lithosphere are primarily caused by variations in the mechanical strength of the mantle-lithosphere, whereas variations in crustal strength appear to be more modest. The variations in mantle-lithospheric strength are primarily related to variations in the thermal structure of the lithosphere, that can be related to thermal perturbations of the sub-lithospheric upper mantle imaged by seismic tomography (Goes et al., 2000a), with lateral variations in crustal thickness playing a secondary role, apart from Alpine domains which are characterized by deep crustal roots. High strength in the East-European Platform, the Bohemian Massif, the London–Brabant Massif and the Fenno-Scandian Shield reflects the presence of old, cold and thick lithosphere, whereas the European Cenozoic Rift System coincides with a major axis of thermally weakened lithosphere within the Northwest European Platform. Similarly, weakening of the lithosphere of southern France can be attributed to the presence of tomographically imaged plumes rising up

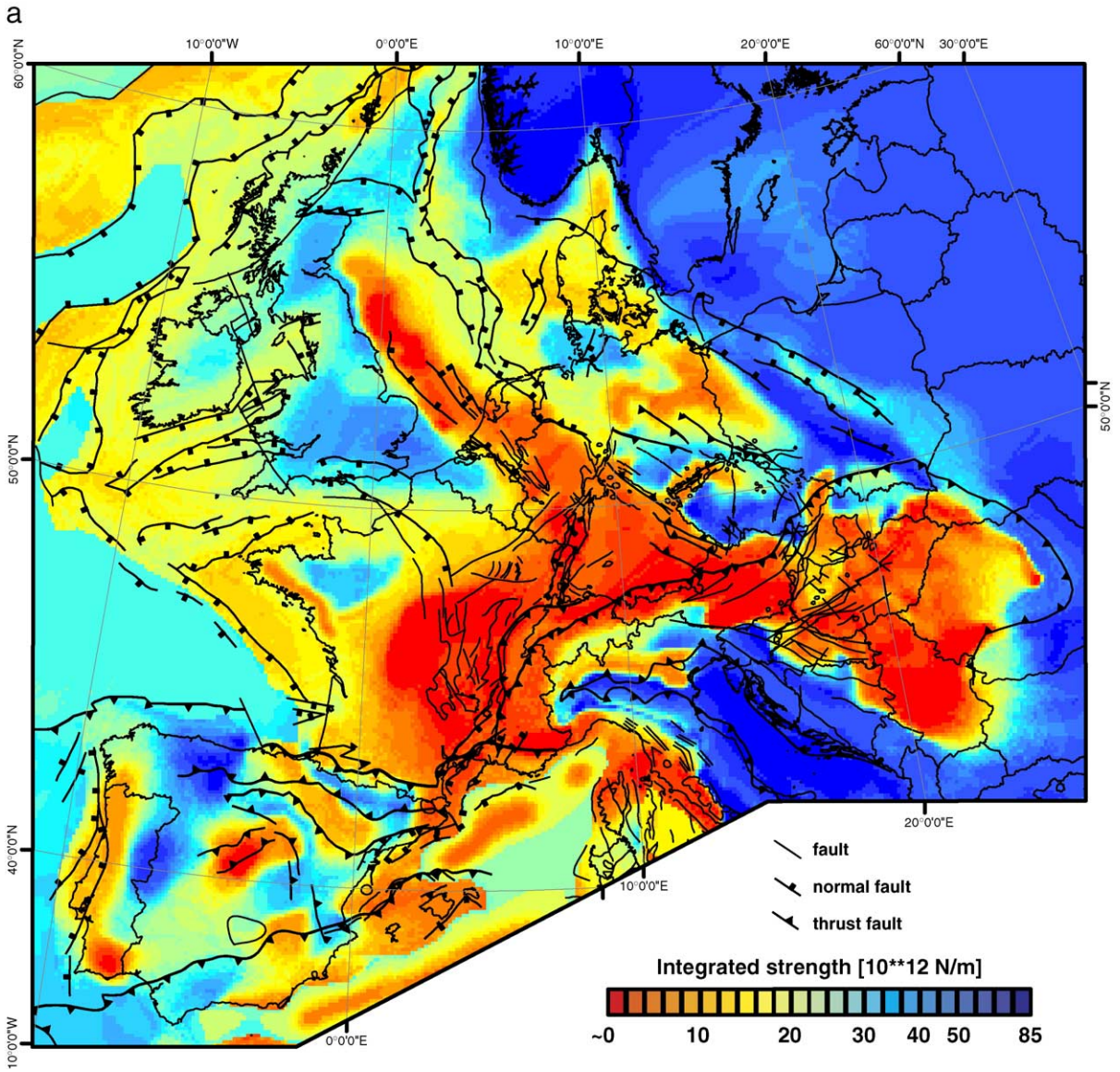

Fig. 8. Integrated strength maps for intraplate Europe. Adopted composition for upper crust, lower crust and mantle is based on a wet quartzite, diorite and dry olivine composition, respectively. Rheological rock parameters are based on Carter and Tsenn (1987). The adopted bulk strain-rate is 10^{-16} s^{-1}, compatible with constraints from GPS measurements (see text). Contours represent integrated strength in compression for (a) total lithosphere, and (b) crust. The main structural features of Europe are superimposed on the strength maps (after Ziegler, 1988; Dèzes et al., 2004).

under the Massif Central (Granet et al., 1995; Wilson and Patterson, 2001).

The major lateral strength variations that characterize the lithosphere of extra-Alpine Phanerozoic Europe are largely related to its Late Cenozoic thermal perturbation as well as to Mesozoic and Cenozoic rift systems and intervening stable blocks, and not so much to the Caledonian and Variscan orogens and their accreted terranes (Dèzes et al., 2004). These lithospheric strength variations (Fig. 8a) are primarily related to variations in the thermal structure of the lithosphere, and therefore, are compatible with inferred variations in the Effective Elastic Thickness (EET) of the lithosphere (see Cloetingh and Burov, 1996).

The most important strong inliers in the lithosphere of the Alpine foreland lithosphere correspond to the Early Palaeozoic London–Brabant Massif and the Variscan Armorican, Bohemian and West-Iberian Massifs. The strong Proterozoic Fennoscandian–East-European

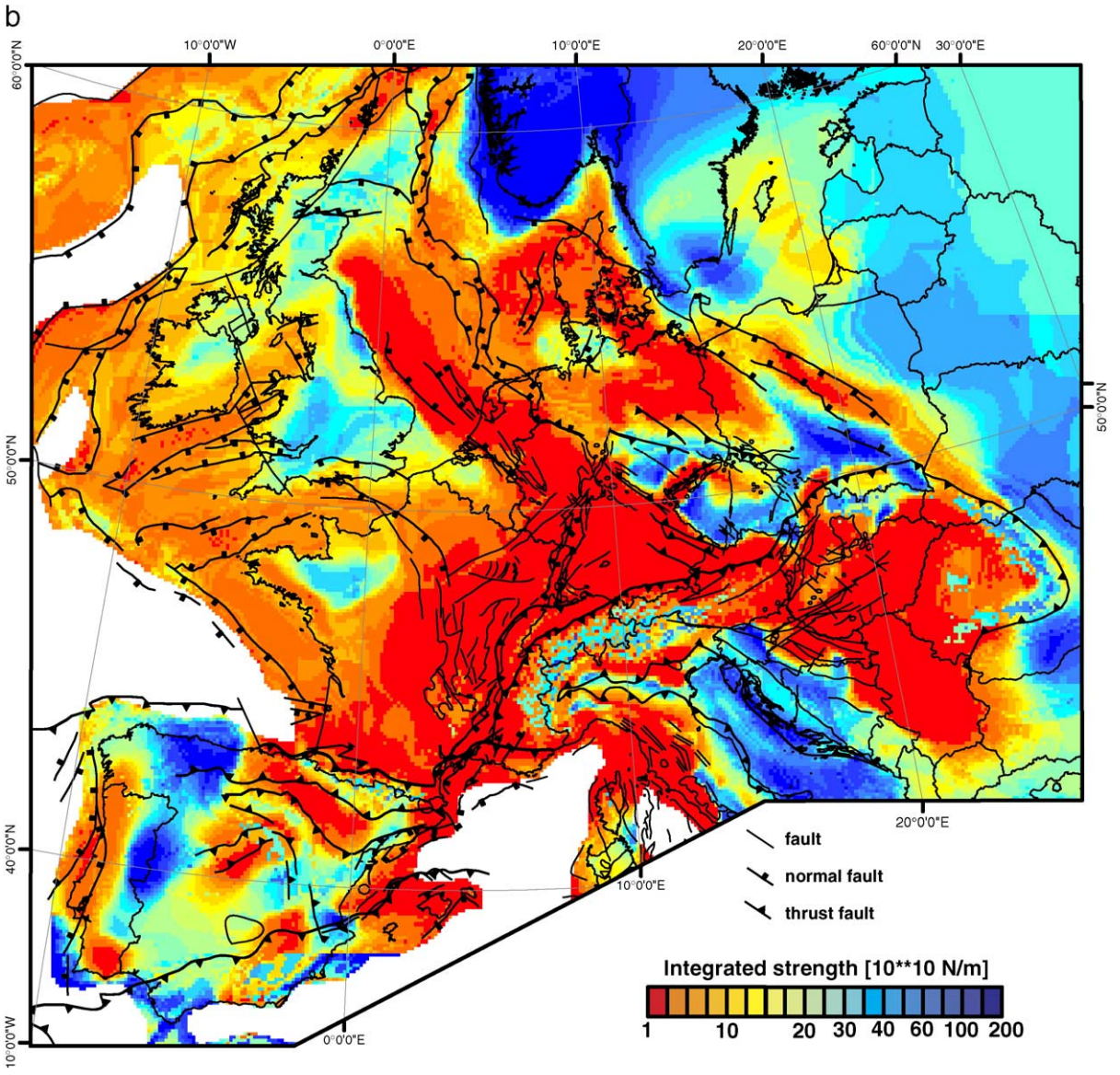

Fig. 8 (*continued*).

Craton flanks the weak Phanerozoic European lithosphere to the northeast whereas the strong Adriatic indenter contrasts with the weak lithosphere of the Mediterranean collision zone.

Fig. 9 displays on the background of the crustal strength map the distribution of seismic activity, derived from the NEIC global earthquake catalogue (USGS). As obvious from Fig. 9, crustal seismicity is largely concentrated on the presently still active Alpine plate boundaries, and particularly on the margins of the Adriatic indenter. In the Alpine foreland, seismicity is largely concentrated on zones of low lithospheric strength, such as the European Cenozoic rift system, and areas where pre-existing crustal discontinuities can be reactivated under the presently prevailing NW-directed stress field, such as the South Armorican shear zone (Dèzes et al., 2004) and the rifted margin of Norway (Mosar, 2003).

It should be noted that the strength maps presented in Fig. 8 do not incorporate the effects of spatial variations in composition in crustal and mantle layers. In future work we will address the effects of such second order strength perturbations, adopting constraints on the composition of several crustal and mantle layers provided by

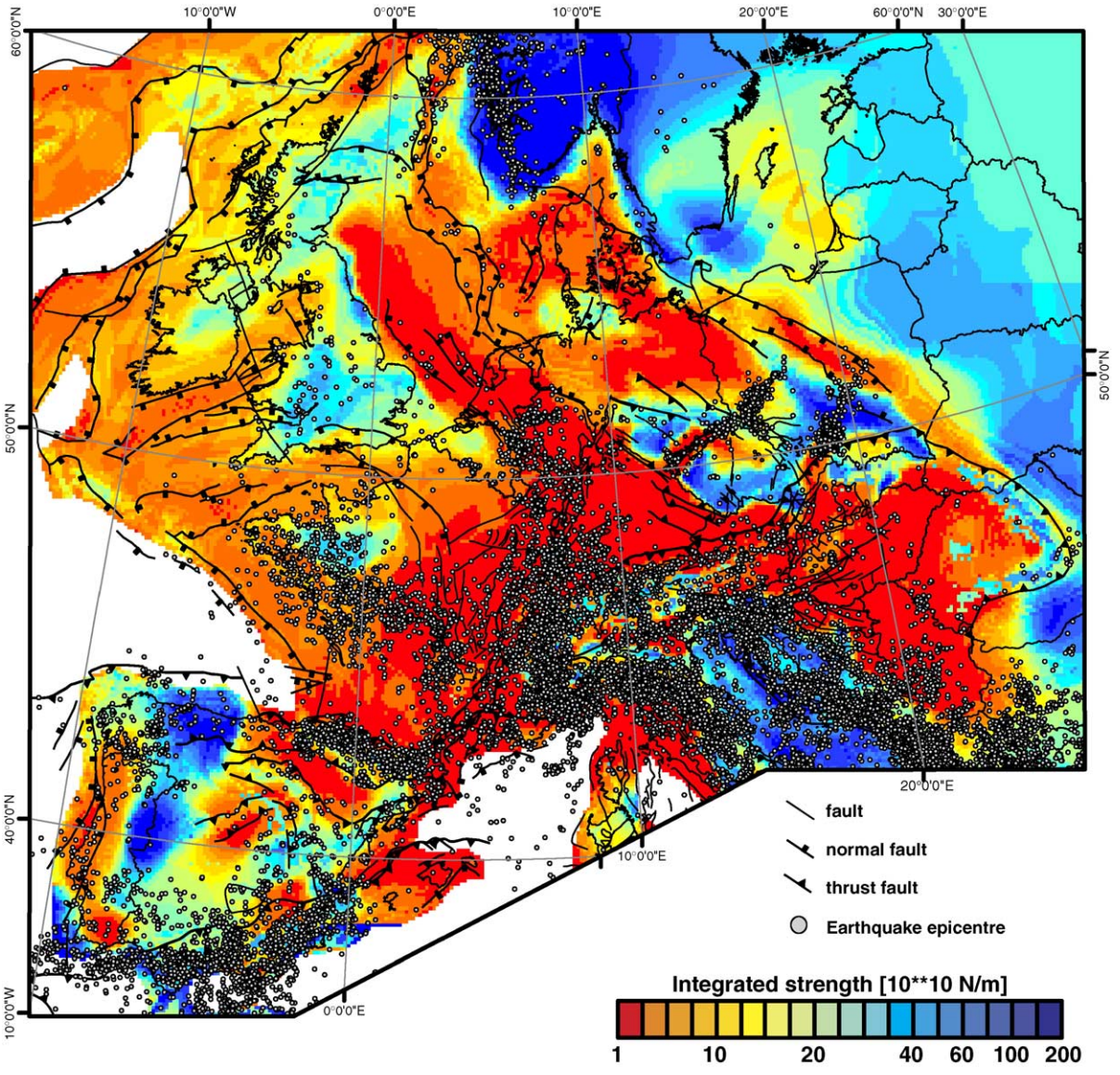

Fig. 9. Spatial comparison of crustal seismicity and integrated crustal strength (see Fig. 8b). Earthquake epicentres from the NEIC data center (NEIC, 2004), queried for magnitude >2 and focal depths <35 km.

seismic velocities (Guggisberg et al., 1991; Aichroth et al., 1992) and crustal and upper mantle xenolith studies (Mengel et al., 1991; Wittenberg et al., 2000).

3.2. Geodetic constraints on broad-scale deformation across the Rhine Graben and Alps

Based on the investigation of the velocity and strain distribution derived from GPS data, the present day kinematical field of western Europe was analyzed, with special emphasis on the URG area. In order to display the intraplate velocities in central Western Europe, we used the velocity datasets of permanent GPS stations in the ITRF2000 reference frame that were processed by Swisstopo[2] (in the following called "Swisstopo dataset"). Displacement rates were determined for 53 GPS sites located in 7 countries (Italy, Switzerland, Austria, Germany, France, Belgium and The Netherlands), covering the major structural units of western Europe, and belonging to different networks (EUREF, AGNES, REGAL and RGP).[3] These values were obtained on

[2] *Swiss Federal Office of Topography.*

[3] *European Reference Frame* (EUREF); *Automated GPS Network for Switzerland* (AGNES); *Réseau GPS permanent dans les Alpes* (REGAL); *Réseau GPS Permanent* (RGP).

the basis of weekly solutions, calculated by processing the raw data with the Bernese software (Beutler et al., 2001; Brockmann et al., 2001, 2002a,b). A limited number of stations with unstable and/or short time series were excluded from the Swisstopo dataset. At the same time, some ITRF2000 velocity values of EUREF stations (in the following called "EUREF dataset") with a long and stable time series were included in order to obtain a more homogeneous distribution of the GPS sites. Data from these stations (BRUS, GOPE, KOSG, POTS and WSRT) were integrated with the Swisstopo data set applying a Helmert transformation (Tesauro et al., 2005). To calculate the motion of the European plate, we used the pole of its rotation as defined by Altamimi et al. (2002). Subsequently we subtracted these velocity values from the ITRF2000 velocities to obtain the residuals (=intraplate relative velocities) with respect to the rotation of the Eurasian plate (Table 1 and Fig. 10). The length of the time series is not the same for all the stations, as EUREF stations recorded since 1996, whilst the Swisstopo stations started to record in 1998. For most of the stations, the analysed time series cover the period from 1998 up to mid 2003 (see Table 1 for details).

Owing to the poor reliability of the vertical component of GPS velocities, we considered only their horizontal components, V_{north} and V_{east}, respectively. The standard deviations, assumed equal for the both components, were calculated for each GPS permanent station on the basis of the length of the time span ($\sigma = 1$ mm/$\sqrt{\text{yr}}$) (Table 1). In this way, we applied the same unique criterion in the evaluation of this parameter to all stations.

GPS stations located between longitude 4°E and 16°E generally move in NW direction at rates between 0.1 and 2.9 mm/yr. Some stations located in Switzerland, differ from this general trend, possibly owing to local effects (Fig. 10). The only two stations located in the URG area, Karlsruhe (KARL) and Strasbourg (STRA), apparently move slowly to the N and NW at relative velocities of $V = 0.81$ and 0.34 mm/yr, respectively (see Table 1). Stations located between longitudes 4°E and 5°W apparently move to the SW to S at relative velocities between 0.5 and 1.5 mm/yr.

On the basis of these velocity solutions, the strain rate field was calculated using the least-squares collocation method (Straub, 1996; Kahle et al., 2000). This method requires the specification of a covariance distance, which is equivalent to the correlation length, which is usually chosen equal to the distance average of the GPS stations. The standard deviation sigma represents the strength of the signal. The strain rate field is displayed as principal axis and values of 2D strain rate tensors (Fig. 11). For southwest Switzerland and southwest Germany, relatively high NW–SE directed compression values of about 12 nstrain/yr were determined.[4] Areas of maximum extension with values of up to 7.5 nstrain/yr occur in central Switzerland and in western Austria (Fig. 11). From the inspection of fault plane solutions (FPS), displayed for the study area in Fig. 12, we observe in the more distal Alpine foreland a mixture of predominantly strike-slip faulting (mostly in URG), normal faulting (mostly in LRG) and some minor thrust faulting. This reflects a relatively uniform NW–SE directed compression and NE–SW extension (Fig. 4), resulting from the interference of North Atlantic ridge-push forces and forces related to the collisional interaction of the African and Eurasian plates (Müller et al., 1992; Plenefisch and Bonjer, 1997; Hinzen, 2003; Kastrup, 2002; Kastrup et al., 2004). Due to low station density, GPS data do not always fully match this first order intraplate stress/strain pattern of continental Europe.

In order to simulate on-going tectonic movements in western Europe, we divided the study area into four areas, each of which represents a rigid block that moves relative to the others. The boundaries between these blocks were defined according to differences in the velocity vectors of the permanent GPS stations, the distribution of earthquakes, and the main faults of the Rhine–Rhône rift system (ECRIS) and the Armorican Massif–Massif Central shear zone (Fig. 13). The horizontal velocity component at GPS stations and at virtual points, located on average within 50 km of the respective block borders, was estimated by assuming a uniform rotation for each of the rigid blocks. The location of the pole of rotation and the angular velocity for each block (Table 2) were estimated by a least-squares adjustment (Geiger, 2003; see Appendix A for details). The data fit well with this model, as demonstrated by the relatively small values of σ_0, that is a statistical parameter related to the residuals between real and estimated velocity values:

$$\sigma_0 = \frac{\sqrt{\sum P_i * Res\ x_i^2 + P_i * Res\ y_i^2 + P_i * Res\ z_i^2}}{\sqrt{n-u}}$$

in which P_i is the weight of the i-velocity, calculated as $P_i = \frac{1}{\sigma^2_{Vnorth_i} + \sigma^2_{Veast_i}}$ and σ_{Vnorth_i} and σ_{Veast_i} the standard deviation for the two components of the horizontal velocity, that we assumed equal to 1 mm/$\sqrt{\text{yr}}$, Res x_i, Res y_i, Res z_i are the difference (residuals) between the

[4] *1 nstrain/yr corresponds to a change of distance of 1 mm per 1000 km and year and is equivalent to $3.17 * 10^{-17}/s^{-1}$.*

Table 1
Residual values between ITRF2000 velocities and the rotation of the Eurasian plate from the combination of the AGNES, EUREF, REGAL and RGP permanent GPS networks

Stations	Initial time	Final time	Latitude	Longitude	V_{north}	V_{east}	V_{abs}	σ_{Vnorth}	σ_{Veast}
	Day.month.year	Day.month.year	Decimal degree	Decimal degree	mm/yr	mm/yr	mm/yr	mm/yr	mm/yr
ANDE	02.09.1998	30.08.2000	46.65330	8.61588	0.72	−0.33	0.79	0.71	0.71
ARDE	28.11.2001	25.06.2003	46.77639	10.20469	0.77	−1.06	1.31	0.80	0.80
BOUR	07.02.2001	25.06.2003	47.39414	7.23059	0.48	−0.52	0.71	0.65	0.65
BRST	17.04.2002	25.06.2003	48.38049	−4.49659	−0.26	−0.15	0.30	0.95	0.95
BRTZ	17.04.2002	25.06.2003	43.47196	−1.53691	−1.17	0.98	1.52	0.96	0.96
BSCN	17.04.2002	25.06.2003	47.24688	5.98938	1.15	−0.38	1.21	0.92	0.92
DAVO	09.09.1998	30.08.2000	46.81292	9.84351	1.13	−0.61	1.28	0.46	0.46
EGLT	17.04.2002	25.06.2003	45.40335	2.05199	−0.51	0.15	0.53	0.92	0.92
EPFL	27.01.1999	23.04.2003	46.52147	6.56789	1.05	0.51	1.17	0.49	0.49
ETHZ	02.09.1998	25.06.2003	47.40707	8.51053	0.76	−0.35	0.83	0.48	0.48
EXWI	26.01.2000	25.06.2003	46.95146	7.43873	−0.50	−0.31	0.59	0.54	0.54
FALE	26.12.2001	25.06.2003	46.80449	9.23030	0.32	−1.44	1.48	0.82	0.82
FCLZ	22.03.2000	25.06.2003	45.64300	5.98568	1.11	−0.14	1.12	0.55	0.55
FHBB	02.09.1998	25.06.2003	47.53387	7.63861	0.73	−0.04	0.73	0.46	0.46
FRIC	03.01.2001	25.06.2003	47.52742	8.11191	0.91	−0.52	1.05	0.63	0.63
GENE	13.12.2000	25.06.2003	46.24825	6.12808	1.14	−0.68	1.32	0.63	0.63
GRAS	02.09.1998	16.04.2003	43.75474	6.92057	1.18	−0.29	1.21	0.46	0.46
GRAZ	02.09.1998	02.05.2001	47.06713	15.49348	0.89	−0.53	1.04	0.61	0.61
HFLK	02.09.1998	22.01.2003	47.31290	11.38609	1.23	−0.79	1.46	0.48	0.48
HOHT	13.12.2000	25.06.2003	46.31941	7.76270	0.85	−0.33	0.91	0.63	0.63
HUTT	14.02.2001	25.06.2003	47.14108	7.83488	1.09	0.91	1.42	0.65	0.65
JUJO	02.09.1998	25.06.2003	46.54749	7.98490	0.09	−0.85	0.85	0.46	0.46
KARL	09.05.2001	25.06.2003	49.01125	8.41126	0.81	0.02	0.81	0.68	0.68
KREU	19.12.2001	25.06.2003	47.64129	9.16004	0.90	−0.56	1.06	0.81	0.81
LILL	17.04.2002	23.04.2003	50.61285	3.13844	−0.30	−0.29	0.42	0.99	0.99
LOMO	02.09.1998	25.06.2003	46.17257	8.78743	0.22	−0.71	0.74	0.46	0.46
LUZE	03.01.2001	25.06.2003	47.06820	8.30064	1.94	−0.51	2.01	0.63	0.63
MANS	17.04.2002	25.06.2003	48.01862	0.15528	−0.85	−1.24	1.51	0.92	0.92
MARS	08.03.2000	12.03.2003	43.27877	5.35379	0.90	−0.55	1.06	0.58	0.58
MART	07.02.2001	12.06.2002	46.12222	7.07069	1.58	−1.03	1.89	0.86	0.86
MLVL	17.04.2002	25.06.2003	48.84106	2.58731	−0.74	−0.72	1.04	0.92	0.92
MODA	22.03.2000	25.06.2003	45.21378	6.71008	0.48	−0.45	0.66	0.55	0.55
NANT	17.04.2002	25.06.2003	47.15411	−1.64537	−0.90	−0.15	0.91	1.27	1.27
NEUC	27.09.2000	25.06.2003	46.99383	6.940483	0.38	−0.53	0.65	0.60	0.60
PADO	28.11.2001	25.06.2003	45.41115	11.89606	1.02	−1.10	1.50	0.80	0.80
PAYE	20.09.2000	25.06.2003	46.81214	6.94394	0.11	0.10	0.15	0.60	0.60
PFAN	27.10.1999	25.06.2003	47.51533	9.78466	2.43	−1.51	2.86	0.52	0.52
RENN	17.04.2002	25.06.2003	48.10864	−1.66734	−0.82	−0.19	0.85	0.92	0.92
SAAN	28.11.2001	25.06.2003	46.51557	7.30129	−0.70	0.37	0.79	0.80	0.80
SAME	28.11.2001	25.06.2003	46.52925	9.87823	1.87	0.23	1.88	0.80	0.80
SANB	05.12.2001	25.06.2003	46.46383	9.18455	1.78	−1.15	2.12	0.80	0.80
SCHA	03.01.2001	25.06.2003	47.73757	8.65585	0.54	0.22	0.58	0.63	0.63
SJDV	02.09.1998	25.06.2003	45.87908	4.67657	0.58	0.02	0.58	0.46	0.46
STAB	05.12.2001	25.06.2003	45.85586	8.94164	1.81	−1.91	2.63	0.80	0.80
STCX	19.09.2001	25.06.2003	46.82239	6.50117	1.20	−0.22	1.22	0.75	0.75
STGA	13.12.2000	25.06.2003	47.44177	9.34595	0.87	−0.61	1.06	0.63	0.63
STRA	22.03.2000	06.11.2003	48.62166	7.68382	0.27	−0.21	0.34	0.56	0.56
TORI	08.03.2000	25.06.2003	45.06337	7.66128	0.86	−0.06	0.86	0.55	0.55
UZNA	03.01.2001	25.06.2003	47.21830	9.00767	1.10	−0.34	1.15	0.63	0.63
VENE	31.01.2001	25.06.2003	45.43698	12.33198	1.85	−0.60	1.95	0.65	0.65
VFCH	17.04.2002	25.06.2003	47.29420	1.71967	−0.86	0.25	0.89	0.92	0.92
WTZR	02.09.1998	25.06.2003	49.14420	12.87891	0.39	−0.54	0.67	0.46	0.46
ZIMM	02.09.1998	25.06.2003	46.87710	7.46527	0.90	−0.19	0.92	0.46	0.46
* BRUS	01.09.1996	16.05.2003	50.79782	4.35922	0.16	−0.37	0.40	0.39	0.39
* GOPE	01.09.1996	16.05.2003	49.91370	14.78562	0.65	−0.68	0.94	0.43	0.43

Table 1 (*continued*)

Stations	Initial time	Final time	Latitude	Longitude	V_{north}	V_{east}	V_{abs}	σ_{Vnorth}	σ_{Veast}
	Day.month.year	Day.month.year	Decimal degree	Decimal degree	mm/yr	mm/yr	mm/yr	mm/yr	mm/yr
* KOSG	01.09.1996	16.05.2003	52.17843	5.80964	0.61	−0.28	0.67	0.39	0.39
* POTS	01.09.1996	16.05.2003	52.37930	13.06609	0.45	−0.72	0.85	0.39	0.39
* WSRT	01.09.1996	16.05.2003	52.91461	6.60450	0.58	−0.41	0.71	0.43	0.43

All stations belong to Swisstopo, supplemented by EUREF stations (marked by a *).

real and calculated geocentric velocities within the 4-block model at the GPS stations, n is the number of observations and u the number of unknowns.

As pointed out in the discussion on lithospheric strength (Fig. 8), the assumption that the Adriatic Indenter and the Armorican Massif represent blocks of high rigidity is supported by our inferences on the spatial distribution of lithospheric strength. Particularly the border separating the blocks to the west and east of the Rhine graben corresponds to a major weakness zone.

Whereas the velocity vectors of the Paris Basin block are WSW-directed, those of the Alpine–German block are NNW-directed, that is perpendicular to those of the Paris Basin block. Between the Adriatic and the Alpine–German blocks no difference in velocity vector directions was found as both move NNW-ward. The Southern France block moves S-wards, and thus, in a different direction than the Paris Basin block (Fig. 13). Across the Rhine Rift system, the Alpine–German and Paris Basin blocks move relative to each other at a mean velocity of 0.76 mm/yr, whereas the Paris Basin and the Southern France blocks move at slightly slower rates of about 0.51 and 0.72 mm/yr, respectively (Fig. 13).

On the basis of these new velocity solutions, the strain rate field was calculated and displayed as principle axes and values of the 2D strain rate tensors (Fig. 14). The largest values of compression and extension occur in the southern and northern parts of the Rhine Rift, respectively. Whereas under the presently prevailing NW–SE-directed compressional stress field the URG subsides in response to sinistral transtensional shear, involving a lateral clock-wise rotational movement of the Paris Basin block, the LRG is subjected to nearly orthogonal NE–SW extension (Dèzes et al., 2004). These results are compatible with earthquake focal mechanisms (Fig. 12) and neotectonic activity in this area, as described in previous studies (Ahorner, 1975; Larroque et al., 1987; Larroque and Laurent, 1988; Müller et al., 1992; Delouis et al., 1993; Plenefisch and Bonjer, 1997; Bonjer, 1997; Schumacher, 2002; Hinzen, 2003; Behrmann et al., 2003; Giamboni et al., 2004). Observed directions of the principal values of strain axes are in overall agreement with those derived from focal mechanisms (Figs. 12 and 14).

Very small strain values are found along the Alpine chain (Fig. 14). This can be explained by the fact that all GPS stations located on the Alpine–German and the Adriatic blocks move in the same NW direction at slightly different absolute velocities. These results differ from those derived from FPS (Fig. 12) and other geophysical data (Eva et al., 1997, 1998; Eva and Solarino, 1998; Sue et al., 1999; Calais et al., 2000, 2002; Vigny et al., 2002; Kastrup, 2002; Sue and Tricart, 2003; Kastrup et al., 2004), which support the presence of relatively high stress and strain. This apparent discrepancy suggests that stress and strain due to horizontal motions play a minor role in the deformation of this area, and that the major contributor to stress/strain accumulation is vertical loading, for instance, due to topography or to major intra-lithospheric density contrast resulting from the nature of the collision process itself.

Relatively small strain rate values were found along the boundary that separates the Paris Basin and the Southern France blocks as a result of small velocity values estimated for this zone (Fig. 14). However, numerous earthquakes, reflecting a strike-slip tensile regime, characterize this boundary (Fig. 12; Nicolas et al., 1990; Delouis et al., 1993). This is compatible with the homogeneous stress field found for the Rhine graben area (σ_1 NW–SE-directed, σ_3 NE–SW-directed) (Delouis et al., 1993). This discrepancy may result from an abrupt change in the velocity and strain fields across the boundary between the Paris Basin and Southern France blocks.

4. Natural laboratory: Vienna Basin

The Vienna Basin is a sinistral pull-apart basin that is superimposed on the Alpine–Carpathian nappe stack, contains up to 6000 m Neogene sediments and separates the Eastern Alps from the Carpathians. Fault systems controlling the subsidence of this basin sole out at depths of 8–12 km into the basal Alpine–Carpathian thrust (Fig. 15; Royden et al., 1983; Royden, 1988; Zimmer and Wessely, 1996).

Development of the Vienna Basin commenced during the early Miocene in response to northeast-directed

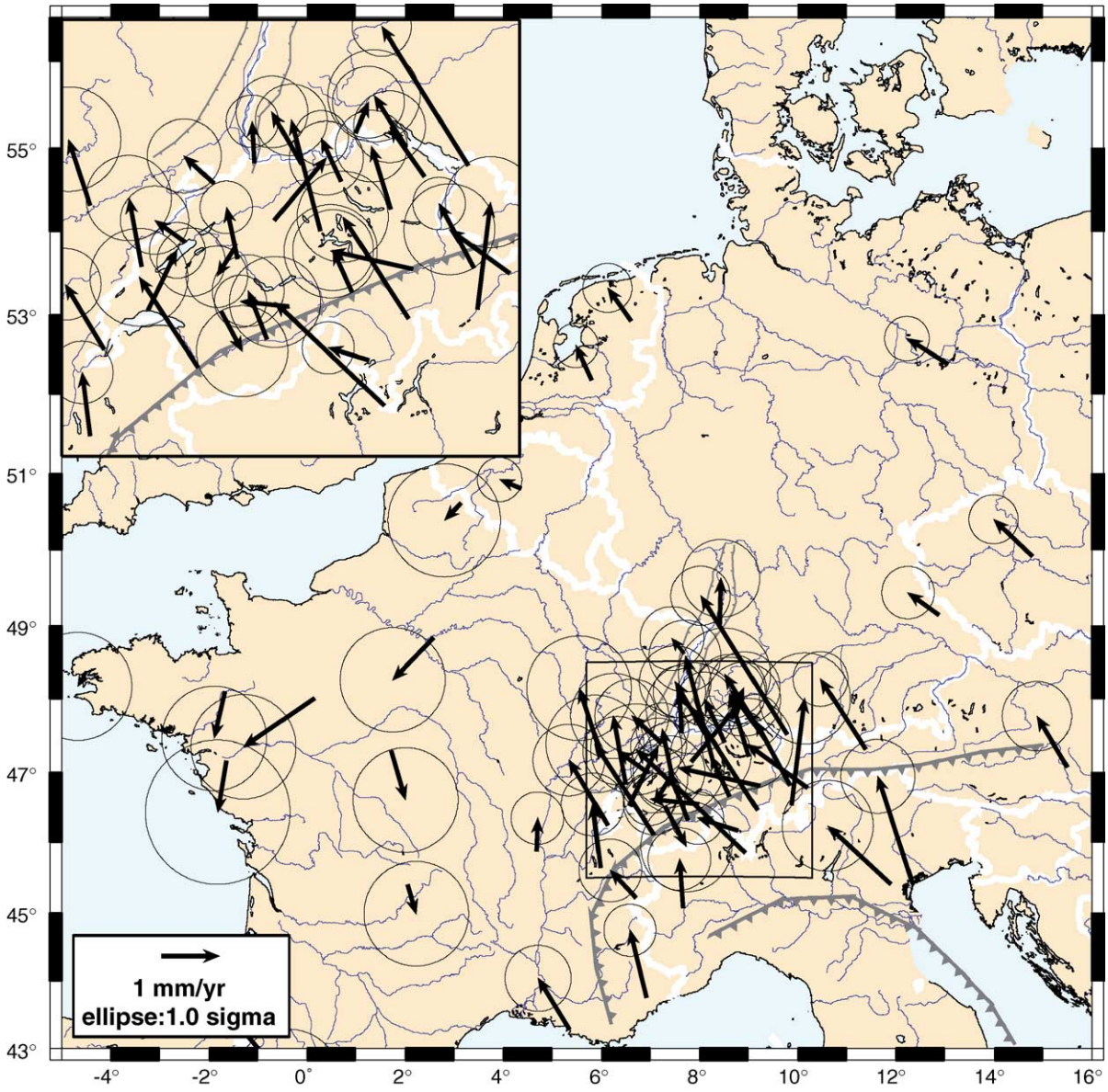

Fig. 10. Velocities relative to Eurasia for the time period 1996 to 2003. Euler pole values: Lat=57.965 deg, Long=−99.374 deg, ω=0.260 deg/My (Altamimi et al., 2002). The standard deviation, assumed equal for the two components, was calculated for each GPS permanent station on the basis of the length of the time series (σ=1 mm/yr). Permanent GPS stations located between longitudes 4° and 16° show NW-directed movement, the others, located between longitudes 4° and −5° move in a SW to S direction. White contour lines denote national borders.

lateral extrusion of the Alpine–Carpathian block, involving activation of the some 450 km long Vienna Basin Transfer Fault System (VBTF) that extends from the Central Alps trough the Mur-Mürz Valley, via the left stepping Vienna Basin into the outer Carpathians of Polish Galicia (Ratschbacher et al., 1991; Decker and Peresson, 1996; Linzer et al., 1997, 2002).

The seismically still active VBTF crosses the central parts of the Vienna Basin where it is associated with the Quaternary Mittendorf Basin (Fig. 16; Aric and Gutdeutsch, 1981; Gutdeutsch and Aric, 1988; Decker and Peresson, 1998). Earthquakes occur along the entire length of the VBTF, highlighting a 400 km long and about 30 km wide zone that parallels the Miocene fault system (Gutdeutsch and Aric, 1988). Within the Vienna Basin area, recorded seismic activity is mainly concentrated along its south-eastern border in the prolongation of seismically active zones of the Eastern Alps and Western Carpathians (Gutdeutsch and Aric, 1988).

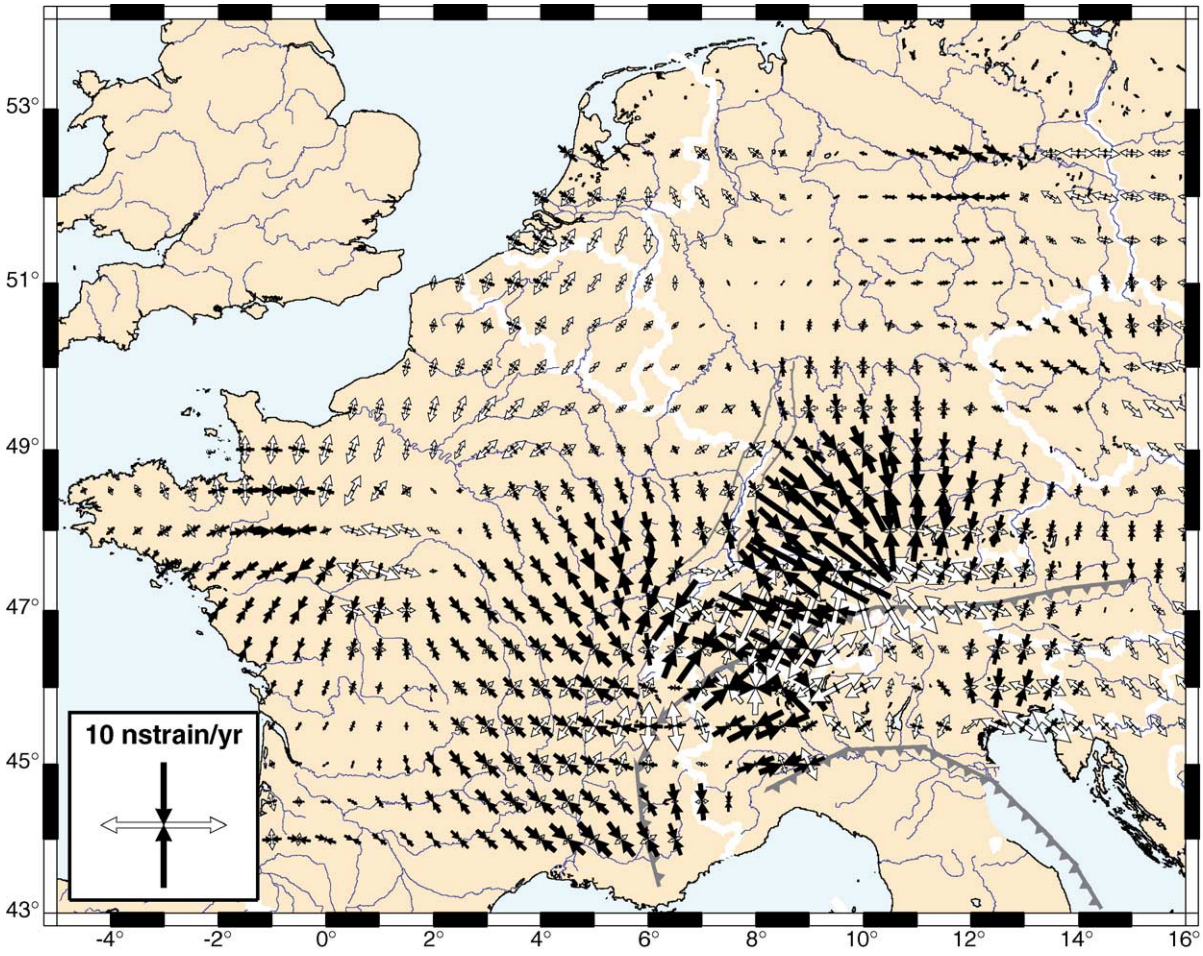

Fig. 11. Principal axes and values of strain rates obtained by the collocation method (Straub, 1996; Kahle et al., 2000). Covariance distance: 123 km; standard deviation sigma of signal: 0.85 mm/yr. Compressional and extensional axes are in black and in white, respectively. White contour lines denote the national borders. The formal error is between 4 and 7 nstrain/yr. For discussion, see text.

Stress analyses and earthquake fault plain solutions mostly indicate sinistral strike-slip faulting along north-east striking sub-vertical faults (Gangl, 1975; Marsch et al., 1990; Reinecker and Lenhardt, 1999; Reinecker, 2000). These data are consistent with GPS observations, indicating approximately 2 mm/yr sinistral movement along the VBTF (Grenerczy et al., 2000). It is not clear, however, whether at present the VFTB is still active as a pull-apart system or rather functions as a linear strike-slip fault along the southern border of the Vienna Basin (Hinsch et al., 2005a,b).

4.1. Quantifying the active kinematics

In order to assess whether or not there is presently a seismic slip deficit along the fault systems of the Vienna Basin, deformation rates along them were analyzed, using two different methods.

4.1.1. Geological balancing of a Quaternary basin

In the southern Vienna Basin, active faults outline a small-scale, actively subsiding Quaternary pull-apart basin, referred to as the Mittendorf Basin (Fig. 16). This basin is filled with up to 140 m fluvial gravel, sand and palaeo-soils that were deposited during the last 400 ky. By adopting a geometrical model for thin-skinned extensional strike-slip duplexes, Quaternary sinistral displacements along the fault system of this basin could be quantified as amounting to 1.5–2 km. This corresponds to a slip rate of 1.6–2.5 mm/yr (Fig. 16) (Decker et al., 2005).

4.1.2. Seismic slip calculations

The Austrian earthquake catalogue (ZAMG, 2001 courtesy of W. Lenhardt) was used to calculate deformation rates from seismic moment summations in order to check for possible seismic slip deficits. The

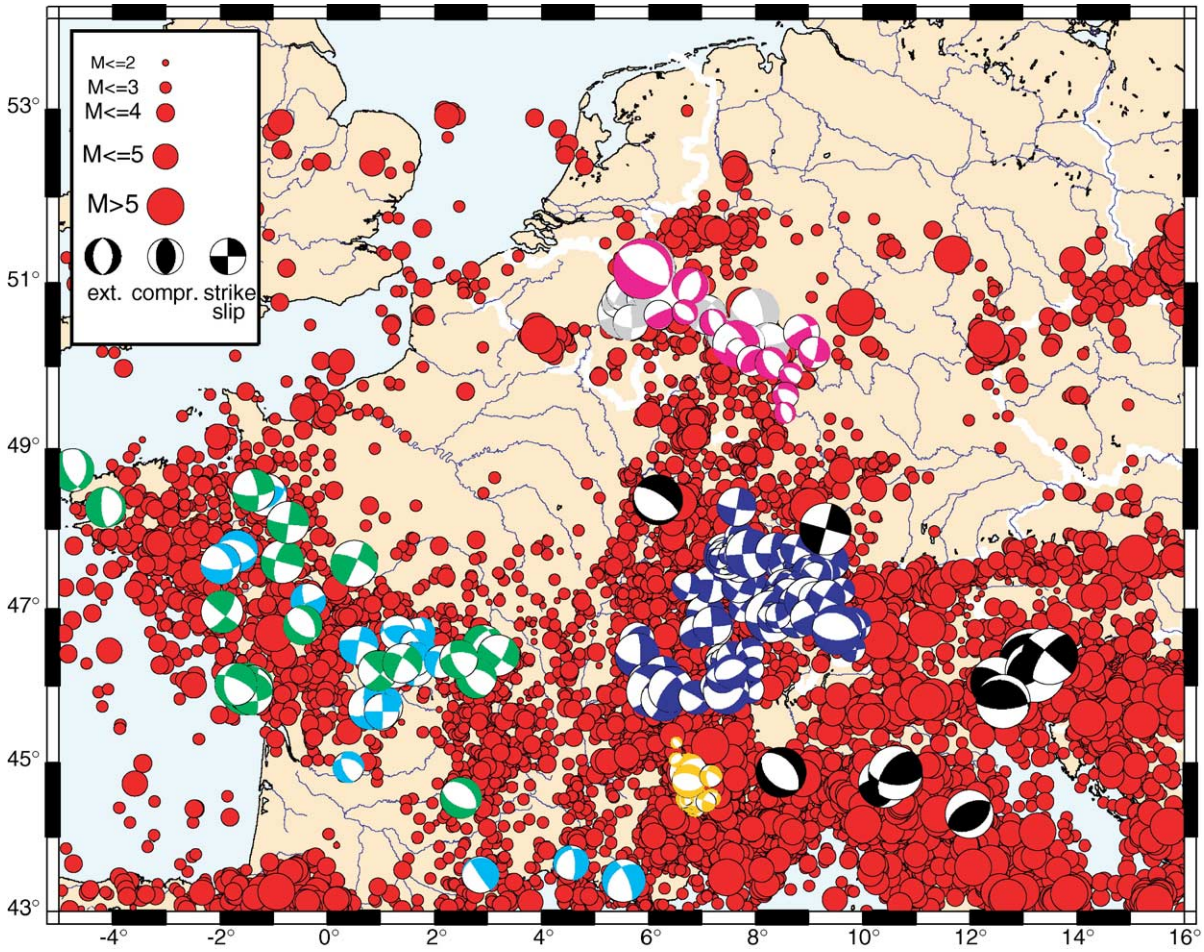

Fig. 12. Earthquakes in central Europe since 1973 from the National Earthquake Information Center (NEIC) and focal mechanism solutions (FPS) since 1961 from Hinzen, 2003 (in grey), Plenefisch and Bonjer, 1997 (in purple), Kastrup, 2002 (in blue), Sue et al., 1999 (in yellow), Nicolas et al., 1990 (in turquoise), Delouis et al., 1993 (in green), and Harvard CMT Catalog (in black).

energy released (more specific the seismic moment) through time during earthquakes along a fault system can be used to estimate the amount of seismic slip that occurred along it (Brune, 1968). For crustal faults, without special mechanical conditions, it is generally accepted, that movements along them occur mainly during earthquakes (Scholz, 1998, 2002; Holt et al., 2000). In such a case the seismic slip should approximate the slip values calculated from other methods, such as geological balancing (see above) or GPS measurements. Details on calculation steps performed for the VBTF can be found in Hinsch and Decker (2003). Results show, that calculated slip rates for the generalized fault system vary between 0.1 and 0.3 mm/yr for brittle faults extending to depths of 6–10 km. Splitting the fault into segments reveals significant along strike variations in slip velocities. Segments with less than 0.02 mm/yr seismic slip contrast with segments moving at 0.2–0.5 mm/yr (Fig. 16).

4.1.3. Seismic slip deficit

Comparing the observed seismic slip values to geodetic velocities of some 2 mm/yr (Grenerczy et al., 2000), and geologically determined strain rates of 1.6–2.4 mm/yr (Decker et al., 2005, see above), reveals the presence of a significant seismic slip deficit. Possible causes for this seismic slip deficit may be related to the chosen calculation parameters, along strike changes in mechanical conditions of the fault system, and observational data covering an incomplete seismic cycle. The most likely reason is that the seismic cycle exceeds the length of available seismological observation and that larger earthquakes than those recorded can be expected along the VBTF (cf. discussion in Hinsch and Decker, 2003).

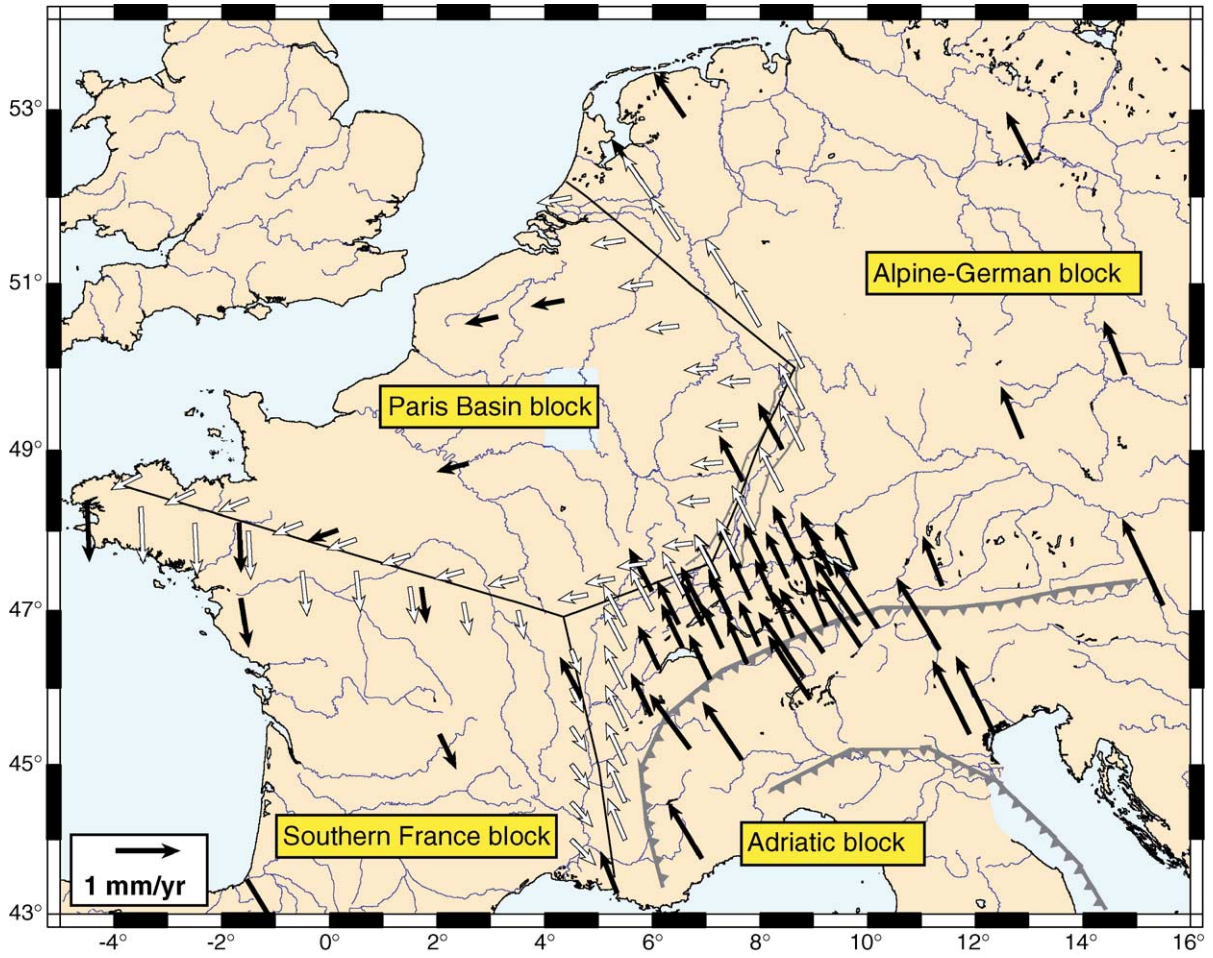

Fig. 13. Estimated velocities of crustal motion for a four-block model. Velocities at permanent GPS stations are shown as black arrows, whereas rates at virtual points, located close to the boundaries of the blocks, are shown as white arrows. Black lines represent the generalized borders between the Alpine–German block in the NE, the Paris Basin block in the NW, and the Southern France block in the SW, while the Alpine chain is taken as the border between the Alpine–German block and the Adriatic block in the SE. White contour lines denote the national borders.

4.1.4. 3-D mapping of active faults

Active faults were mapped on a multi-source basis, including published and unpublished subsurface maps of Quaternary and Neogene levels, geological maps, satellite images, 2-D and 3-D seismic data, high resolution digital elevation models for geomorphologic investigations of faults (scarps, hanging valleys etc.) and Quaternary terraces, field mapping and near surface geophysics (Decker et al., 2005; Hinsch et al., 2005a,b).

Table 2
Location of pole of rotation, angular velocity (ω) and σ_0 (a posteriori of the unit weight calculated for each block)

Blocks	Latitude	Longitude	ω	σ_0
	Decimal degree	Decimal degree	Degree/Myr	
SW	47.7850	10.4980	0.0502	0.19
SE	35.7540	−7.4030	0.0393	0.46
NW	23.5794	9.4148	0.0104	0.32
NE	29.6398	−23.015	0.0144	0.51

Based on these integrated data and methods, it was possible to constrain the active faults and their kinematic relationship in the southern Vienna Basin (south of the river Danube) and for parts of the central Vienna Basin (Fig. 17). In the southern Vienna Basin, 3-D seismic data reveals a negative flower structure with en-échelon faults (Fig. 17). This fault system is associated with a relatively linear scarp along the "Rauchenwarth Plateau" and controlled the subsidence in the Mitterndorf Basin, which contains up to 150 m of Quaternary gravels beneath the level of the present day drainage system (Hinsch et al., 2005a,b; Fig. 17). A prominent normal fault branches off at a high angle from this flower structure system and extends into the urban area of the city of Vienna (Fig. 16). Activity

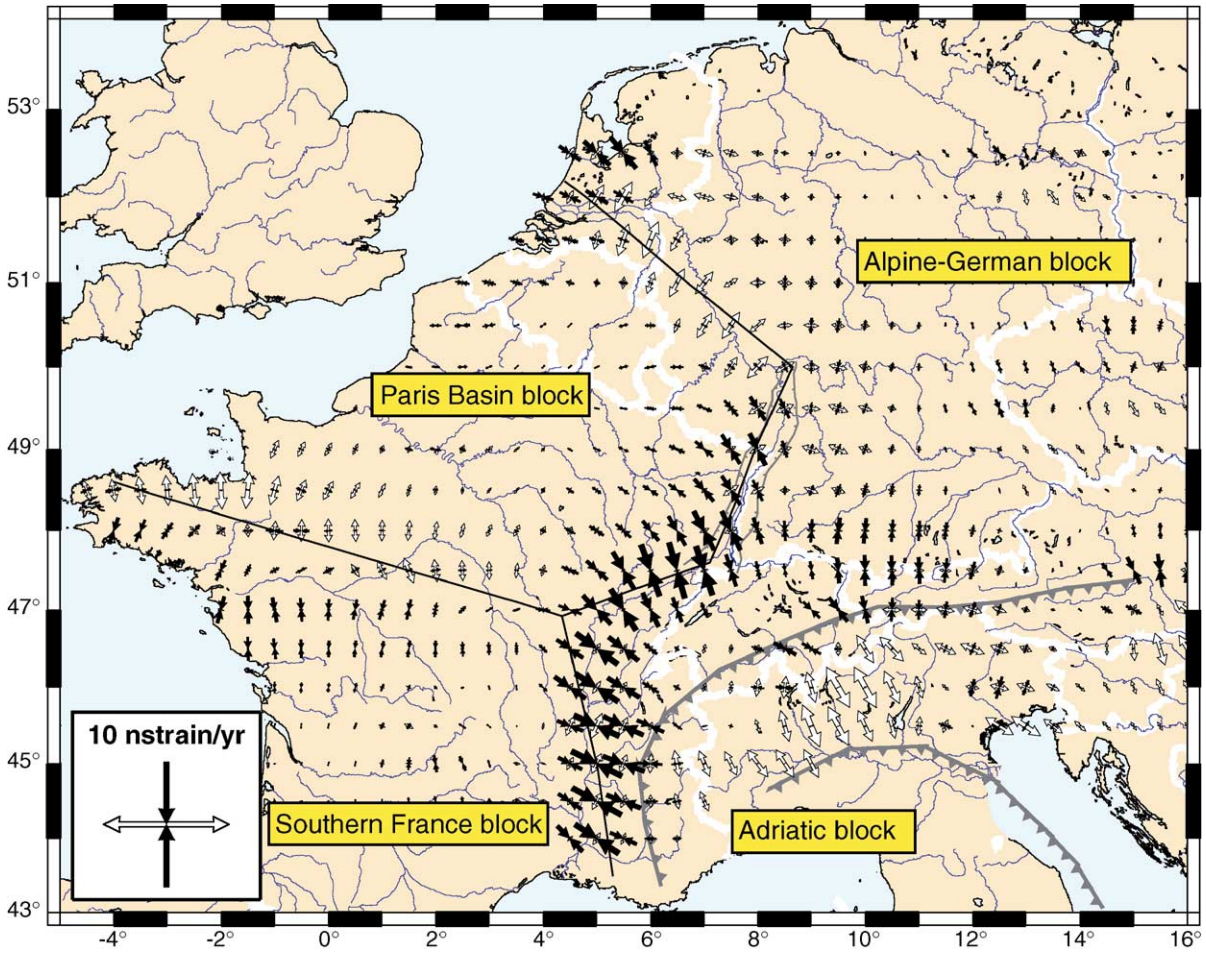

Fig. 14. Principal axes and values of strain rates reconstructed from the velocity field for the four-block model using the method of collocation (Straub, 1996; Kahle et al., 2000). Covariance distance: 77 km, sigma of signal: 0.56 mm/yr. Compressional and extensional axes are in black and in white, respectively. See Fig. 13 for convention.

along this fault is documented by the occurrence of tilted river terraces. Their tilting can be attributed to a large-scale rollover that is associated with active normal faults along the western margin of the Vienna Basin. In the central parts of the Vienna Basin, geomorphologic studies, combined with the distribution of Quaternary sediments, permitted to map active faults north of the river Danube (Decker et al., 2005). There, tilted and dissected terraces indicate the presence of a similar fault pattern as in the northern part of the southern Vienna Basin (Fig. 16). This suggests, that faults are still active throughout the Vienna Basin, even though no large scale pull-apart step-over of the seismically active principal displacement zone can be observed. The results of active fault mapping to the north and south of the river Danube are compiled in a map of active faults (Fig. 16; Hinsch et al., 2005a,b). This map also provides further information on the quality and source of interpretation, as well as on different background datasets (including digital terrain model, different geological maps).

4.1.5. Underestimated seismic potential

The above results of seismic slip calculations, compared to geologically derived strain rates, indicate that the seismic cycle exceeds the duration of the available seismological observation time and that larger earthquakes than those historically recorded must be expected to occur along the VBTF. The integration of subcrop data, the thickness of Quaternary deposits, earthquake and geophysical data and geomorphologic studies resulted in the development of a detailed active fault map. This map shows a major NE-striking, seismically active fault system in the SE part of the Vienna Basin from which numerous faults branch off. Three of these branch faults, which were at least active during the Pleistocene, pass through the urban

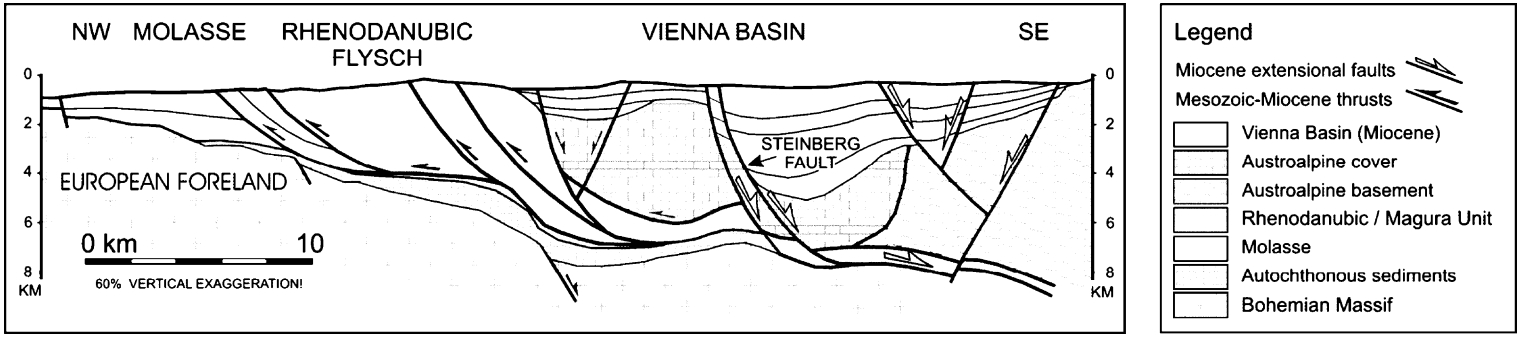

Fig. 15. Cross-section through the northern Vienna Basin (after Wessely, 1993). The major listric normal faults (Steinberg fault system, 5.6 km vertical throw) root in the Alpine–Carpathian sole thrust. Location of these major faults at the NW basin margin controls the asymmetrical geometry of the basin and the NW tilt of its sedimentary fill.

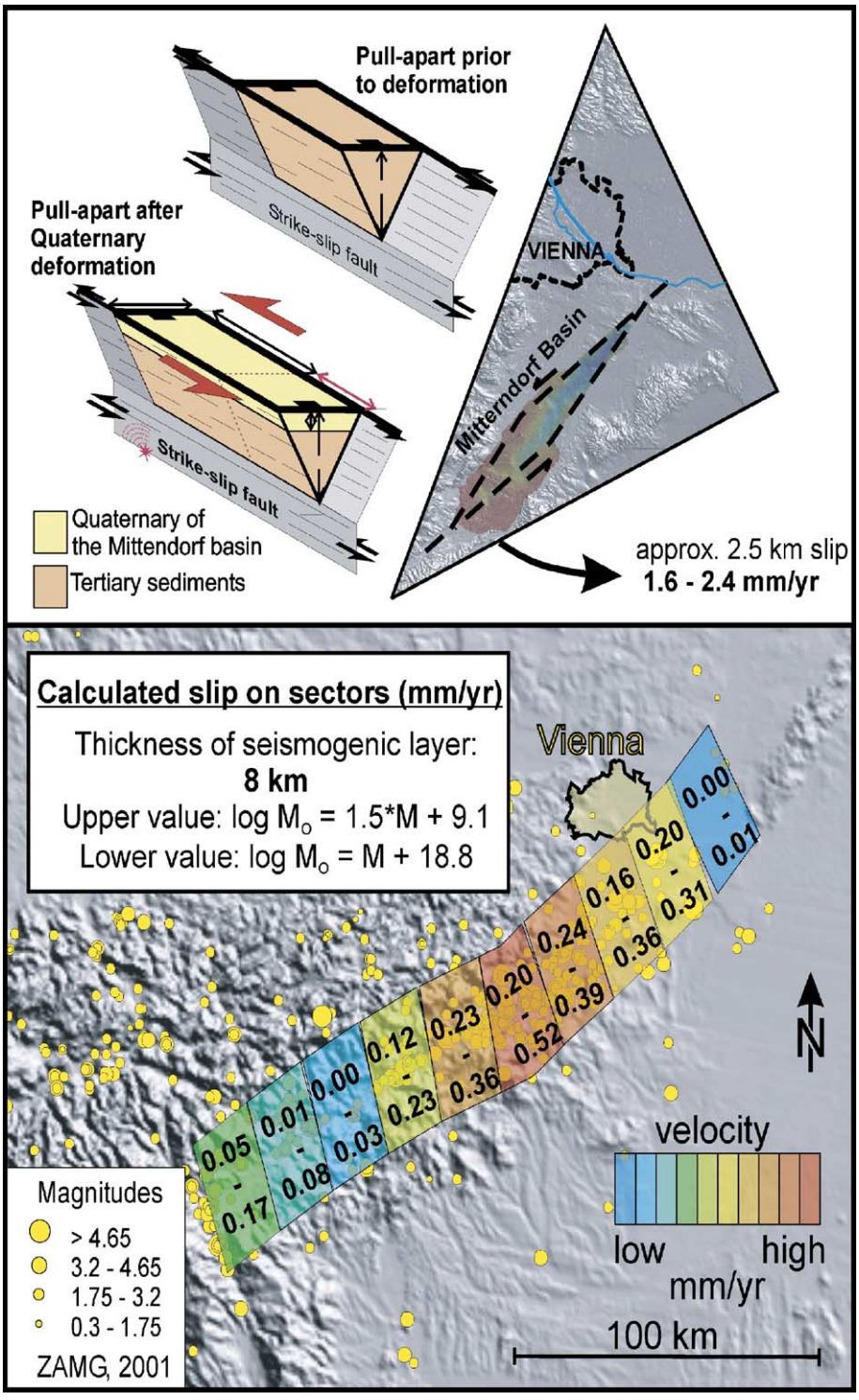

Fig. 16. Assessing deformation rates. Upper: schematic geometry of the shoebox model used for calculating Quaternary fault offset and average slip rates from the subsidence of the Mitterndorf Basin, Southern Vienna Basin (modified after Decker et al., 2005). Lower: calculated seismic slip rates from cumulative scalar seismic moments for arbitrarily selected fault sectors along the Austrian part of the Vienna Basin Transfer Fault (minimum thickness of the brittle crust: 8 km). The velocity range of individual sectors results from the use of two different empirical relationships for magnitude to moment conversion (Purcaru and Berckhemer, 1978; Hanks and Kanamori, 1979). All segments appear to be seismically active but show significant differences of calculated seismic slip (0–0.52 mm/yr; modified from Hinsch and Decker, 2003).

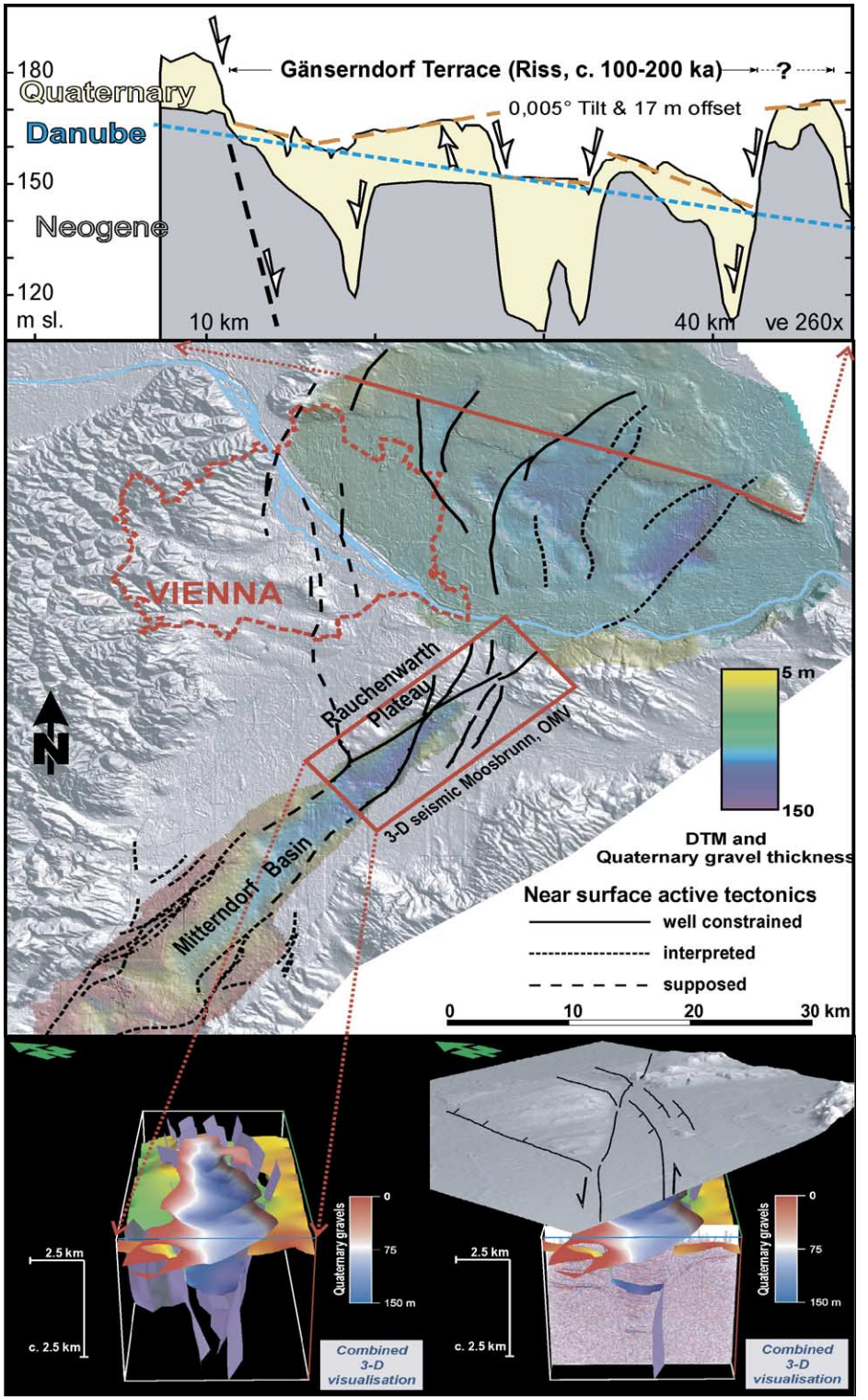

Fig. 17. Multisource mapping of active faults in the Vienna Basin. Upper: tilted terraces of the river Danube and subsided Quaternary basins indicate subsurface segmentation by faults and associated block tilting. Center: compilation of active faults inferred from data described in Hinsch et al. (2005a,b) and published data referred to in text. Background image: digital elevation model (grey) and thickness of Quaternary gravels (coloured). Lower: 3-D perspective view of integrated faults, horizons, seismic data and digital elevation model used for fault interpretation. Seismic data: courtesy of OMV AG, Austria.

centre of Vienna (Fig. 17). However, most of these branch faults have not been the loci of recorded earthquakes.

Accordingly, these faults were not taken into consideration in the available seismic hazard maps, which are exclusively based on historical and instrumental earth-

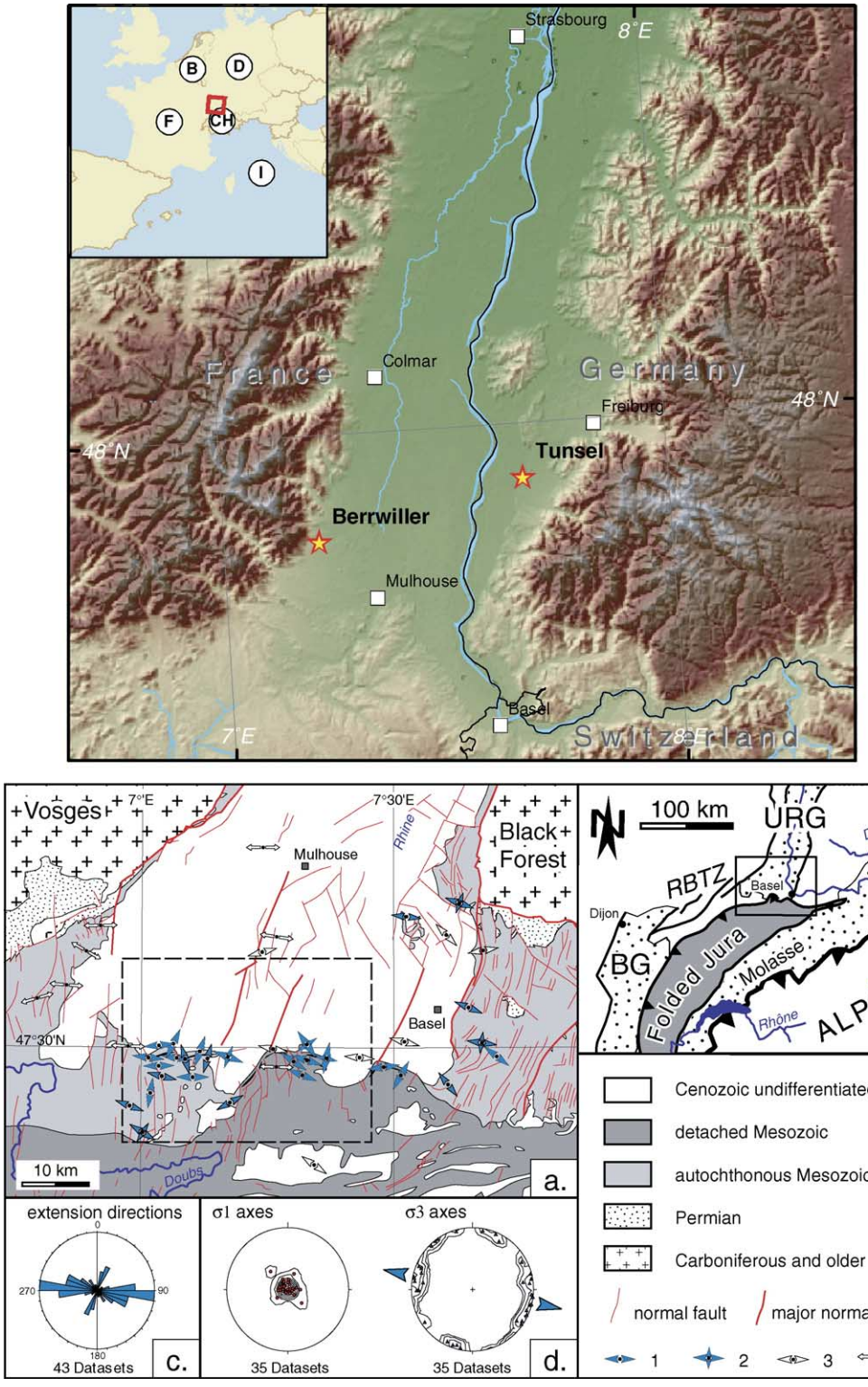

quake data. The underestimated seismic potential of these faults, in combination with the economical relevance of the region (2.4 million Austrian inhabitants in the Vienna Basin, producing ca. 45% of the Austrian GDP), calls for a seismic hazard re-assessment that includes data from the active fault datasets generated by this study.

5. Natural laboratory: Upper Rhine Graben

Studies carried out in the framework of ENTEC address particularly the southern parts of URG (Fig. 18a), an area of increased seismic hazard (Fig. 1), as for instance evidenced by the 1356 earthquake that severely damaged the city of Basel. Despite dedicated research, the seismic source of this historical earthquake (strike slip, thrust or normal faulting, reactivation of Oligocene or Permo–Carboniferous faults) has not yet been unequivocally identified (Meyer et al., 1994; Nivière and Winter, 2000; Meghraoui et al., 2001; Müller et al., 2002; Lambert et al., 2005). Furthermore, it is not clear whether on-going deformation of the North-Alpine foreland at convergence rates of about 1 mm/yr or less (Müller et al., 2002; Ustaszewski et al., 2005b) is partitioned between the crystalline basement (including Permo–Carboniferous troughs) and its sedimentary cover along rheologically weak Middle and Upper Triassic evaporite layers (Müller et al., 1987). During the Pliocene, shortening in the Jura Mountains propagated north-westward and northward and encroached during Late Pliocene times on the southern margin of the URG (Nivière and Winter, 2000; Giamboni et al., 2004). This late phase of Jura Mountain folding was accompanied by a change from previously "thin-" to "thick-skinned" deformation (Philippe et al., 1996; Becker, 2000; Dèzes et al., 2004). Solving these problems is a key issue in assessing the seismic hazard potential of the southern URG area that requires knowledge on fault kinematics during the geological past. Therefore, ENTEC research in the southernmost URG concentrated on detailed mapping of basement faults and kinematic reconstructions throughout time, integrating available geophysical data with results of structural field studies and geomorphologic observations.

5.1. Evolution and kinematics of the southern parts of the URG

The NNE striking URG is delimited to the south by an ENE-trending intracontinental transform fault system, referred to as the Rhine–Bresse or Burgundy Transfer Zone (RBTZ; Fig. 18b; Bergerat, 1977). Localisation of the RBTZ was pre-conditioned by basement faults outlining a system of Permo–Carboniferous troughs (Ziegler et al., 2004). Rifting in the URG was initiated during the late Priabonian under a regional northerly directed compressional stress field (Bergerat, 1987), causing extensional and transtensional reactivation of NNE- and ENE-trending Late Palaeozoic fracture systems. The resulting extensional strain across the evolving graben was WNW–ESE directed, roughly orthogonal to its axis (Schumacher, 2002; Ustaszewski et al., 2005a).

At the southern end of the URG, the late Eocene rifting phase gave rise to the subsidence of half-grabens controlled by NNE-trending normal faults (Fig. 19a). At the same time, the ENE-trending basement faults of the RBTZ were transtensionally reactivated in a sinistral mode. Strike-slip faulting within the basement was accommodated in its sedimentary cover mainly by the development of en-échelon aligned extensional flexures, involving locally confined N–S-extension. Thus, at the intersection of the URG and RBTZ, contemporaneous activity along NNE-trending normal faults and ENE-oriented extensional flexures reflect development of a stress regime that approaches radial extension (Figs. 18 and 19; Ustaszewski et al., 2005b).

A northerly directed stress regime persisted during the Oligocene, controlling the main rifting phase of the URG, but permutated during the early Miocene to a northwest-directed one under which the northern parts of the URG continued to subside without interruption until Quaternary times (Buchner, 1981; Schumacher, 2002; Dèzes et al., 2004). By contrast, the southern parts of the URG ceased to subside during the Burdigalian when uplift of the Vosges–Black Forest Arch began (Laubscher, 1992). Development of this arch, which entailed uplift of the southern part of the URG

Fig. 18. Top panel: Topographic map and DEM of southern parts of the Upper Rhine Graben. Inset: location map. Stars denote locations of profiles shown in Figs. 35, 36, and 37. Lower panel: (a) Tectonic map of the southernmost URG and adjacent Jura Mountains. Eo-/Oligocene extension directions are shown by diverging arrows. Note deviating extension directions in the vicinity of flexures delimiting the URG to the south. Dashed rectangle shows outlines of Fig. 19. (b) Location of study area at the junction between the URG and Rhine–Bresse Transfer Zone (RBTZ), which links the URG and contemporaneous Bresse Graben (BG). (c) Frequency distribution of extension directions (interval width 10°) shown in (a). (d) Contoured Sigma-1- and Sigma-3-axes obtained from 35 locations. The scatter of Sigma-3-axes is due to interference between regional and local stresses at the URG–RBTZ boundary. Legend: 1: extension, 2: radial extension (1 and 2 inferred from analysis of striated faults), 3: extension direction inferred from conjugated faults, 4: extension direction compiled from Larroque and Laurent (1988).

and deep truncation of its sedimentary fill (Schumacher, 2002), is attributed to lithospheric folding in response to the build-up of a NW-directed stress field that reflects increased collisional coupling between the Alpine Orogen and its northern foreland. Subsidence of the southern part of the URG resumed only during the late

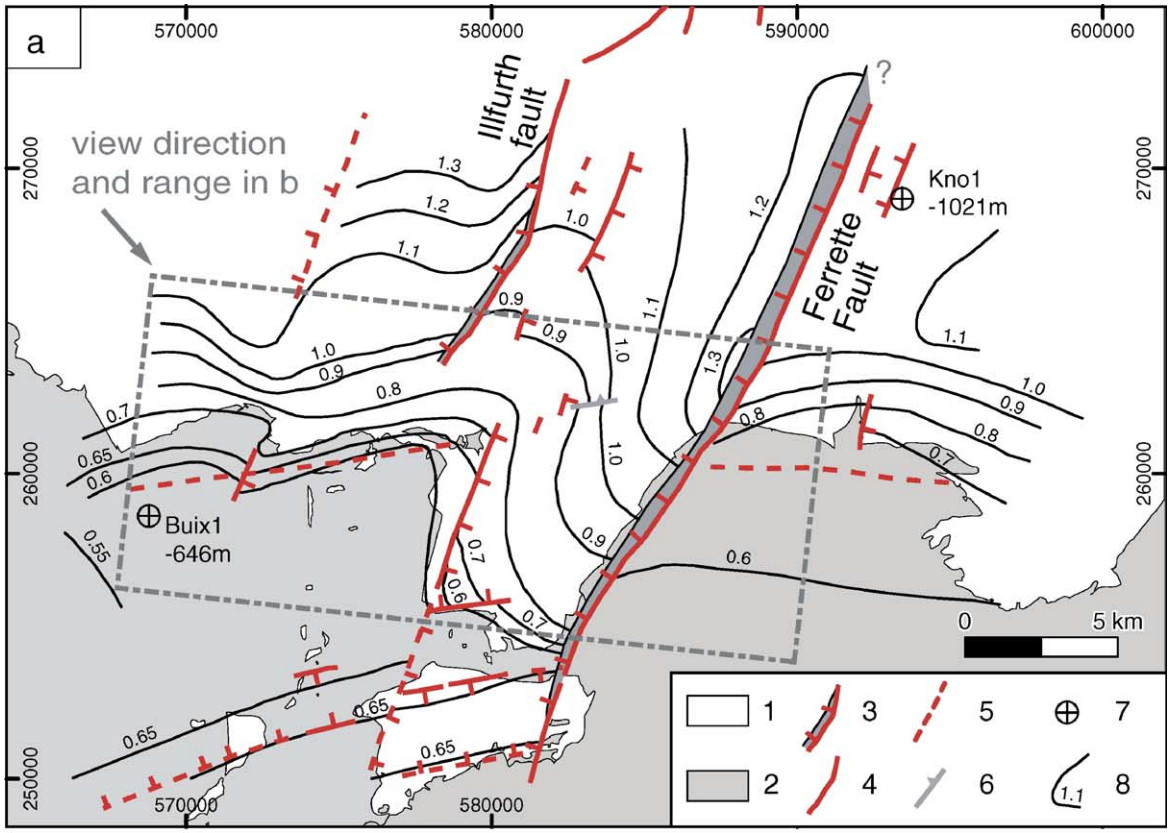

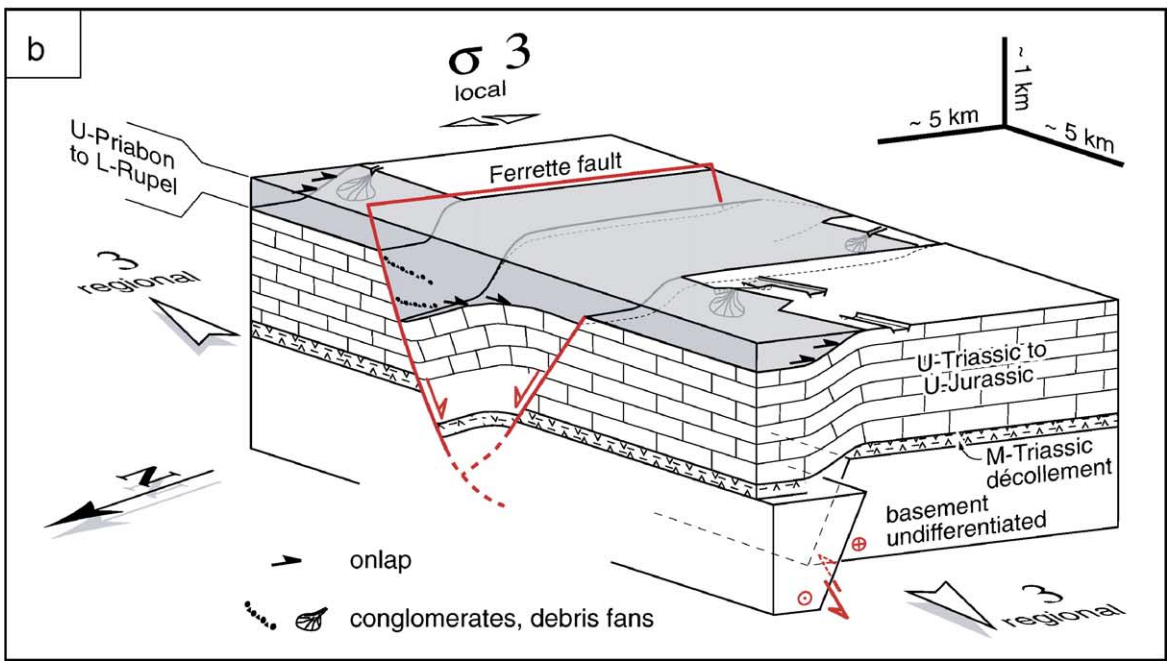

Pliocene when uplift of the Vosges–Black Forest Arch slowed down or ended and the effects of crustal extension/transtension became dominant again (Dèzes et al., 2004). Correspondingly, a major hiatus in the sedimentary record of the southern part of the URG prevents the analysis of its evolution during late Oligocene to early Pliocene times.

Post-late Pliocene to recent uplift of and shortening in the frontal parts of the Jura Mountains along the southern margin of the URG is documented by deformation of late Pliocene fluvial gravels, as well as by progressive deflection and capture of rivers (Fig. 20; Giamboni et al., 2004). This deformation was presumably controlled by thick-skinned reactivation of ENE-striking basement faults, as evidenced by reflection-seismic sections which demonstrate the spatial coincidence of en-échelon surface anticlines and basement faults (Fig. 21). Focal plane mechanisms of upper crustal earthquakes show mainly strike-slip characteristics and a consistently NW–SE-directed greatest principal stress (Plenefisch and Bonjer, 1997; Kastrup et al., 2004). Nodal plane orientations, however, suggest that only NNE- and NW-trending faults are being reactivated. The reactivation of ENE-trending basement faults, as suggested by geological evidence, is not evidenced by seismotectonics. This discrepancy is the focus of on-going research.

5.2. URG rifting modelling

Crustal extension across the southern URG accounts for a net stretching factor of 1.2 (Villemin et al., 1986), corresponding to a total extensional strain of 6–7 km (Brun et al., 1992). During the late Eocene and Oligocene, deformation was concentrated on the NNE-striking main border faults, which obliquely cross-cut Palaeozoic structures (Sittler, 1969). During the early Miocene, deformation progressively migrated towards the interior of the evolving graben as initial E–W-directed extension rotated counter-clockwise to a nearly NE–SW-directed one (Behrmann et al., 2003; Bertrand et al., 2005). The modelling study discussed below covers parts of the southern URG and its shoulders in the Colmar and Freiburg–Offenburg area (Fig. 22).

The rifting history of the southern URG was analyzed by applying numerical modelling techniques, based on finite element methods and contact mechanics. Both forward and backward models were carried out to address two major aspects of rifting processes, namely the kinematics of extension and fault propagation. The forward model aimed at defining the evolution of faulting during the rifting phase, and at analyzing the relationship between the strike of faults and the extension direction (orthogonal versus oblique extension) (Fig. 22). The backward model focused on the kinematics of rifting in the southern parts of the URG. Retro-deformation of this graben segment helped to define the finite amount of extension that occurred across it, the potential contribution of strike-slip deformation to observed displacements, and the cumulate amount of subsidence and possible post-rift uplift (Fig. 23).

5.2.1. Discussion of forward model

Qualitative results show that deformation is mainly concentrated on contact zones, the border faults, while the central part of the graben remains less deformed. However, in case of oblique extension, deformation is not necessarily restricted to the border faults: a narrow band of high strain and brittle behaviour develops in the centre of the graben along its axis (Fig. 22) (Cornu and Bertrand, 2005a). This zone is the likely location of subsequent faults that develop during oblique rifting. For this segment of the URG, the narrow zone of high strain and brittle behaviour closely fits the surface trace of the Rhine River Fault (Fig. 23).

It is, however, not possible to propose from this model the sense of displacement on a newly formed fault along the graben axis, as most of the vertical displacement is accommodated along the border faults. Moreover, because the zone of high brittle behaviour is rather vertical, one would expect strike-slip motion combined with a normal component. A plausible rifting scenario for the URG could be, as proposed by Bertrand et al. (2005), that initially the border faults ac-

Fig. 19. (a) Base Mesozoic contours and faults at the Rhine Graben–Jura boundary SW of Basel (based on reflection-seismic data). Seismic reference datum = 500 m. Legend: 1: Tertiary undifferentiated, 2: Mesozoic undifferentiated, 3: normal fault, barbs on the hangingwall side, fault heave shown in grey, 4: normal fault, 5: normal fault inferred, 6: transpressively reactivated fault, 7: exploration wells penetrating base Mesozoic surface (depth in m below sea level), 8: isochrones in seconds two-way travel time (1 s TWT = approx. 1700 m). Numbers on map edges: Swiss National coordinates. Dashed rectangle shows outlines of block model in b. (b) Block diagram illustrating contemporaneous development of halfgrabens and extensional flexures under regional WNW-oriented extension during the Upper Priabonian to Lower Rupelian. Interference of growth faulting along NNE-oriented, Rhine Graben-parallel faults and sinistral transtensive movements along ENE-striking (reactivated) Late Palaeozoic faults allows for the development of localised depocenters. Vertical scale and fault displacements exaggerated, Illfurth fault omitted for legibility.

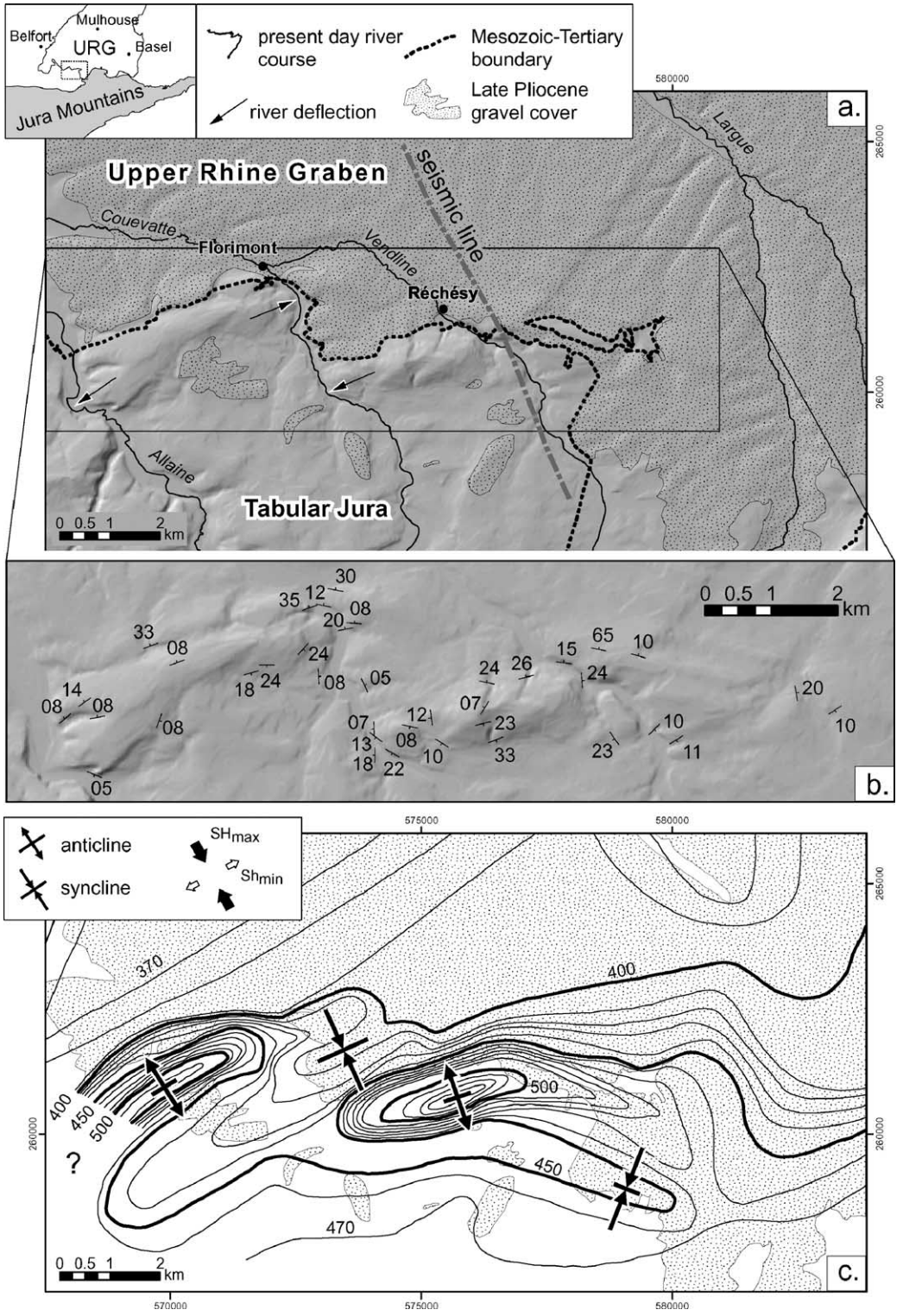

Fig. 20. (a) Shaded relief map showing juvenile morphology of two ENE-trending en-échelon aligned peri-anticlines SW Basel (DHM 25, reproduced by permission of Swisstopo, BA045927). Note deflection of Allaine and Coeuvatte rivers near fold hinges. (b) Close-up of en-échelon aligned anticlines with dip azimuths measured in Upper Jurassic and Palaeogene sediments, illustrating that topography results from folding of the sediments. (c) Isohypses of the base of Late Pliocene gravels (outline of figure identical to a) showing anticline–syncline pairs corresponding closely to topography and the configuration of underlying Mesozoic–Palaeogene sediments. These structures developed after the deposition of the Late Pliocene gravels (Post-2.9 Ma). Top left insert: recent stress field, according to earthquake focal mechanism (Plenefisch and Bonjer, 1997; Kastrup et al., 2004).

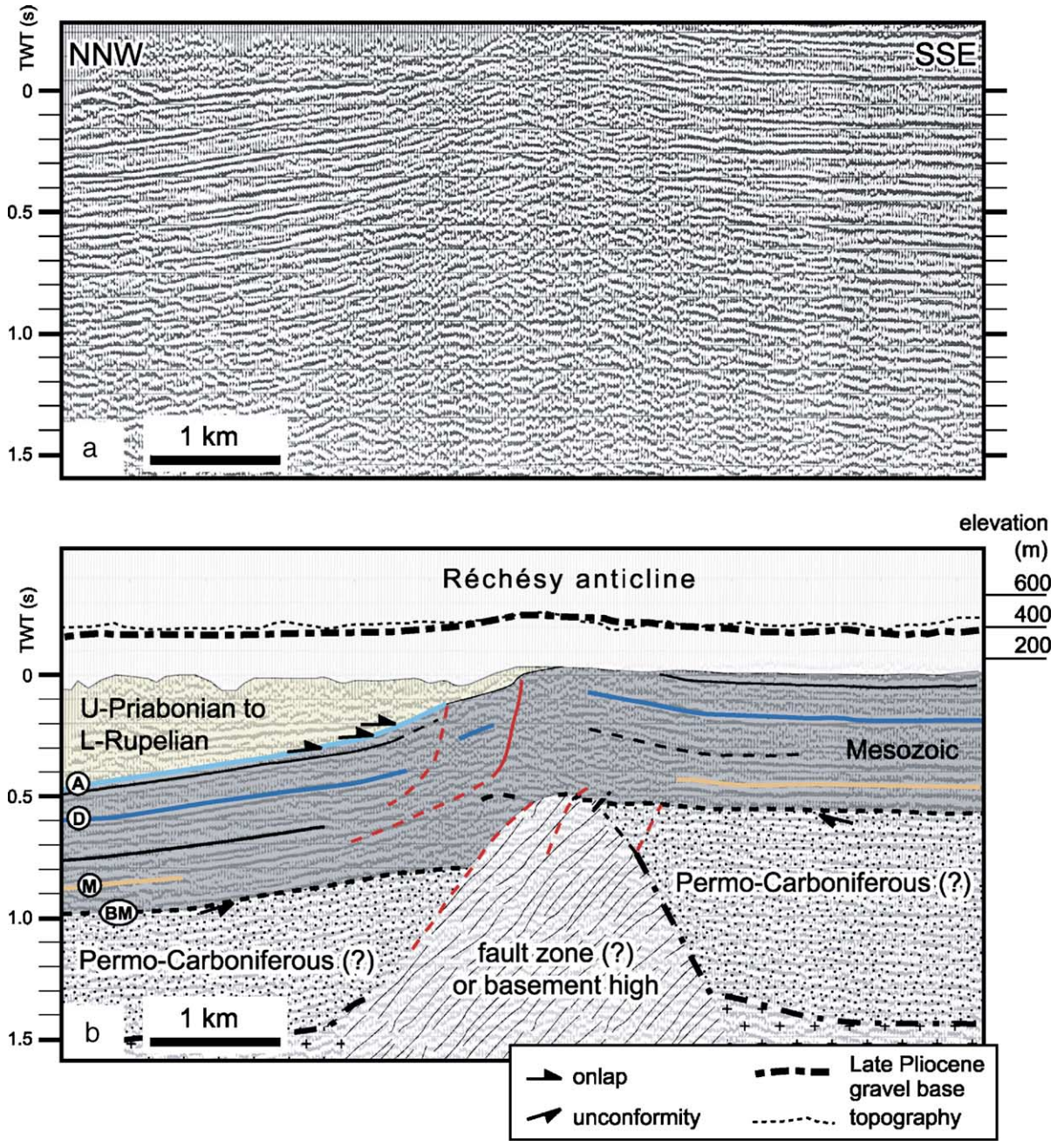

Fig. 21. Reflection-seismic line crossing a reactivated Palaeogene flexure in Mesozoic sediments (data: courtesy of Shell International EP). For location of the section see Fig. 20a) stacked, uninterpreted section, b) interpreted section. BM = base Mesozoic, M = top Muschelkalk, D = top Dogger, A = top Malm, hatched = fault zone associated with Late Palaeozoic faults. The structure of the Base of the Late Pliocene gravels (cf. Fig. 20c) and the topography are superimposed on the figure. The metric scale coincides with the depth in seconds two-way travel time (calculated using seismic velocities from nearby boreholes). Note close correlation between Mesozoic reflectors and Pliocene gravel base. Moreover, fold crests in both gravels and Mesozoic sediments coincide and are located precisely above the basement fault zone, suggesting thick-skinned origin of the post-Late Pliocene folds.

commodated nearly orthogonal extension, and that, as the extension axis rotated counter-clockwise, new faults developed inside the graben. The models suggest that one of the most important features is the Rhine River fault that probably accommodated a significant amount of strike-slip movement whilst most of the normal displacement was taken up by the Main Border and associated faults.

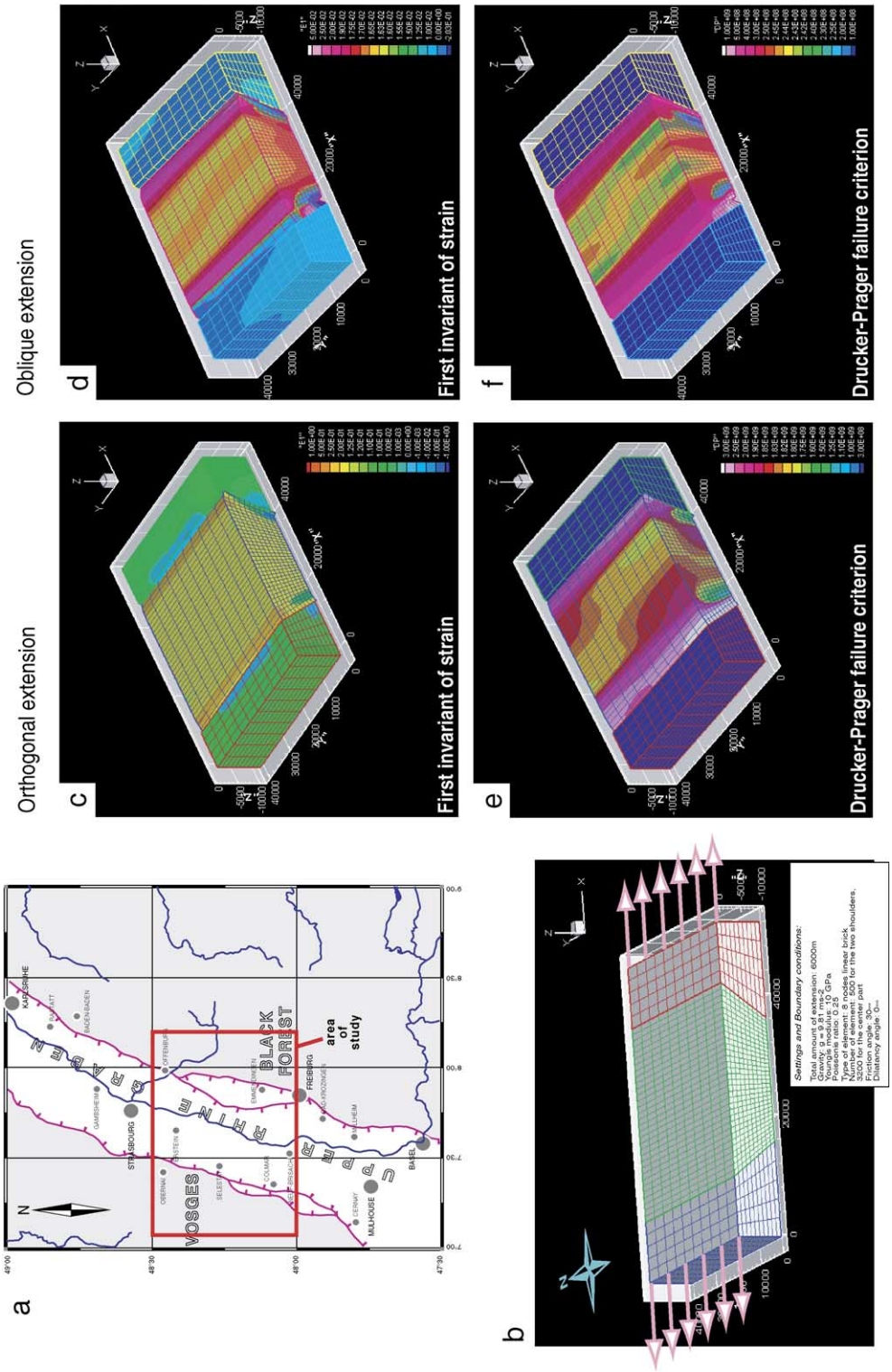

Fig. 22. (a) Sketch map of the southern part of the Upper Rhine Graben, showing the western and eastern main border faults, and the area covered by the numerical models shown in Fig. 23, denoted by the red rectangle. (b) Initial (i.e. pre-rift) geometry of the studied graben segment, used for the forward model. The two lateral blocks correspond to the future graben shoulders (i.e. Vosges and Black Forest Mountains to the west and the east, respectively). Their contact zones with the central block correspond to the border faults delimiting the Upper Rhine Graben. Right panel: Results of the forward model. Both purely orthogonal and partly oblique extension scenarios were tested. Results are presented in terms of the first invariant of strain E1 (sum of the diagonal terms of the strain tensor): (c) orthogonal and (d) oblique extension. And in terms of the Drucker–Prager (DP) failure criterion (numerical equivalent of a Mohr–Coulomb criterion, see Appendix B for further details): (e) orthogonal and (f) oblique extension. Cartesian coordinates are in meters.

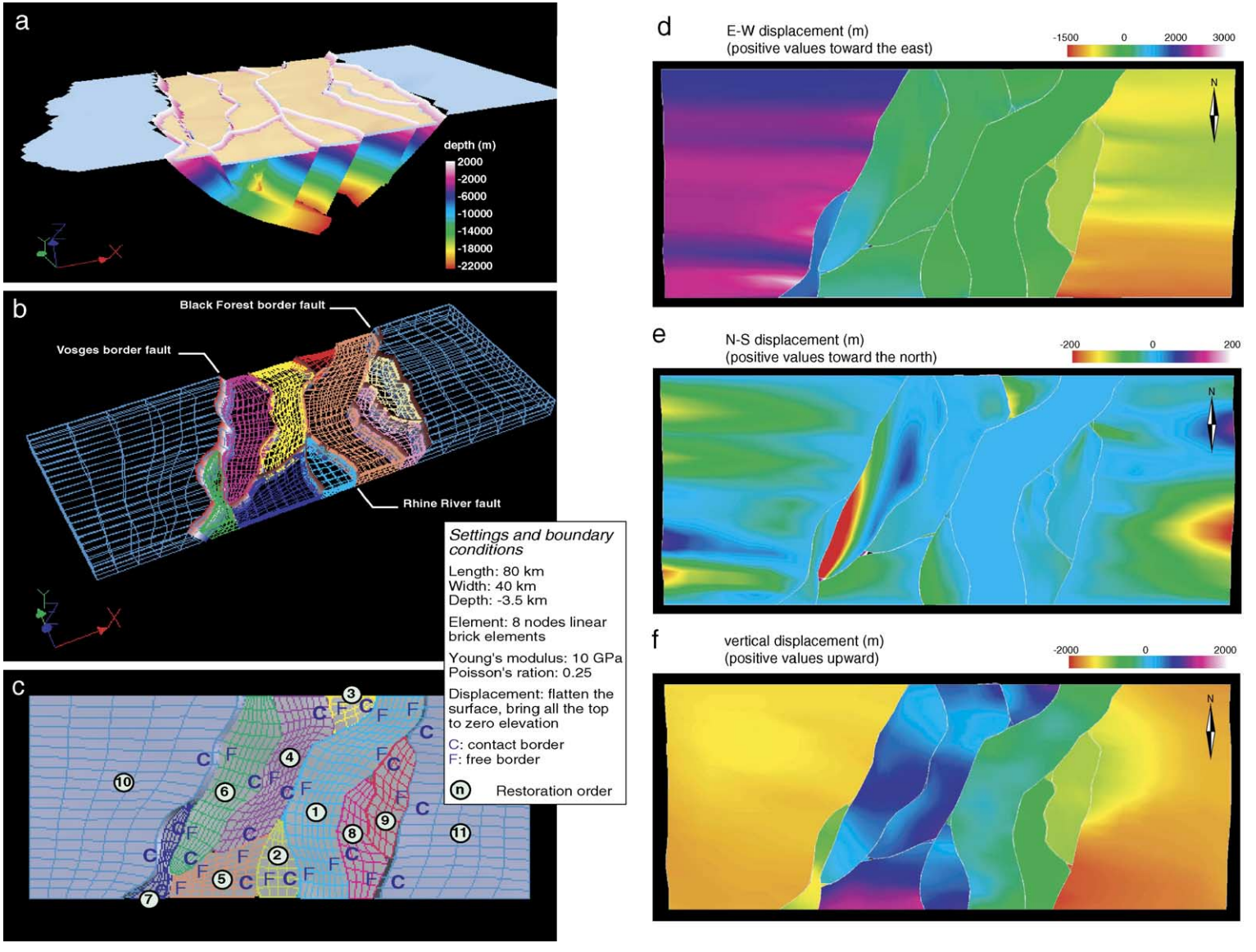

Fig. 23. Left panel: Construction of initial multi-block domain used for backward modelling (for location see Fig. 22). (a) Present-day geometry of the geological domain. (b) Finite elements domain built from this geological domain. (c) Contact sequence of movement used for backward modelling the contact borders, (C) are borders containing the "slave" nodes and free borders, (F) those containing "target" nodes. Right panel: Results of backward model, presented in terms of displacement (m), showing the top surface of all blocks, (d) displacement along the E–W x-axis, (e) displacement along the N–S y-axis, (f) displacement along the vertical z-axis.

5.2.2. Discussion of backward model

Displacement components along the 3 axes provide information on rifting processes in the URG. As previously suggested by forward modelling and Cornu and Bertrand (2005b), the majority of deformation is initially accommodated along the border faults (Fig. 23d,e for heave and 23f for throw) with only a minor part being distributed within the graben itself. This confirms the model of Behrmann et al. (2003) and Bertrand et al. (2005) which suggests that deformation first concentrates on the main border faults whereas localized deformation occurs within the graben during later rifting stages.

Despite strict boundary conditions and a purely orthogonal rifting scenario, components of strike-slip motion have been identified along all faults. Strike-slip components range from a few tens to about 100 m, as in the previous simple backward model (Cornu and Bertrand, 2005b). In case of partly oblique rifting, it is likely, that the URG accommodated a significant component of strike-slip motion. At this point, we are unable to quantify the cumulated strike-slip deformation component as no trace of strike-slip deformation has yet been identified in the field.

Although the main border faults accommodated the bulk of deformation, the Rhine River fault played an important role in the evolution of the URG. This fault, despite having a relatively low heave owing to its steep dip, accommodated a significant throw, and marks the boundary between the shallow eastern and the deep western part of the southern URG. Each fault block, although cut by secondary faults that accommodate smaller displacements, behaves more or less as a single block.

Summarizing, the forward model provides new insight into the possible faulting history of the URG. It clearly shows that (1) whatever the extension direction, deformation is mainly accommodated along the border faults, and (2) the observed fault pattern can only be reproduced under conditions of oblique extension.

The backward model is in good agreement with the results of previous studies (Behrmann et al., 2003; Cornu and Bertrand, 2005b; Bertrand et al., 2005) which show that (1) the maximum deformation occurs along the border faults, and (2) maximum subsidence is centred on the south-western part of the graben. In addition, the direction and magnitude of observed strike-slip values are compatible with those of a simple 4-block model (Cornu and Bertrand, 2005b). Although these lateral motions are mainly a function of fault orientation, an oblique extension component is required for the development of the observed fault pattern.

From the backward and forward models it appears that opening of the URG involved a component of oblique extension, and that the central Rhine River fault played a major role during the rifting history. Therefore, the Rhine River fault deserves further attention in future seismotectonic studies as it cuts densely populated and industrialized areas.

5.3. Seismic tomography

For the southern parts of the URG, a combined interpretation of regional teleseismic travel time tomography (Lopes Cardozo et al., 2005) and local earthquake tomography (Lopes Cardozo and Granet, 2003) provides a crucial link between the structure of the entire lithosphere and the structures in the upper crust (Lopes Cardozo and Granet, 2005). Since both methods use the inversion of P-wave travel time residuals to retrieve the seismic velocity structure of the Earth, a comparison of the results should be rather straightforward (Fig. 24).

Layer 4 (75–100 km) of the teleseismic model shows mainly ENE–WSW oriented structures that parallel the fabric of the Variscan basement; such pre-existing structures played an important role during recent deformation. Layers 2 and 3 (25–75 km) show dominantly N30° to N35° trending structures. The structures of the uppermost layer (10–25 km) show the same N25° trending structures as those derived from the upper crustal velocity model.

The total absence of structures aligned with the N10° trend of the URG in the two seismic velocity models reflects that rifting had limited effects on the configuration of the crust and mantle-lithosphere. On the other hand, the dominance of structures aligned with the structural grain of the Variscan Orogen shows that the present-day structure of the crust and mantle-lithosphere dates back to the Late Palaeozoic (see also Ziegler et al., 2004).

Results of a combined interpretation of both tomographic surveys and SKS and P_n anisotropy studies permit to evaluate possible models for the development of the URG (Lopes Cardozo, 2004). The absence of a distinct pulled-up of the lithosphere–asthenosphere boundary beneath the southern parts of the URG excludes a uniform pure-shear rifting model (McKenzie, 1978).

On the other hand, the simple-shear model (Wernicke, 1981) implies that during crustal extension thinning of the mantle-lithosphere is laterally offset from the rift axis by a shear that cuts through the entire litho-

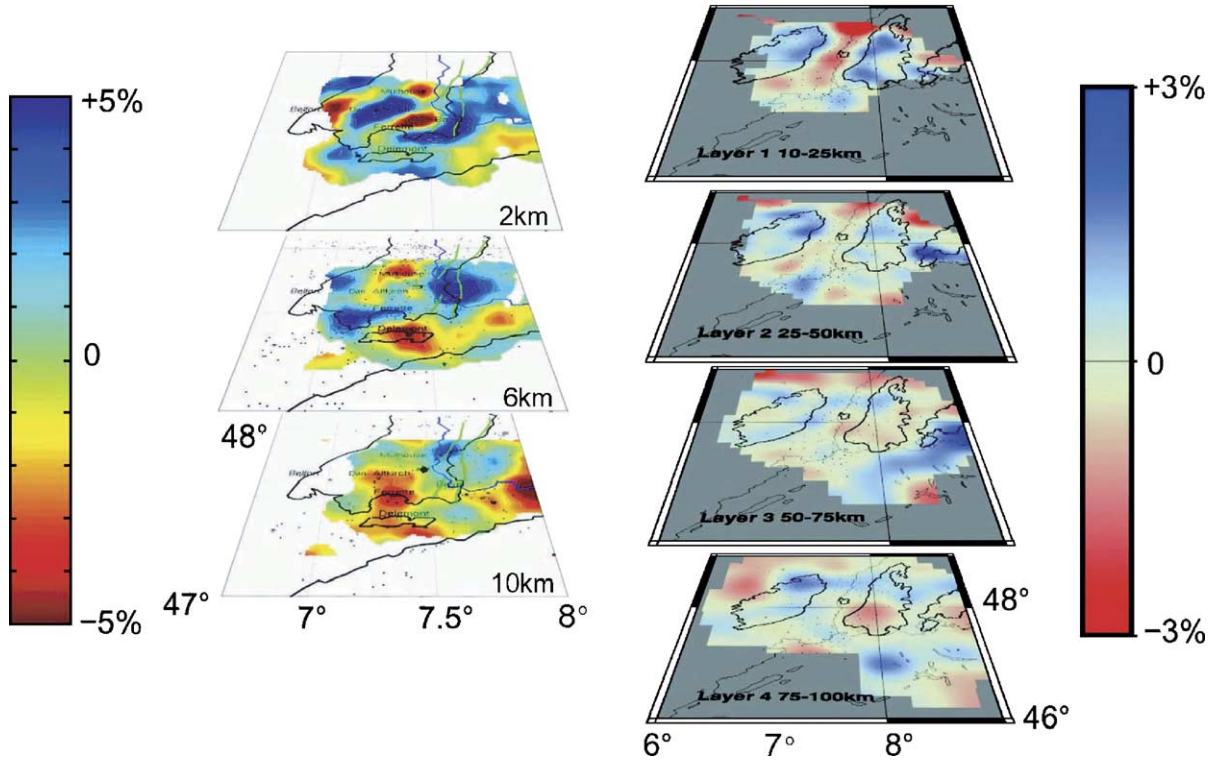

Fig. 24. Comparison of tomographic results. On the left panel, map view images of the P-wave velocity travel time residuals obtained from local earthquake tomography show the crustal velocity structure down to 10 km. The right hand panel presents map view images of teleseismic travel time tomography for the entire lithosphere. Note scale difference.

sphere. Accordingly, perturbation of the lithosphere–asthenosphere boundary would develop parallel to the rift axis. However, the absence of graben parallel mantle-lithospheric structures, speaks against the applicability of the simple-shear model to the URG.

The observed orientation of structures in the P-wave velocity model, together with the orientation of the P_n anisotropy (Judenherc et al., 1999), suggests that deformation of the mantle-lithosphere involved reactivation of pre-existing Variscan structures, rather than the development of a newly formed shear parallel to the rift axis. Therefore, the most plausible model for the development of the URG is a combination of simple shear and oblique rifting (Fig. 25).

The difference between the strike of structures observed in the crust and in the mantle-lithosphere implies that the ductile lower crust acted as a partial decoupling layer. Intense shear-deformation is thought to have erased the layering of the lower crust as defined by reflection-seismic data (Wenzel et al., 1991; Brun et al., 1992).

The two tomography studies, combined with the results of other geophysical and geological studies, describe the configuration of the entire lithosphere of the URG.

5.4. Structural modelling of tomography coupled with numerical modelling

A detailed model of upper crustal fault systems was developed for the southern part of the URG by combining the results of local earthquake tomography with data derived from reflection-seismic lines, focal mechanisms, hypocenter locations, and gravity data (Lopes Cardozo and Granet, 2003, 2005; Lopes Cardozo et al., 2005).

In the 3-D tomographic data body, the signature of fault zones was identified with the aid of reflection-seismic lines, defining the location of major faults at upper crustal levels. Subsequently, fault zones were traced on vertical slices through the tomographic velocity body, while their strike was derived from horizontal slices and from gravity data. Thus, fault zones could be traced from one vertical tomographic slice to the next, similar to the interpretation of a reflection-seismic survey (Fig. 26).

A total of six fault zones were defined. These are: the Western Boundary Fault, the Illfurth Fault, the Sierentz Fault, the Eastern Boundary Fault, the Black Forest Fault and the fault system that delineates the northern margin

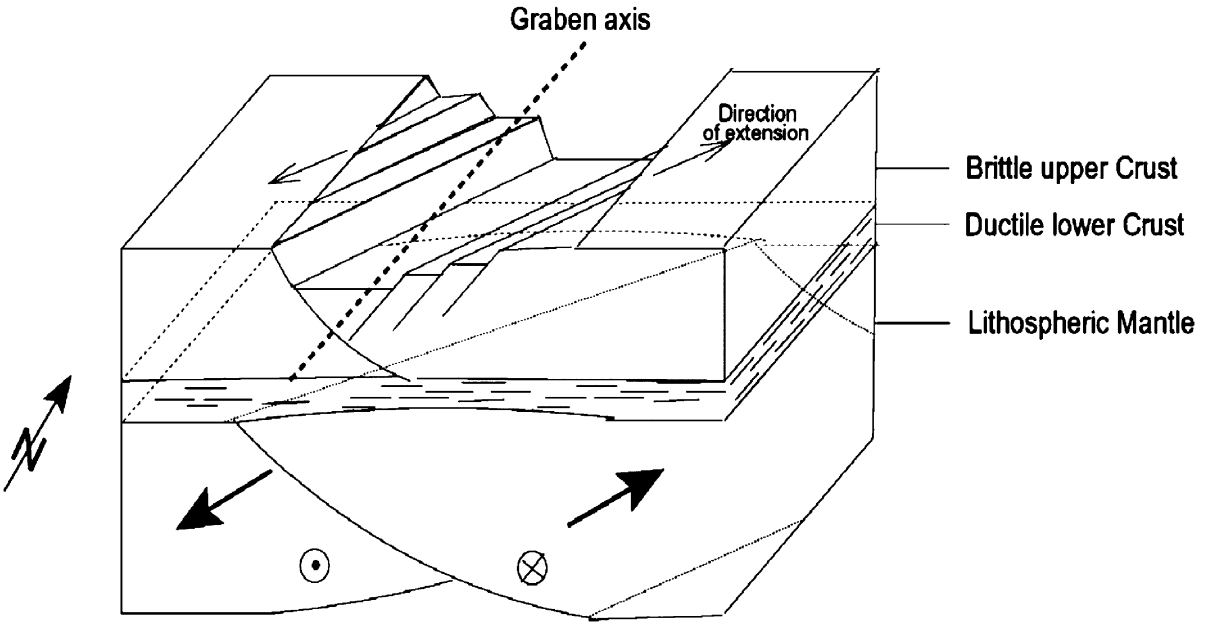

Fig. 25. Model for the formation of the URG: sinistral strike-slip motion along a mantle shear zone, oriented obliquely to the graben axis, causes oblique upper crustal extension. Pre-existing Variscan crustal structures are reactivated as sinistral transtensional faults.

of the Permo–Carboniferous trough system beneath the Jura Mountains (Fig. 27). At top-basement level, the location of most of the faults is controlled by reflection-seismic lines. Some of these crustal faults are considered to be active owing to the occurrence of nearby earthquakes. The direction and sense of movement along some of these faults is defined by focal mechanisms, which indicate that on-going deformation of the mapped area is controlled by NW–SE compression.

In the modelled region, the magnitude of stresses is unknown as in-situ stress measurements (Becker, 2000) are too close to the surface and as their results are too variable to be included in our model. Therefore, we simulated a compressional regime by applying oblique displacements on the boundaries of our model (Fig. 28). Applied displacement rates, partially constrained by GPS data, are in the order of 1 mm/yr. In our modelling experiment 1 m of displacement was applied, equivalent to 1000 years.

In an effort to evaluate the response of the southern URG fault system to the present-day stress regime, we imposed on the boundaries of our model the following three NW–SE directed displacement conditions (see Fig. 28). In the first case, all boundaries of our model were displaced by the same amount. In case 2, the amount of displacement was unevenly spread over the model boundaries. In case 3, the amount of displacement was distributed such that emphasis was put on sinistral activity along the eastern boundary fault zone of the graben.

Homogeneous displacement leads to concentration of deformation and unrealistic solutions, as shown in case 1 (Fig. 29). Applying heterogeneous displacement boundary conditions (case 2 and 3) affects all faults of the system, with displacements mainly accommodated along the Eastern Boundary Fault and the faults beneath the Jura Mountains (PT1–3) (Fig. 29). These faults also seem to localize extreme values of isotropic stress, deviatoric stress, and the Drucker–Prager criterion (numerical equivalent of Mohr–Coulomb failure criterion). This supports the concept that the eastern part of the graben system is more active than the western one.

When the Eastern Border Fault, the largest of the system, is given even more freedom to move (case 3), other faults of the system become also active. Therefore, future seismic hazard studies should not only focus on the largest known fault of the region, but include also smaller ones and unknown structures.

5.5. Results of GPS measuring campaigns and precision-levelling

In order to determine uplift/subsidence and horizontal displacement rates in the URG area, GPS measurements were carried out by a group of universities and governmental agencies of France, Switzerland and Germany (CNRS Géosciences Azur Nice, Bureau de Recherches Géologiques et Minières Orleans, Federal Office of Topography Switzerland,

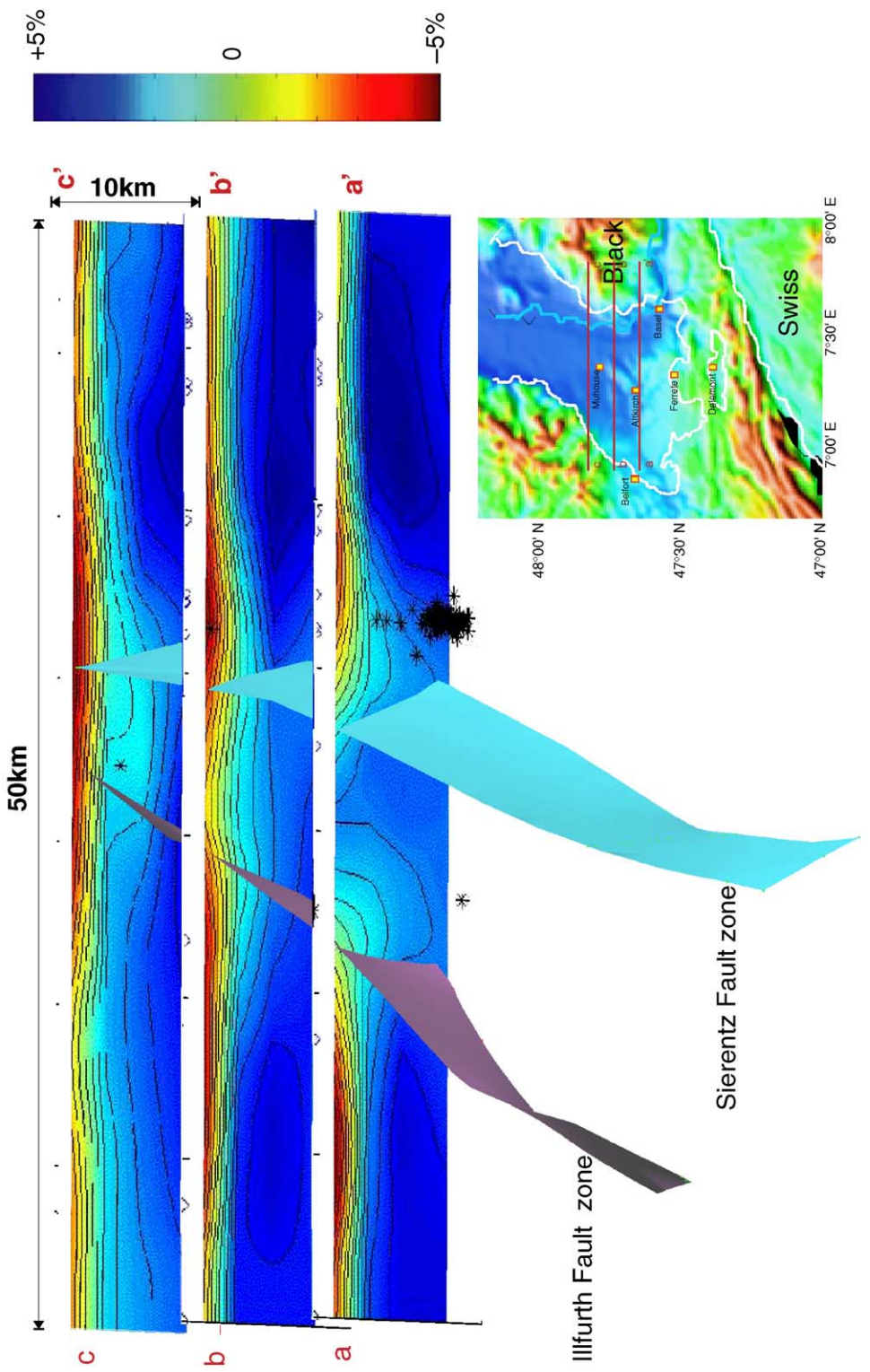

Fig. 26. E–W tomographic cross-sections of P-wave velocity travel time residuals through the southern part of Upper Rhine Graben, showing position of Illfurth and Sierentz faults that is constrained by reflection-seismic data on one of the cross-sections. Contour line interval is 1%. Black stars: earthquake hypocentres. For discussion, see text. The cross-sections have a length of 50 km, and a depth of 10 km. For location see topographic map. White lines denote the edge of the distribution of the Tertiary sediments in the Rhine Graben, Delemont Basin and Molasse Basin.

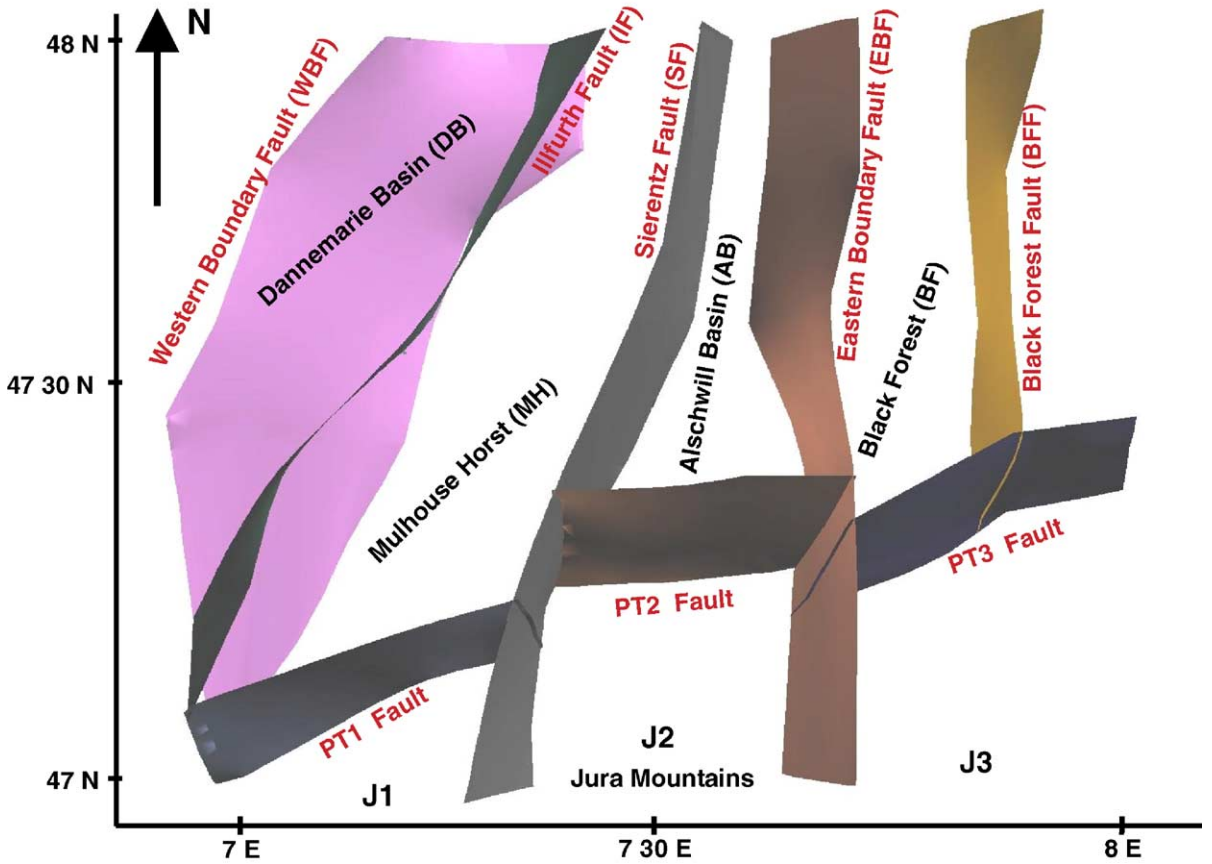

Fig. 27. Interpreted fault systems and major blocks in the southern-most parts of the Upper Rhine Graben. The E–W trending faults PT1 to PT3 form the northern margin of a Permo–Carboniferous trough system that underlies the Jura Mountains.

Geodesy and Geodynamics Laboratory of the Swiss Federal Institute of Technology Zürich, Geodetic Institute of the University of Karlsruhe and Ordnance Survey of Baden-Württemberg). Although many permanent GPS stations operate in the vicinity of the URG, the spatial resolution of the network had to be enhanced by temporarily occupied campaign stations (Fig. 30). These temporary stations provide not only a better spatial resolution, but in most cases have higher structural stability. So far, two measuring campaigns were carried out in 1999 and 2000, involving a total of 30 and 27 stations, respectively.

Furthermore, in 2002 two weeks of data from selected permanent stations was acquired and processed in order to monitor their displacement evolution. This survey included the stations STUT (Stuttgart), ZIMM (Zimmerwald), ETHZ (ETH Zürich) that, upon a statistical stability analysis, were considered as stable. A statistical displacement analysis was then carried out for the area covered by these stations.

In the analyses of displacements observed during the 1999 and 2000 measuring campaigns their horizontal and vertical components were separated. In this respect it must be realized that the horizontal accuracy of GPS positioning is by a factor of 2–3 better than the vertical accuracy. Unfortunately, as the time-span between the two measuring campaigns was too short, tectonically significant displacements could not be detected at most stations. Amongst the permanent stations, significant displacements were detected only at the station KARL where, at a 95% confidence level, displacement rates reach a value of 0.8 mm/yr, with a bearing of W–NW (Fig. 30).

Obviously, longer time-intervals are required between GPS measuring campaigns in order to determine more accurately on-going vertical and horizontal displacements and to compute detailed strain distribution maps for the study area. However, based on statistical analyses of the already available data, it is evident that displacement rates in the URG area must be well below 1 mm/yr. This is compatible with geological data and

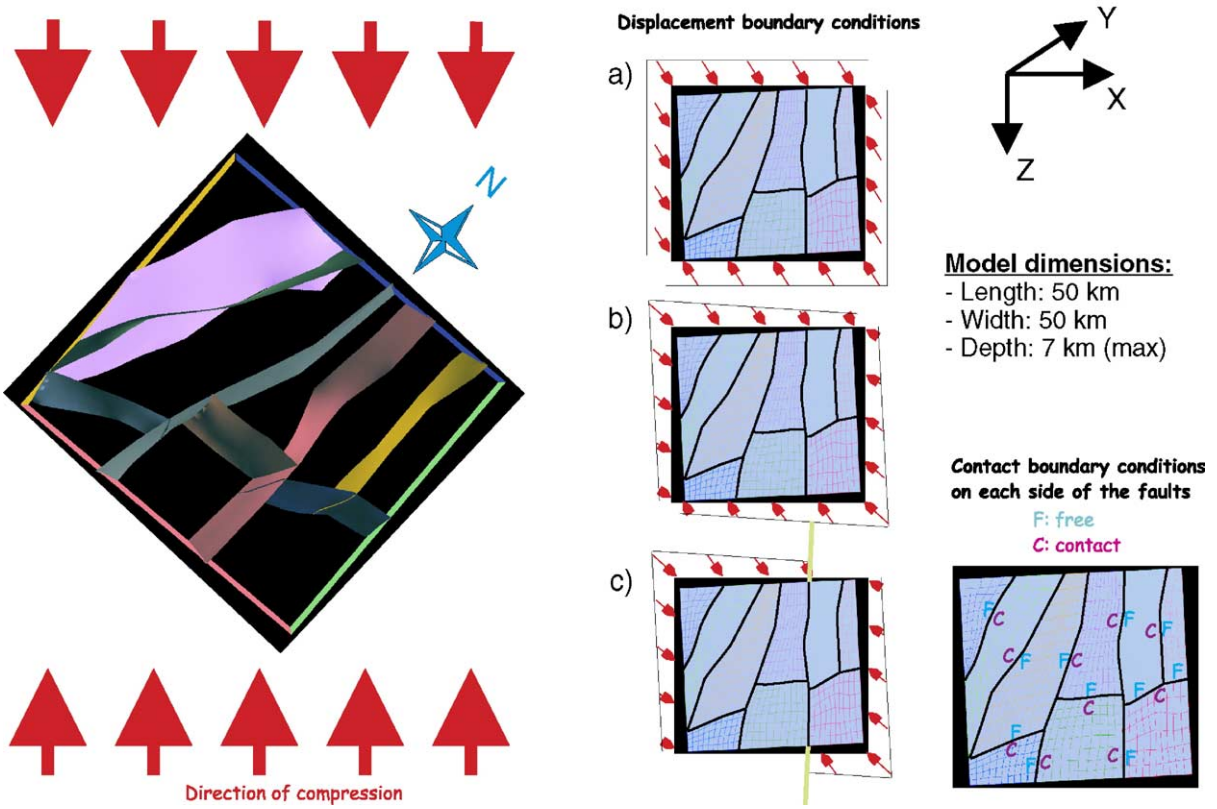

Fig. 28. Left panel: The fault-block model of Fig. 27 is subjected to NW–SE compression that is simulated by NW-ward displacement of its southern and eastern borders and SE-ward displacement of its northern and western borders. Center panel: (a) case 1: uniform displacement on all model borders; (b) case 2: uneven displacement of the model borders with maximum displacement at the northwestern and southeastern corners, and minimum displacement at the northeastern and southwestern corners; (c) case 3: in order to simulate strike-slip motions on the Eastern Boundary Fault of the Upper Rhine Graben, displacements are confined to the northern and western model borders W of this fault and to the southern and eastern model border E of this fault. Right panel: The Cartesian coordinates of the model and contact boundary conditions for each fault plane.

the results of Nocquet and Calais (2003) who, based on the analysis of 64 permanent stations spread all over Europe, determined horizontal displacement rates of no more than 0.6 mm/yr across the URG.

As the vertical accuracy of GPS positioning is significantly poorer than for horizontal positioning, we had to resort to high-precision-levelling data for the detection of uplift/subsidence rates. Such data sets are not only very accurate, but cover time spans of over 80 years. Recently, Demoulin (2004) has demonstrated that reconciling geodetic and geological rates of vertical crustal motions in intraplate regions requires a high frequency and a large number of measurement epochs in regional levelling, much greater than in classical comparisons of general surveys, inadequate to separate tectonic and near-surface components of ground motion. As pointed out by Demoulin, future investigations should concentrate on whether recording aseismic slip events in intraplate settings may give indications regarding the possible seismogenic character of a fault.

Precision-levelling data sets were acquired on the German side of the study area in the vicinity of Freiburg (Zippelt, 1988; Demoulin et al., 1995; Rosza et al., 2005). Altogether four 1st and 2nd order levelling lines were selected, which cross various faults along the eastern graben margin (Fig. 31). These levelling data revealed significant positive vertical displacements in the vicinity of Eichstetten (0.71 mm/yr), where the Lehen–Schönberg Fault shows seismic activity. Similarly, the Main Border Fault is active in the area of Freiburg and significant positive displacements were detected along the Weinstetten Fault in the vicinity of Bad Krozingen. Positive vertical displacement rates reach values of up to 0.45 mm/yr on the Main Border Fault and 0.35 mm/yr on the Weinstetten Fault. The detected vertical displacement rates are shown in Fig. 31 and are

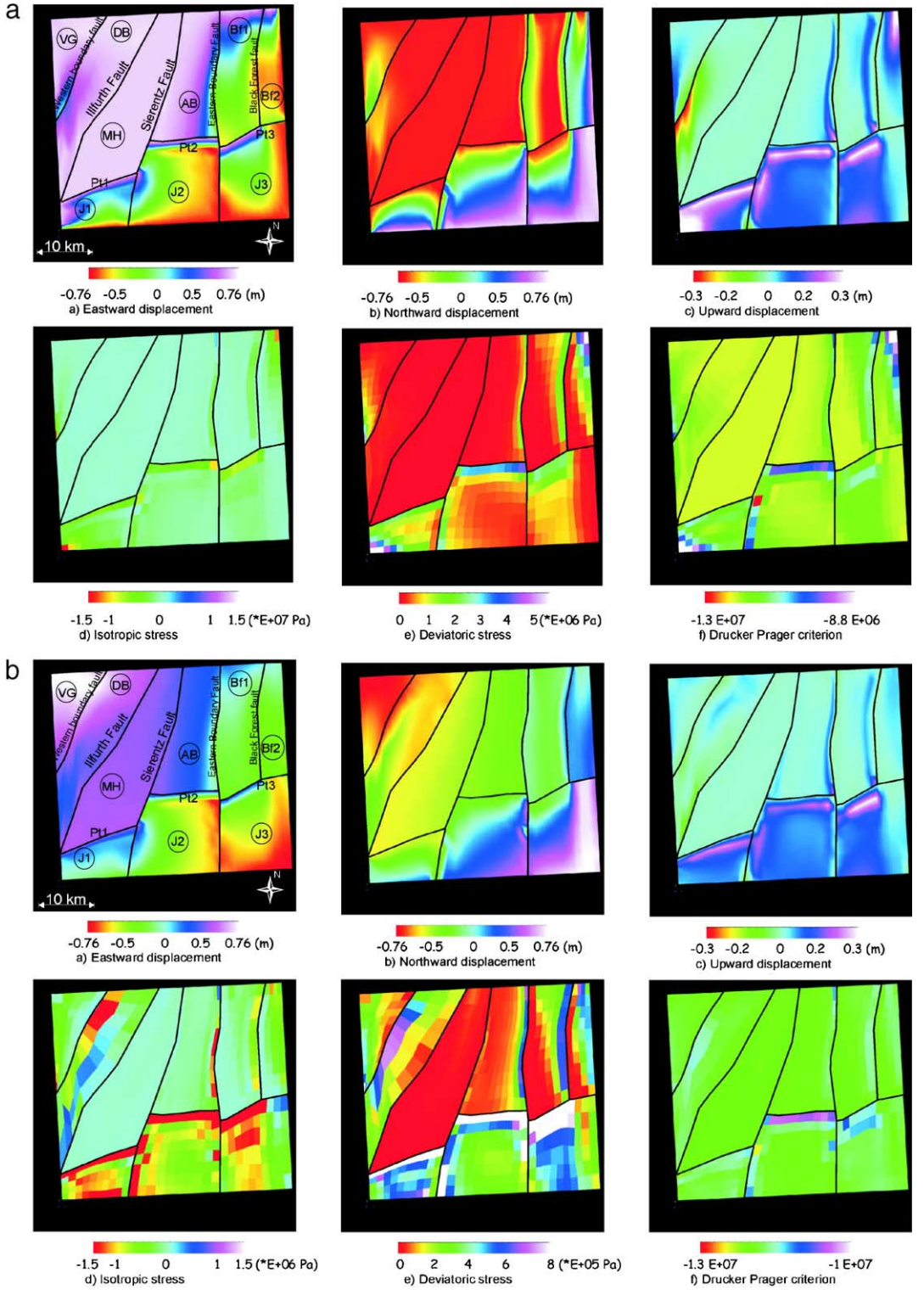
a
VG
DB
Bf1
Western boundary fault
Illfurth Fault
Sierentz Fault
Eastern Boundary Fault
Black Forest Fault
AB
Bf2
MH
Pt2
Pt3
Pt1
J2
J3
J1
N
10 km
-0.76 -0.5 0 0.5 0.76 (m)
a) Eastward displacement
-0.76 -0.5 0 0.5 0.76 (m)
b) Northward displacement
-0.3 -0.2 0 0.2 0.3 (m)
c) Upward displacement
-1.5 -1 0 1 1.5 (*E+07 Pa)
d) Isotropic stress
0 1 2 3 4 5(*E+06 Pa)
e) Deviatoric stress
-1.3 E+07 -8.8 E+06
f) Drucker Prager criterion
b
VG
DB
Bf1
Western boundary fault
Illfurth Fault
Sierentz Fault
Eastern Boundary Fault
Black Forest Fault
AB
Bf2
MH
Pt2
Pt3
Pt1
J2
J3
J1
N
10 km
-0.76 -0.5 0 0.5 0.76 (m)
a) Eastward displacement
-0.76 -0.5 0 0.5 0.76 (m)
b) Northward displacement
-0.3 -0.2 0 0.2 0.3 (m)
c) Upward displacement
-1.5 -1 0 1 1.5 (*E+06 Pa)
d) Isotropic stress
0 2 4 6 8 (*E+05 Pa)
e) Deviatoric stress
-1.3 E+07 -1 E+07
f) Drucker Prager criterion

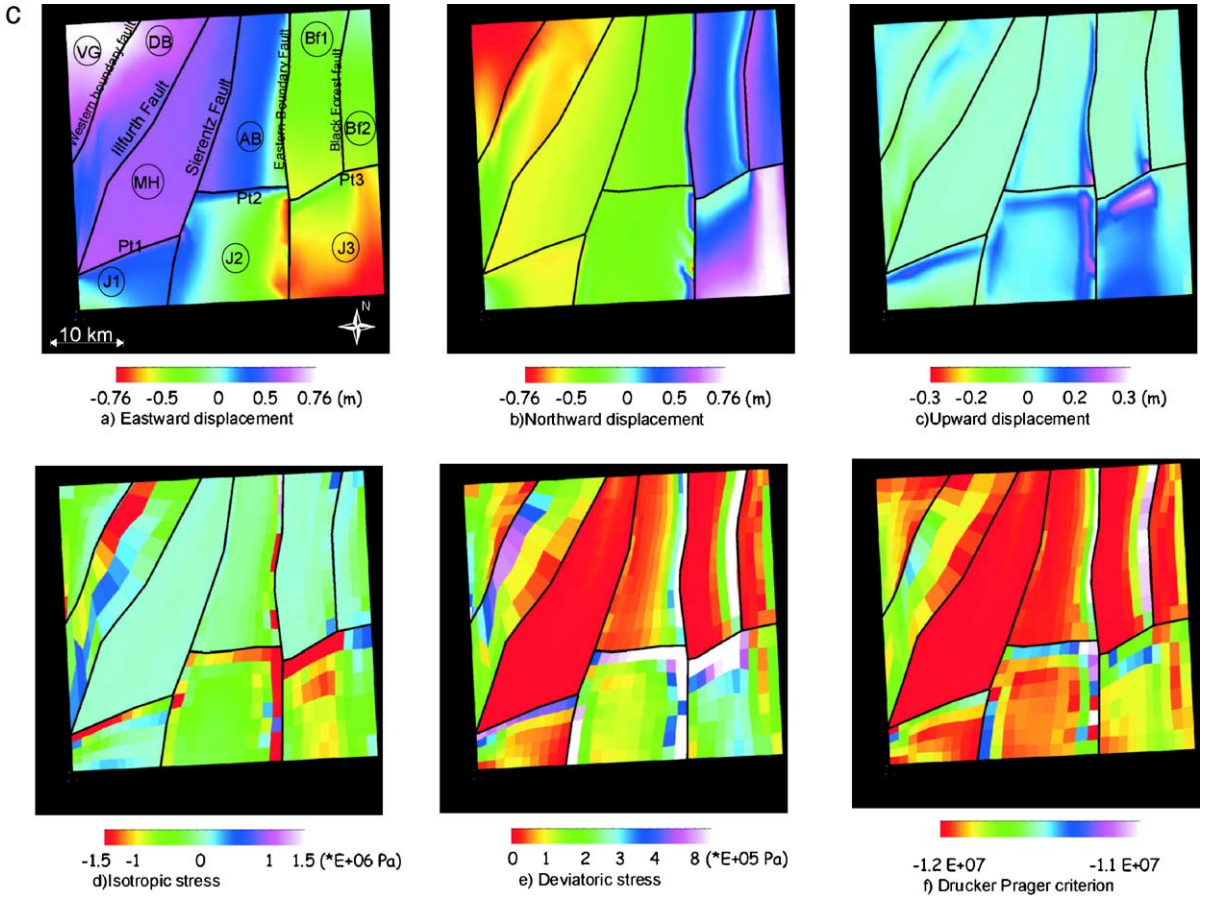

Fig. 29. Results of (a) case 1, (b) case 2, (c) case 3. Black lines indicate faults zone. For each case E–W motions (subpanels a), N–S motions (subpanels b), vertical motions (subpanels c), isotropic stress (subpanels d), 2nd invariant of the deviatoric stress (subpanels e), and the Drucker–Prager criterion (subpanels f) are shown in colour. Under the applied boundary conditions, the Eastern Boundary Fault accommodates most of the deformation of the model. However, all other faults in the system are also activated. Strike-slip motion along the border faults and their reverse component can be compared to focal mechanism. Maximum compression is concentrated on the Eastern Boundary Fault Zone and on faults beneath the Jura Mountains. Negative values for the Drucker–Prager criterion show that no new faults are formed in the model.

compatible with seismotectonic investigations carried out by Behrmann et al. (2003).

In order to develop a reliable strain distribution map for the study area, GPS campaign measurements need to be continued. However, during the last few years, many permanent GPS stations were newly installed in the URG and its vicinity. Therefore, the data logged by these stations will be reprocessed using the same approach in order to derive consistent results. Using these data sets, a good regional overview of displacement rates in the URG should be obtained, particularly when enhanced by long-term GPS campaigns.

5.6. Seismotectonics of the Freiburg area

The URG came into evidence during the late Eocene and remained tectonically active to the present. Subsidence of its southern parts was interrupted during the Burdigalian in conjunction with doming of the Vosges–Black Forest Arch, but resumed during the late Pliocene and continued during the Quaternary (Schumacher, 2002; Dèzes et al., 2004). The relatively well-preserved topography of the shoulders of the URG (Fig. 18a) suggests a Plio–Pleistocene reactivation of its border faults. This possibility was evaluated along the SE margin of the URG in the vicinity of Freiburg (SW Germany), where despite continuous though diffuse seismic activity, evidence for near-surface deformation had so far not yet been documented.

In an effort to identify possible indications for Pleistocene deformation, a multi-disciplinary study was initiated, focusing on regional and local geomorphologic and geological evidence. Satellite images revealed that fault patterns defined at Oligocene

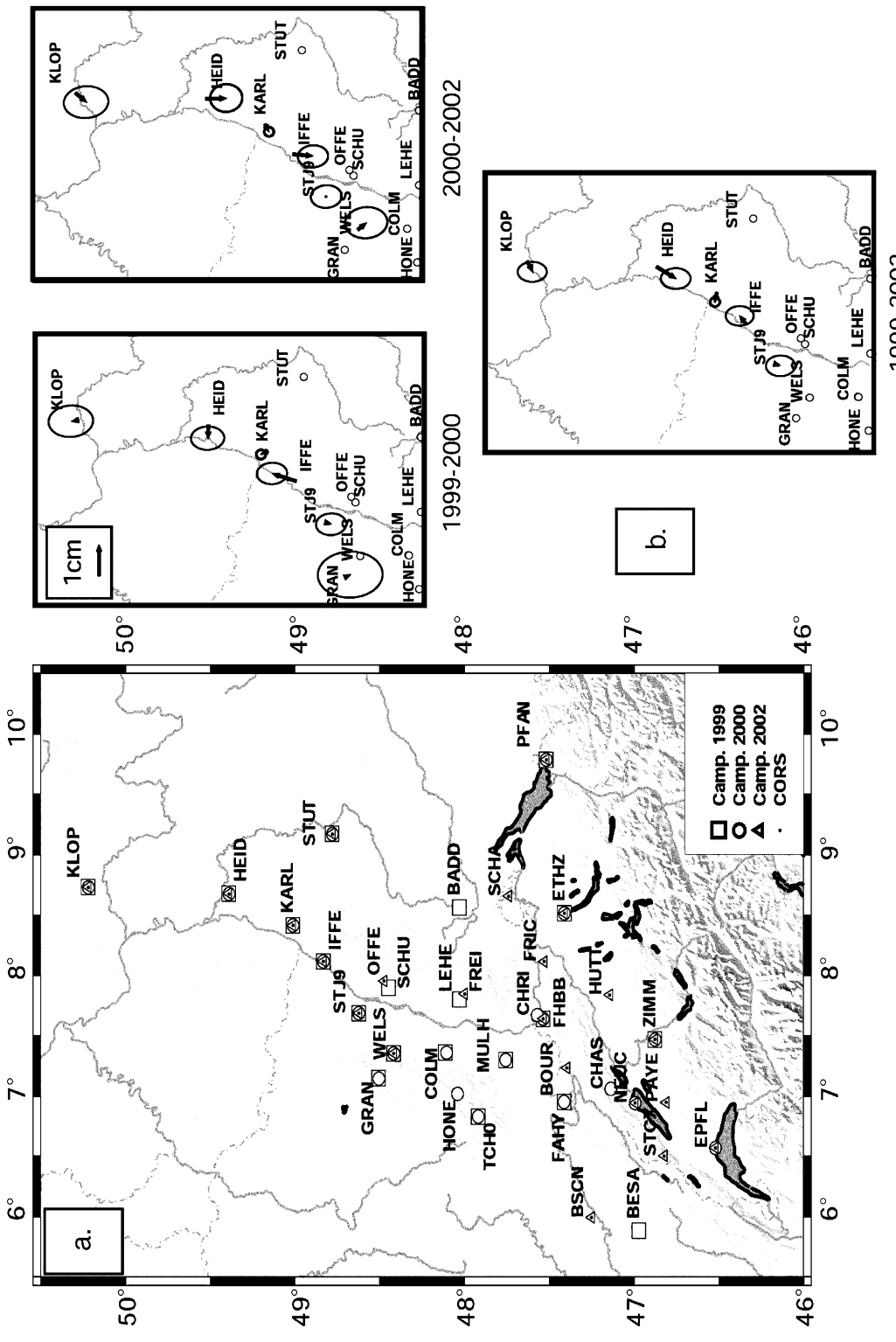

Fig. 30. Left panel (a): GPS network in the Upper Rhine Graben area. Squares: campaign 1999; circles: campaign 2000; triangles: campaign 2002. Right panels (b): differential horizontal displacements during various time spans relative to Karlsruhe (confidence of the error ellipses 95%).

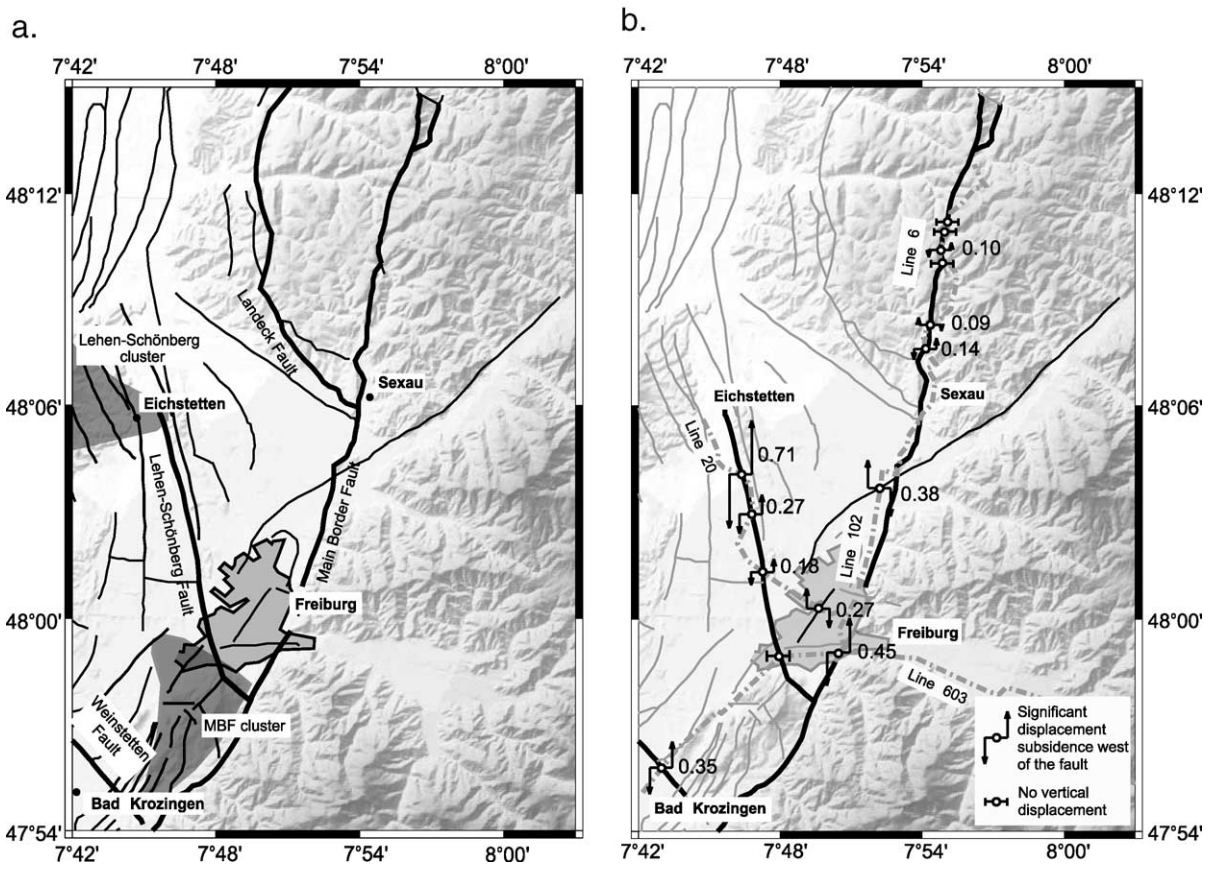

Fig. 31. (a) Investigated precision levelling lines and fault pattern around Freiburg. (b) Vertical displacement rates along faults (mm/yr).

levels have a clear topographic expression as continuous scarps, a few tens of kilometres long and 20–30 to 300–500 m high (Fig. 32).

5.6.1. Regional approach

Based on geological maps, imagery and field observations, terraces and alluvial fans were mapped as potential markers for young deformation. Based on terraces geometries, supported by borehole control on the thickness and composition of alluvial deposits, the evolution of the Quaternary drainage system could be reconstructed (Fig. 33). At the beginning of Quaternary (Fig. 33a), the paleo-Elz and paleo-Dreisam rivers flow towards the NW and SW, respectively. During the Riss glacial period (Fig. 33b), sediments shed by the Black Forest formed a continuous flood plain, the westward extent of which is unknown owing to its subsequent erosion. During the Würm glacial period (Fig. 33c), the river Rhine shifted to the east of the Kaiserstuhl volcano, whereas further south it incised eastward into the Riss flood plain up to the trace of the Rhine River Fault. Subsequently, the Rhine shifted back to the west of the Kaiserstuhl volcano, whereas the Elz and Dreisam rivers continued to flow towards the NW (Fig. 33d). This scenario raises the question whether the scarps along the Rhine River Fault are tectonic or erosional in origin.

5.6.2. Local approach

The southern branch of the Rhine River Fault was studied in detail, using borehole logs, field observations, imagery and subsurface geophysical data. This part of the Rhine River Fault was chosen owing to the incision gradient of valleys narrowing toward the fault on its footwall block and the presence of newly formed fans on its hanging wall block (Fig. 32, Staufen fan). Pleistocene tectonic reactivation of the Rhine River Fault is suggested by the occurrence of local depocentres on its hanging wall, indicative for a Pleistocene minimum vertical offset of about 30 m (Fig. 34). In view of the linearity and continuity of the Rhine River scarp, its association with hanging valleys, and its possible coincidence with a reactivated fault, three electric tomography profiles were recorded across it

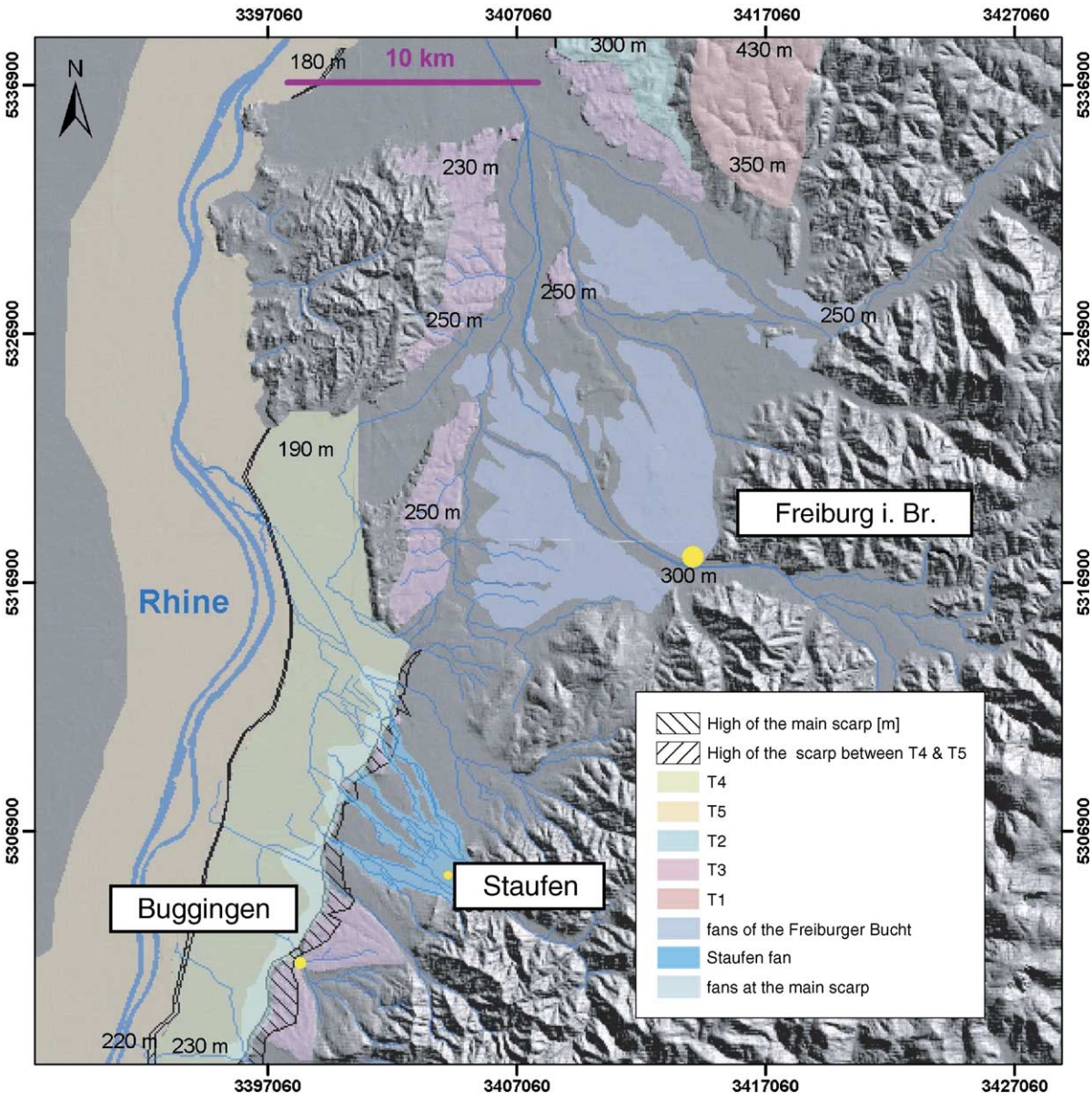

Fig. 32. Digital elevation model of the Freiburg area, showing the alluvial terrace and fans with approximate elevations. Except for T1, terraces elevation tends to increase southward, as do scarp amplitudes.

in the Tunsel area (Fig. 35). On two of these profiles, a faulted vertical offset of Weichselian deposits by up to 15 m could be documented.

5.6.3. Regional morphotectonic study

A systematic morphotectonic survey of the southern parts of the URG identified several escarpments of potentially tectonic origin along which recent seismic activity may be recorded, such as the Berwiller scarp in the Dannemarie Basin (see Fig. 18a for location). Across this escarpment geophysical data were acquired and shallow boreholes drilled in order to obtain information on its subsurface configuration and specifically on the nature of its origin (Gourry et al., 2001; Brüstle et al., 2003). Fig. 36 illustrates the adopted multi-disciplinary approach. First, an initial regional site reconnaissance is performed on the DEM (Fig. 36a). Then, subsurface properties of the ground are imaged by electrical tomography vertical panels (electrical resistivity results shown in Fig. 36c), seismic reflection panels (Fig. 36d) and by a planview map of electro-magnetic survey (Fig. 36e). Finally, a profile of six shallow, non-

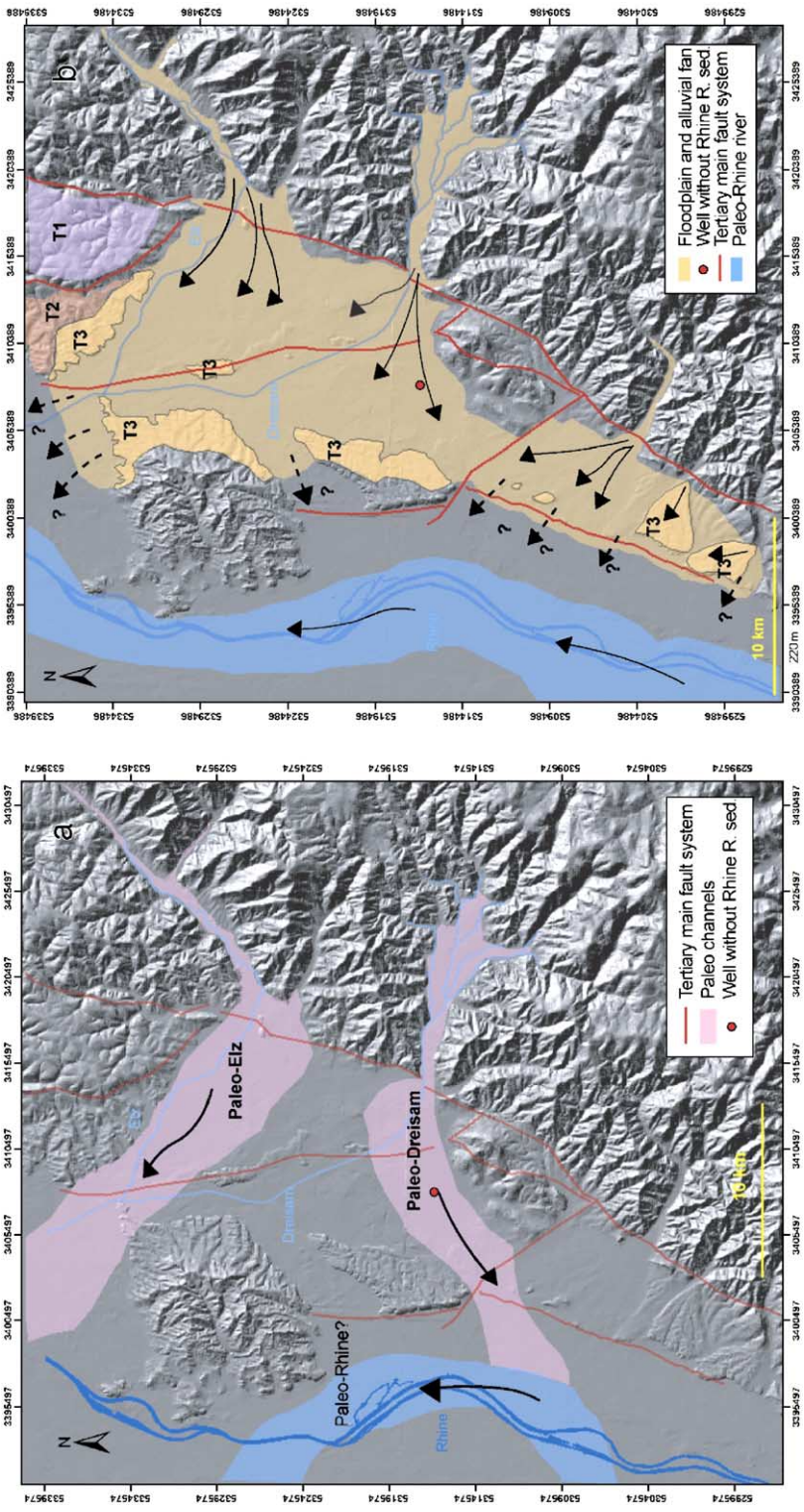

Fig. 33. Evolution of the drainage system during the Quaternary. (a) At the beginning of Quaternary, the Elz and Dreisam flow respectively toward the NW and the SW, following the channels identified on Fig. 3. (b) During Riss glacial age, sediments from the Black Forest form a continuous flood plain in the graben. Extension of this flood plain is not known because of subsequent erosion. (c) During Würm glacial age, the Rhine river shifts eastward, east of the Kaiserstuhl volcano (NW corner of the area). In the south, incision from the Rhine river reaches the trace of the Rhine river fault. (d) Today, the Rhine river has moved back west of the Kaiserstuhl, while the Elz and Dreisam are still flowing toward the NW.

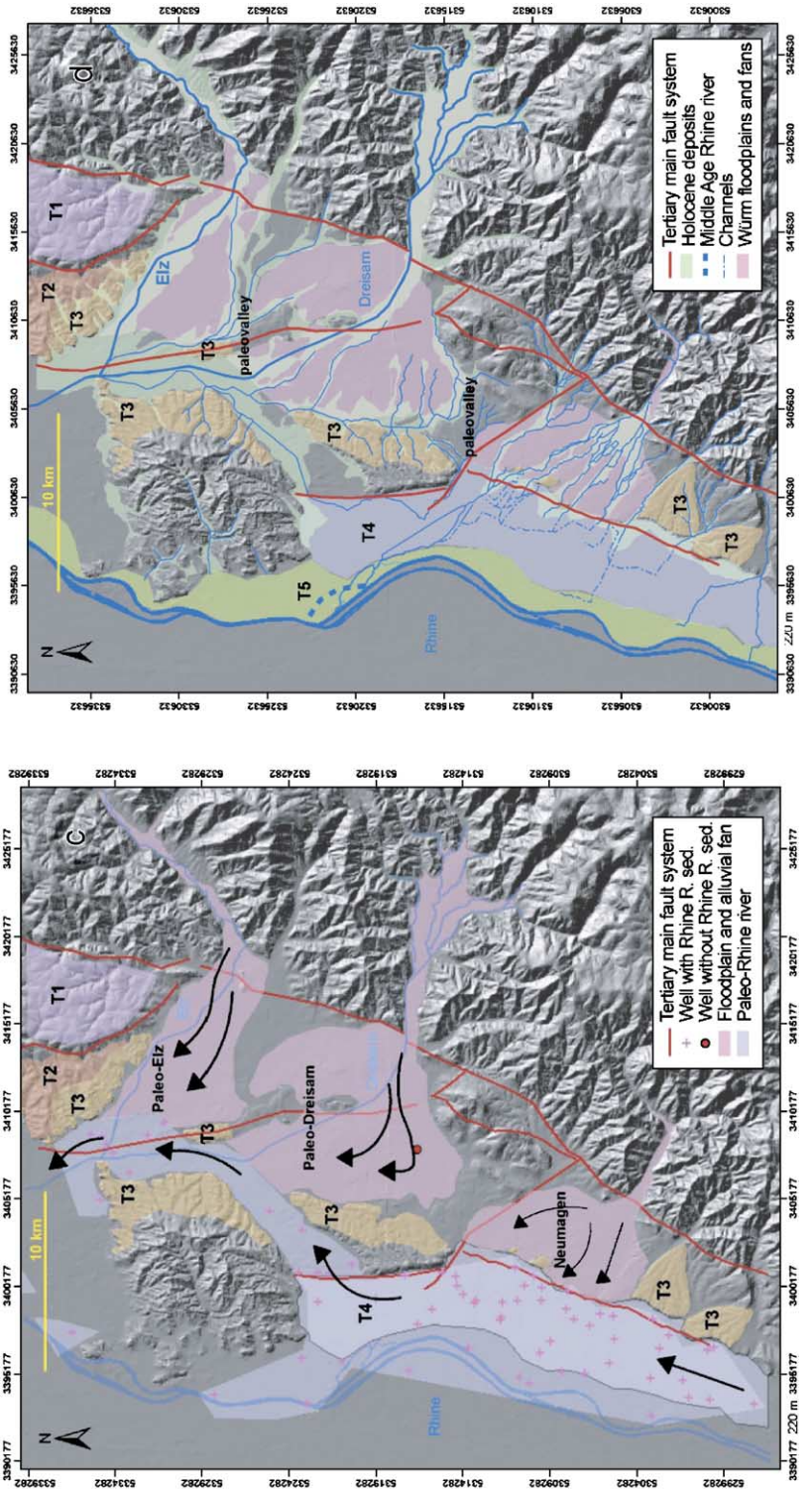

Fig. 33 (*continued*).

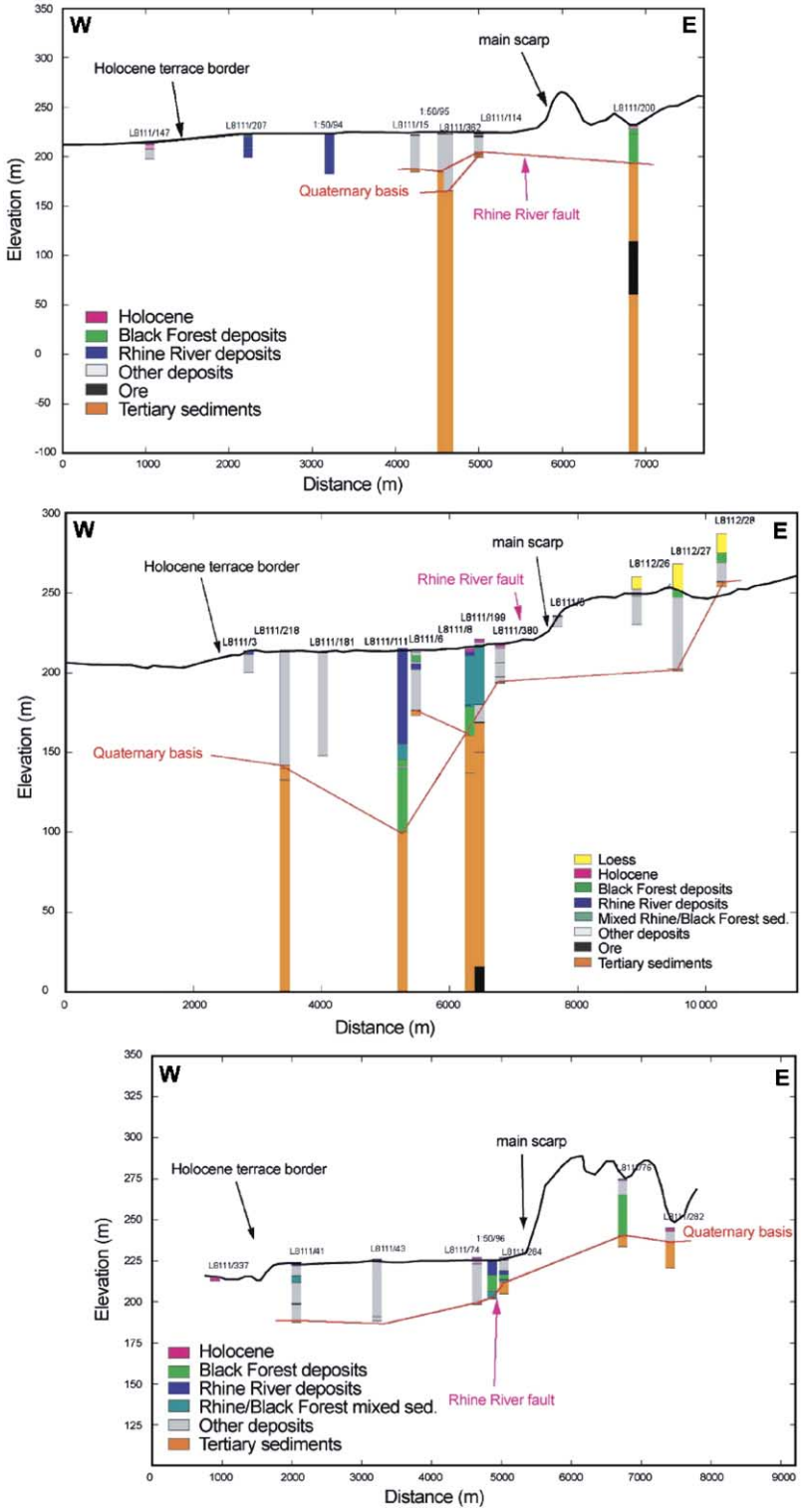

Fig. 34. Cross sections across the Rhine River escarpment near Tunsel, based on borehole logs (modified after Brüstle, 2002). Note elevation changes of the base of Quaternary deposits in the vicinity of the Rhine River Fault, reaching some 30 m. For location see Fig. 18a: the profiles are located near the star Tunsel.

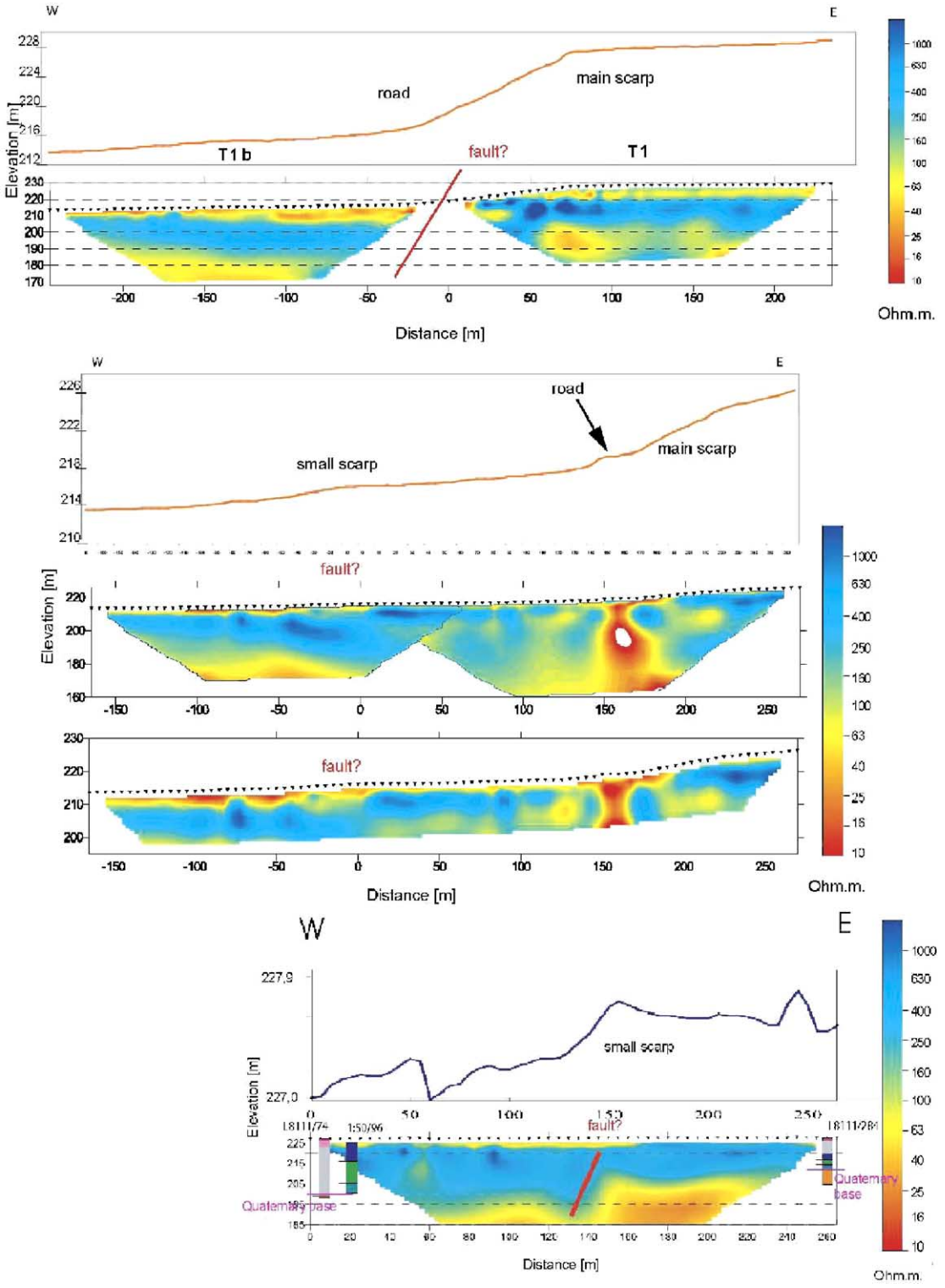

Fig. 35. Electric tomography profiles across the Rhine River escarpment near Tunsel (modified after Brüstle, 2002). Recent offsets are suspected only on the upper and middle profiles, whilst on the bottom profile the base of the Quaternary is offset by more than 15 m. For location see Fig. 18a: the profiles are located near the star Tunsel.

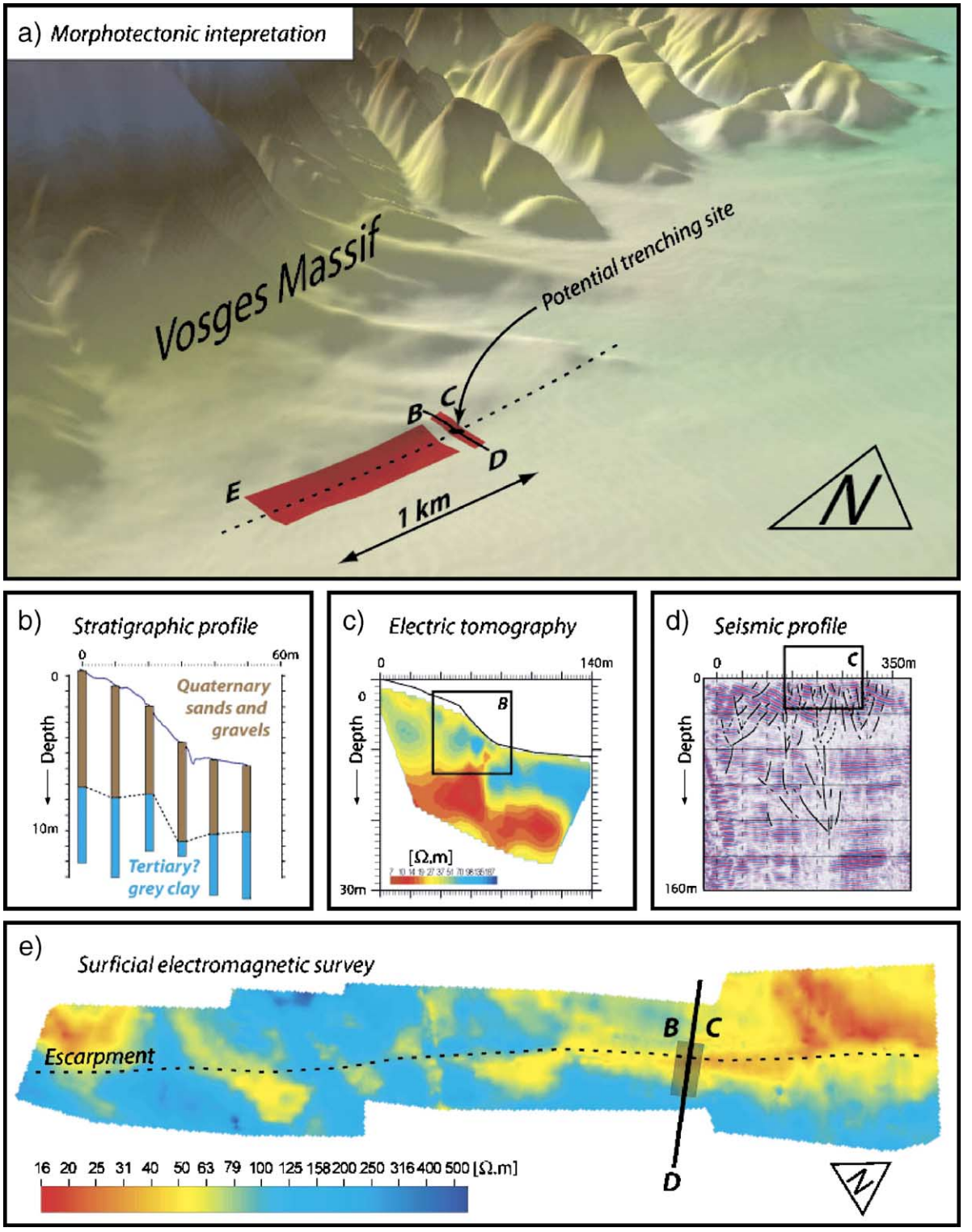

Fig. 36. Multidisciplinary analysis of a suspected tectonically induced scarp in the Berrwiller area. For location see Fig. 18a: the profiles are located near the star Berwiller. (a) Digital elevation model of the study area, showing locations of geophysical data acquisition and location of potential trenching site. Dashed line indicates the location of the studied escarpment. (b) Stratigraphic profile of six shallow cores. (c) Electrical resistivity. (d) Seismic reflection panels. (e) Planview map of electro-magnetic survey.

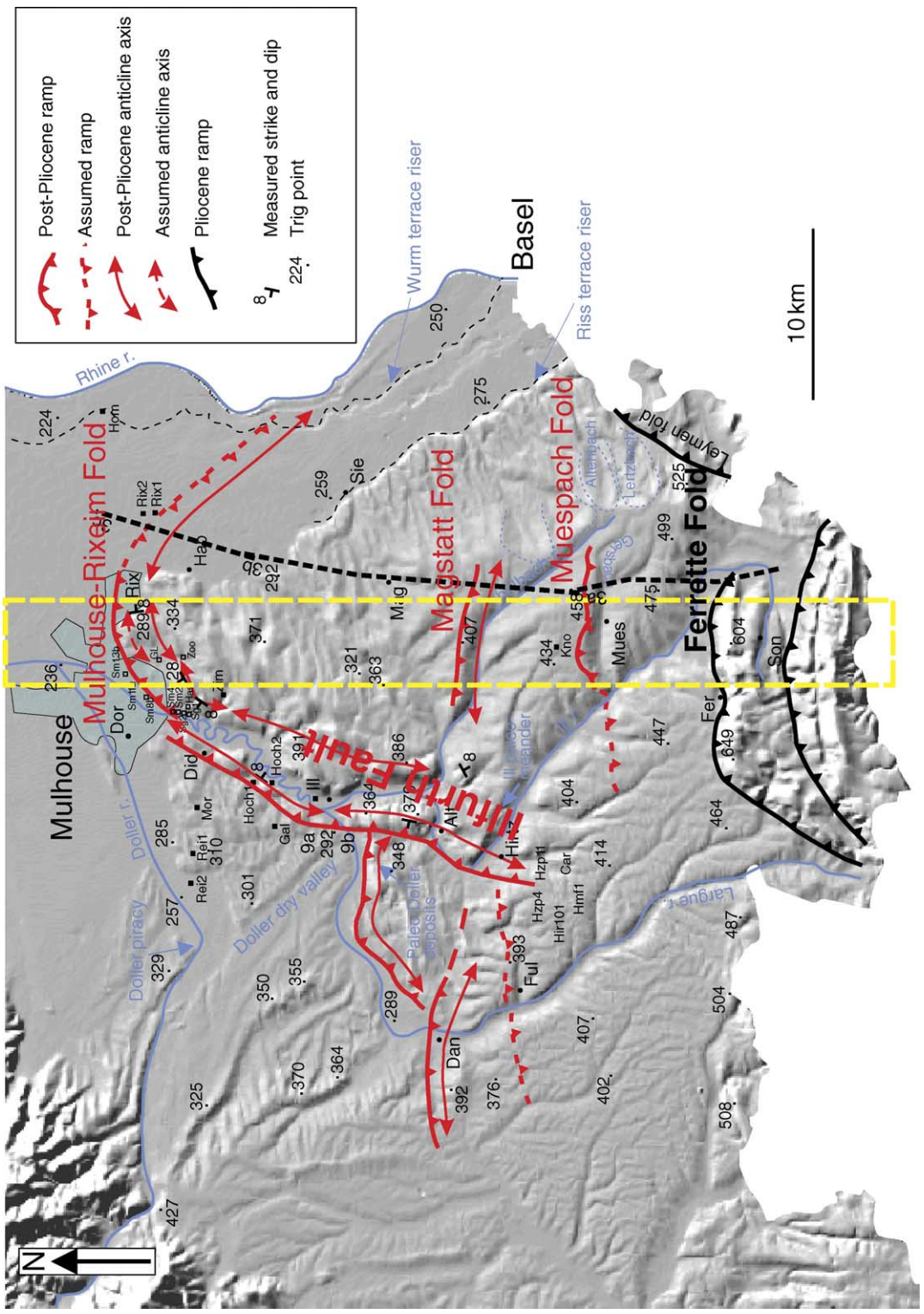

Fig. 37. Digital Elevation Model of Mulhouse Horst domain (vertical exaggeration ×10, source: IGN topomap) showing morphostructural interpretation (modified after Nivière and Winter, 2000). Dashed line yellow box: trace of cross-section given in Fig. 39.

destructive cores (Fig. 36b) was sunk in the location where the fault-like morphology seemed to exhibit the largest subsurface displacement. Though initially designed for palaeo-seismological trenching, this suite of investigation demonstrated the presence of a perched water table, rendering trenching technically difficult, expensive and hazardous. Shallow coring with a percussion coring device (hollow core barrel, 1 m long, 6 cm diameter) proved a viable exploration tool because it is not so sensitive to water table conditions and though laterally discontinuous, it on the other hand allows a much deeper view of subsurface stratigraphy (down to

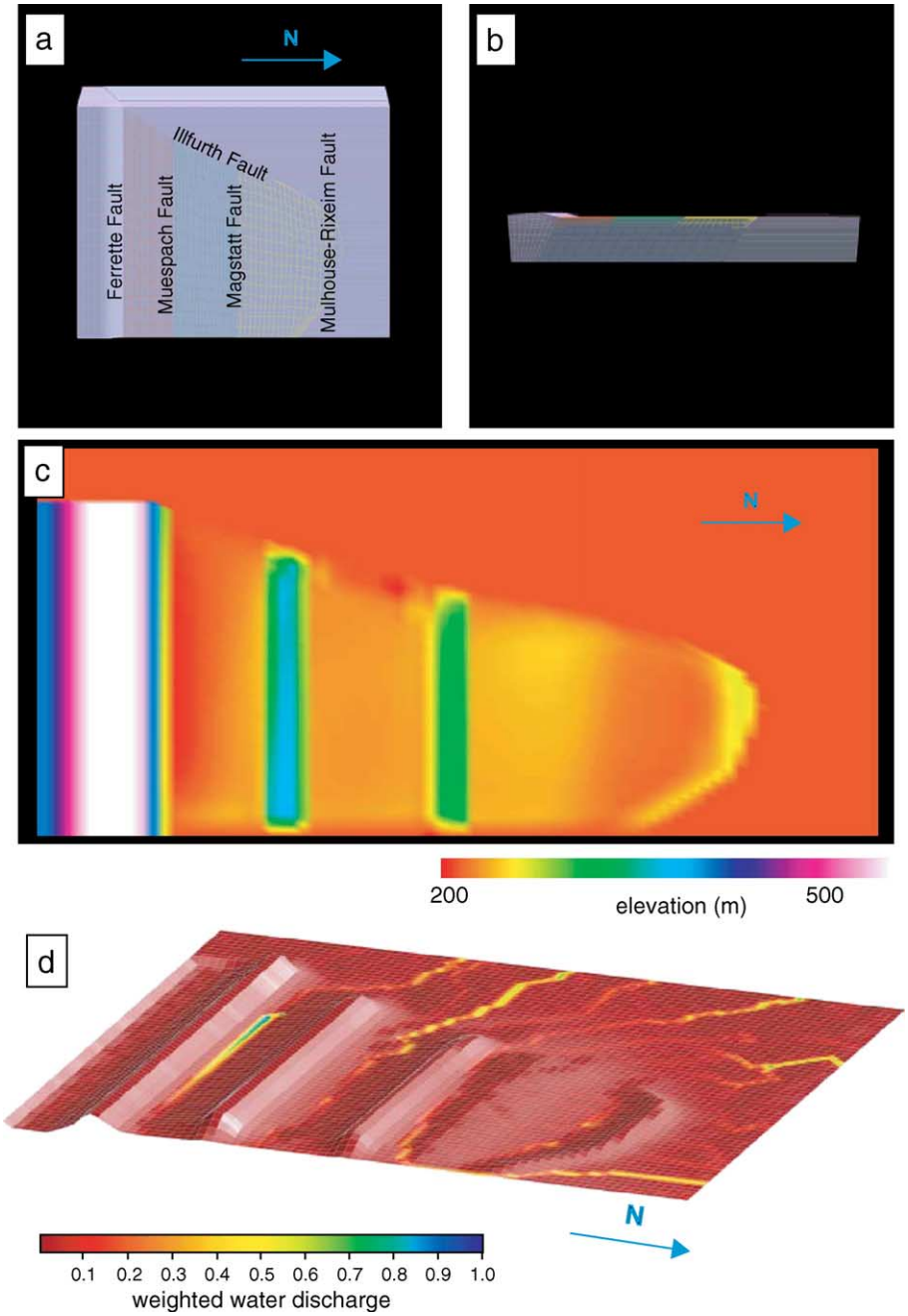

Fig. 38. (a) Top view and (b) lateral view of the mesh used for the finite element modelling of the tectonic deformation of the Mulhouse Horst domain. (c) Topographic view of the domain after 500 m of compression. (d) Hydrographic network computed from the topography given in (c).

11 m below the surface). Based on such complementary surveys, trenching sites may be selected where suspected fault activity could be validated and dated.

Our results point towards a Pleistocene reactivation of fault systems in the south-eastern parts of the URG. In order to validate these findings, trenching will have to be performed to determine the age of deformed deposits and to obtain information on the strain scenario. Furthermore, the study area will be extended toward the north to cover a larger portion of the graben.

5.7. Coupling of geomorphologic and numerical modelling

The physically based landscape evolution model APERO (Progressive Analysis of EROsion) was developed to model the interaction between tectonics and erosion at length scales of several tens of kilometres and at time scales ranging from several thousands to millions of years (Carretier et al., 1998; Carretier, 2000). This model accounts for multi-directional water flow, sediment production by bedrock-to-soil conversion, alluvial transport in rivers, bedrock incision by rivers, non-linear diffusive transport on hill slopes, simplified flexural isostasy, and 3-D kinematics of tectonic surface displacement.

APERO, combined with a code for geomechanical deformation of the crust (Cornu and Bertrand, 2005a,b), was applied to address the question of Plio–Pleistocene northward propagation of the Jura fold-and-thrust belt into the domain of the Mulhouse Horst and to assess related effects on the geomorphologic evolution of this area, using available geophysical, geological and geomorphologic data. This domain comprises from south to north the Ferrette, Muespach, Magstatt and Rixheim ramp-structures which are rooted in Late Triassic evaporites, acting as a detachment layer (Fig. 37).

The modelling presented here addresses the tectonic evolution of the Mulhouse Horst, focusing on fault reactivation and its relation to the Triassic detachment layer, and specifically on mechanisms controlling northward tilting of the area.

The tectonic model tested essentially north-directed compression and successive in-sequence activation of three faults within the deformed domain. It should be noted that the model cannot reproduce the creation of faults, but allows for a good description of frictional contacts. Therefore, each fault has to be pre-defined in the model.

Geomorphologic modelling addressed the evolution of the landscape in response to tectonic movements that were predicted by mechanical modelling, and highlights the capture of the hydrographic network. Coupling between erosion and tectonic movements was examined through simple erosion power laws depending on local gradients and water discharges.

Modelling reproduced the main topographic characteristics, namely an overall 1° north-dipping slope that locally flattens behind ramps where sediments accumulated (Figs. 38 and 39). Moreover, the thrusting history could be reproduced and demonstrated that the Illfurth Fault played an active role in the development of the dividing line between the uplifted and incised Mulhouse Horst and the westward adjacent Dannemarie Basin that is subjected to less intense erosion. On the other hand, back tilting behind the Mulhouse–Ricxheim thrust could not be reproduced. This modelling aspect, as well as geophysical data (Lopes Cardozo and Granet, 2003), suggests that deformation of the Mulhouse Horst is not restricted to thin-skinned tectonics but involved also a thick-skinned component.

6. Natural laboratory: Lower Rhine Graben

6.1. Introduction

The Lower Rhine Graben (LRG), which forms the northwestern segment of the European Cenozoic Rift System, extends from the margins of the Rhenish Massif to the Dutch North Sea coast (Fig. 40). Its main elements are the Erft half graben in the German Lower Rhine Embayment and the Roer Valley Rift System (RVRS) of The Netherlands (Fig. 41).

The late Oligocene and younger RVRS is superimposed on the West Netherlands basin that underwent a complex evolution, involving several Mesozoic and Paleogene extensional and inversion phases (Zijerveld et al., 1992; Geluk et al., 1994; Michon et al., 2003; Van Balen et al., 2005). During these Late Palaeozoic faults were repeatedly reactivated (Ziegler, 1990, 1994; Houtgast et al., 2002; Ziegler et al., 2004; Van Balen et al., 2005).

As shown in Fig. 41a, the RVRS structurally consists from SW to NE of the Campine Block, the Roer Valley Graben (RVG) and the Peel Block (Houtgast and Van Balen, 2000). Subsidence of the RVG was controlled by multi-stage evolution of the main bounding fault zones, including the Peel Boundary fault zone (PBFZ), the Feldbiss Fault Zone (FFZ), the Veldhoven Fault and the Rijen Fault. Remarkably, the subsidence of the basin is almost balanced by the offsets along these fault zones (Houtgast and Van Balen, 2000; Michon et

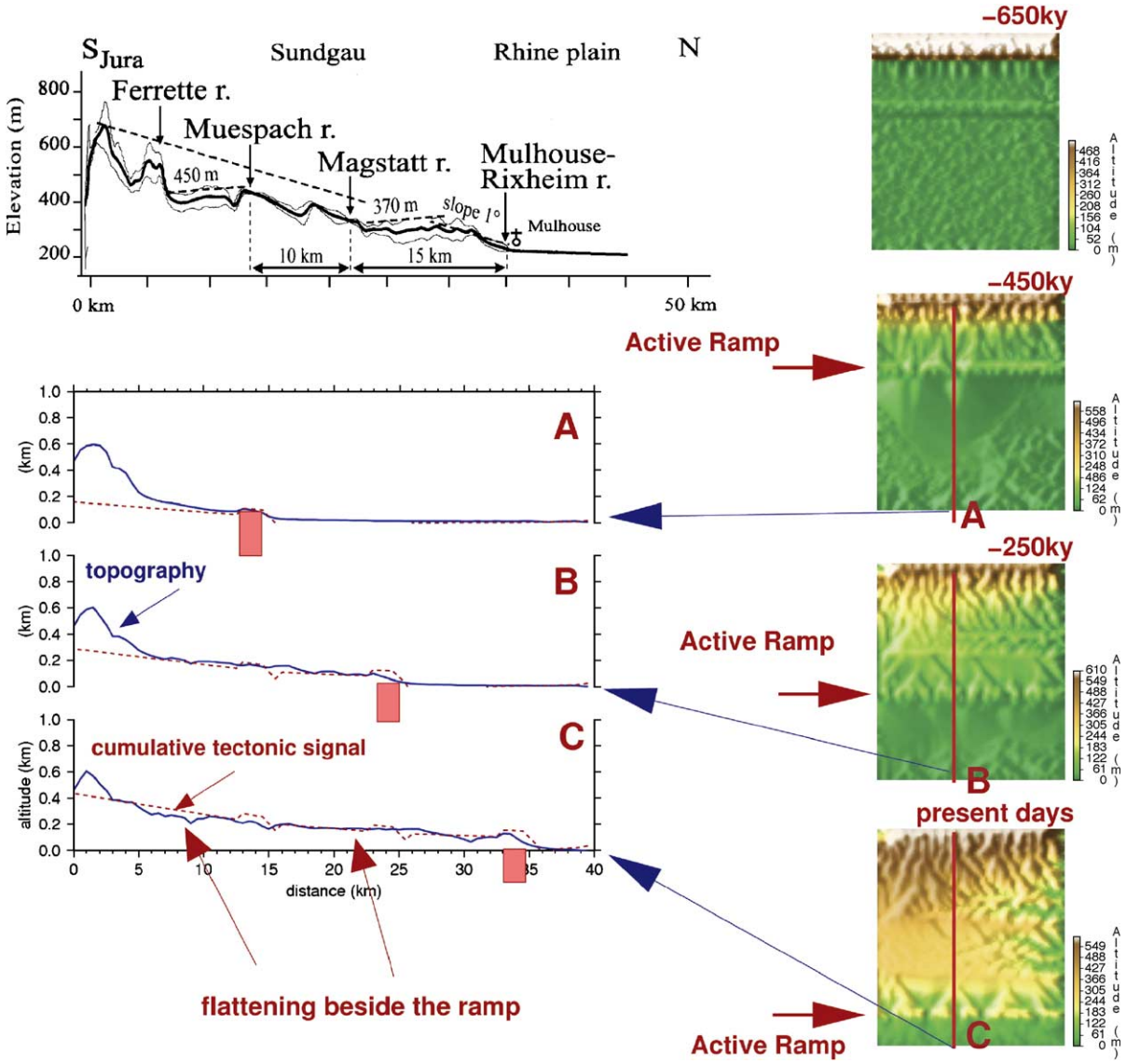

Fig. 39. Model for topographic evolution of Mulhouse Horst domain, involving 3 stages of in-sequence ramp-faulting and tilting. For location see Fig. 37. Erosion model: bedrock incision and alluvial transport during 650 kyr; initial sediment thickness of 10 m (gravels). Tectonics and topography development: the stages A, B and C show northward progression of ramping and tilting with the red bricks marking the location of active faults. The initial topography was a flat surface perturbated by a Gaussian signal (sigma = 1 m), whereas the Ferrette fold had a box-like relief of 600 m. For this test, climatic boundary conditions were assumed to be constant with 50 cm/yr of precipitation.

al., 2003). The Oligocene and younger syn-rift sediments attain a thickness of 1700 m. In its central, deepest parts, the RVG has the geometry of a half-graben that is bounded in the NE by the Peel Boundary fault zone (Fig. 41b). Towards the NW and SE the RVG shallows progressively. In its SE parts, the RVG has the geometry of a symmetric graben, with the bounding fault zones having about equal throws. In the southeastern continuation of the RVRS, the main extension is accommodated in the asymmetric Erft Graben that is, however, not the direct continuation of the RVG but corresponds to a separate structural element (Geluk et al., 1994; Klett et al., 2002; Michon et al., 2003).

The RVRS started to subside during the late Oligocene under a northerly directed compressional stress regime, controlling WNW–ESE directed oblique extension across the evolving graben (Fig. 42b). At the transition to the Miocene, the compressional stress regime permutated to a NW-directed one, causing nearly orthogonal NE–SW extension across the RVRS (Fig.

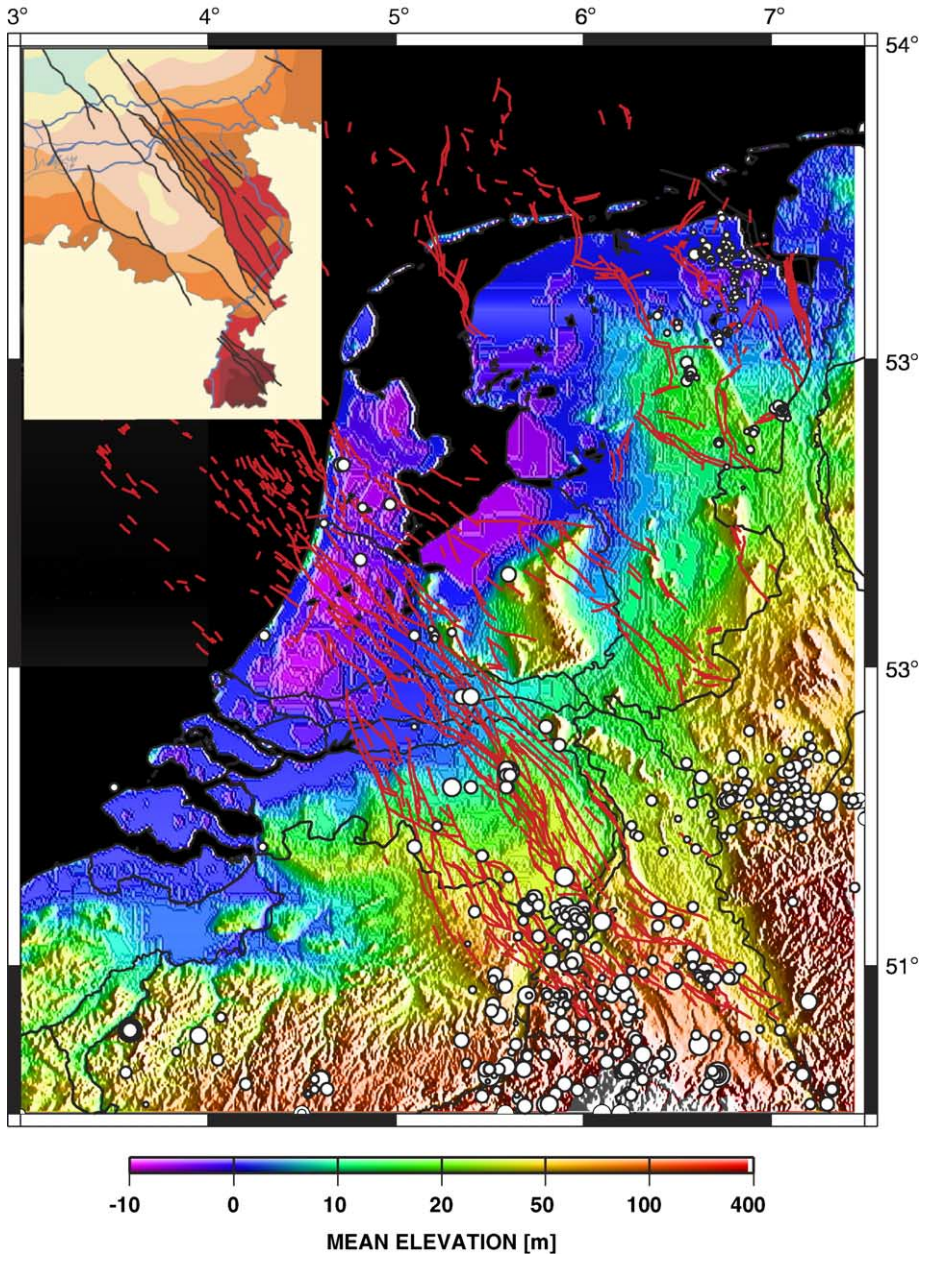

Fig. 40. Topography of The Netherlands and surroundings in a colour-coded relief map (data from GTOPO30) with superimposed base-Tertiary fault systems (red lines), based on data from TNO–NITG (Dirkzwager et al., 2000), and total seismicity (tectonic and man-induced) (data from ORFEUS data center (ORFEUS, 2004)). Inset: depth map of Base Quaternary deposits in the southeastern Netherlands (50 m depth contour interval), showing main faults that were active during the Quaternary (De Mulder et al., 2003). The depth of the Base Quaternary varies from more than 250 m below sea level (light green color) to an elevation of more than 150 m above sea level (dark brown color).

42c). This stress regime persisted until the present, although its magnitude apparently increased during the Pliocene, as evidenced by a subsidence acceleration of the RVRS. In the recent past, fault movements, some of which may have been accompanied by earthquakes, gave rise to the development of distinct fault-scarps. Some of these have been investigated in the framework of paleoseismologic research (Camelbeeck and Meghraoui, 1998; Camelbeeck et al., 2001; Houtgast et al., 2003, 2005). At present, the RVRS is seismotectonically active, and thus presents a zone of increased seismic hazard, as highlighted by the 1992 Roermond earthquake (M_L=5.8) (Fig. 41a, Plenefisch and Bonjer, 1997; Van Eck and Davenport, 1994; Hinzen, 2003).

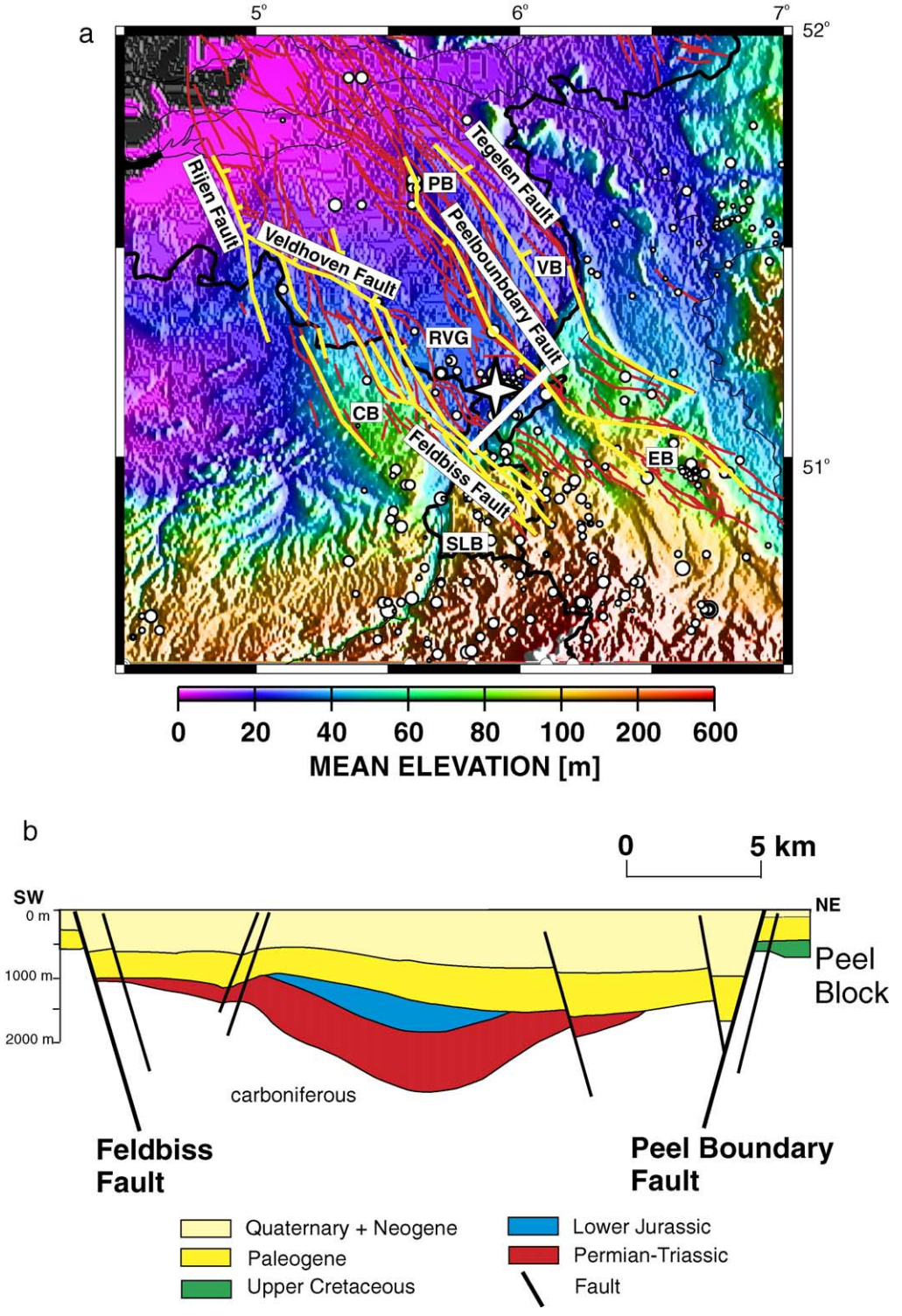

Fig. 41. (a) Topography of the Lower Rhine Graben (LRG) area in colour-coded relief map. Data are from the GTOPO30 global data set. Earthquake epicenters are from the ORFEUS data center, and are shown as white dots, with dot size indicating magnitude. White star gives the location of the 1992 M_L=5.8 Roermond earthquake. Red lines depict Base Tertiary faults, yellow lines depict Base Miocene faults. Faults are digitized from Geluk et al. (1994) and De Mulder et al. (2003). Main tectonic structures: RVG = Roer Valley Graben; PB = Peel Block; VB = Venlo Block; CB = Campine Block; EB = Erft Block; SLB = South Limburg Block; PBF = Peel Boundary Fault; FF = Feldbiss Fault. (b) Cross section through the Roer Valley Rift System (after Geluk et al., 1994). Location of profile is indicated by the white line in Fig. 41a.

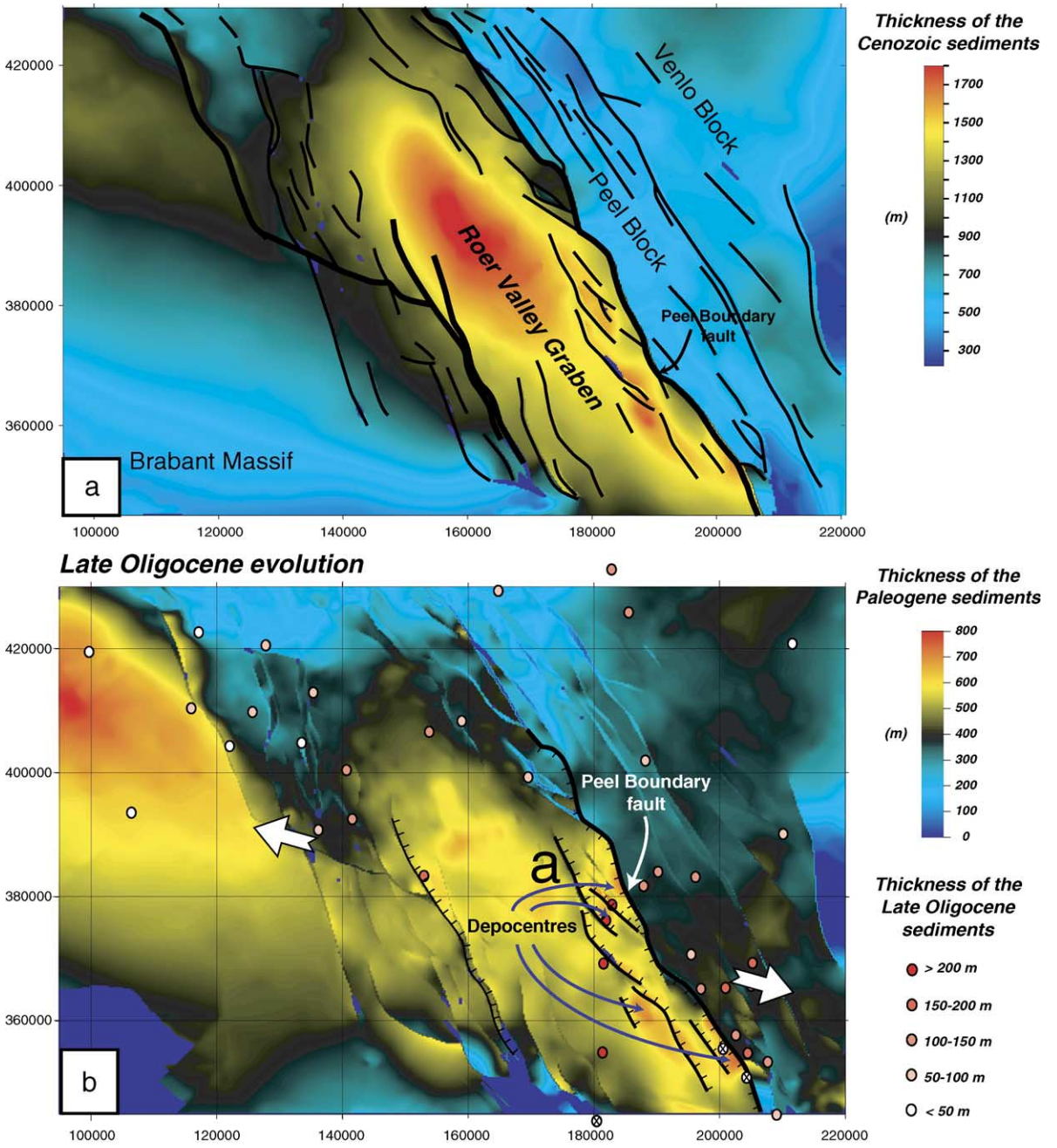

Fig. 42. (a) Base Tertiary structural map of Roer Valley Rift System (RVRS). (b) Oligocene development of the RVRS, inferred from the thickness of Late Oligocene sediments, subsidence analyses and distribution of active faults. White arrows indicate extension direction. (c) Miocene–Quaternary development of the RVRS, inferred from the thickness of Neogene sediments, subsidence analyses and distribution of active faults. White arrows indicate the extension direction.

6.2. Earthquake activity in the LRG

Since the early studies of Ahorner (1983) on seismicity and faulting in the LRG much progress has been made owing to a multidisciplinary approach that integrates German, Belgian and Dutch studies on seismicity (EUCOR-URGENT; Dost and Haak, in press; Camelbeeck et al., 1994) and high resolution digital elevation models (Cloetingh and Cornu, 2005) with the results of trenching (Houtgast et al., 2003; Meghraoui et al., 2000), high-resolution reflection-seismic data recorded on rivers (e.g. Cloetingh, 2000; Dèzes et al.,

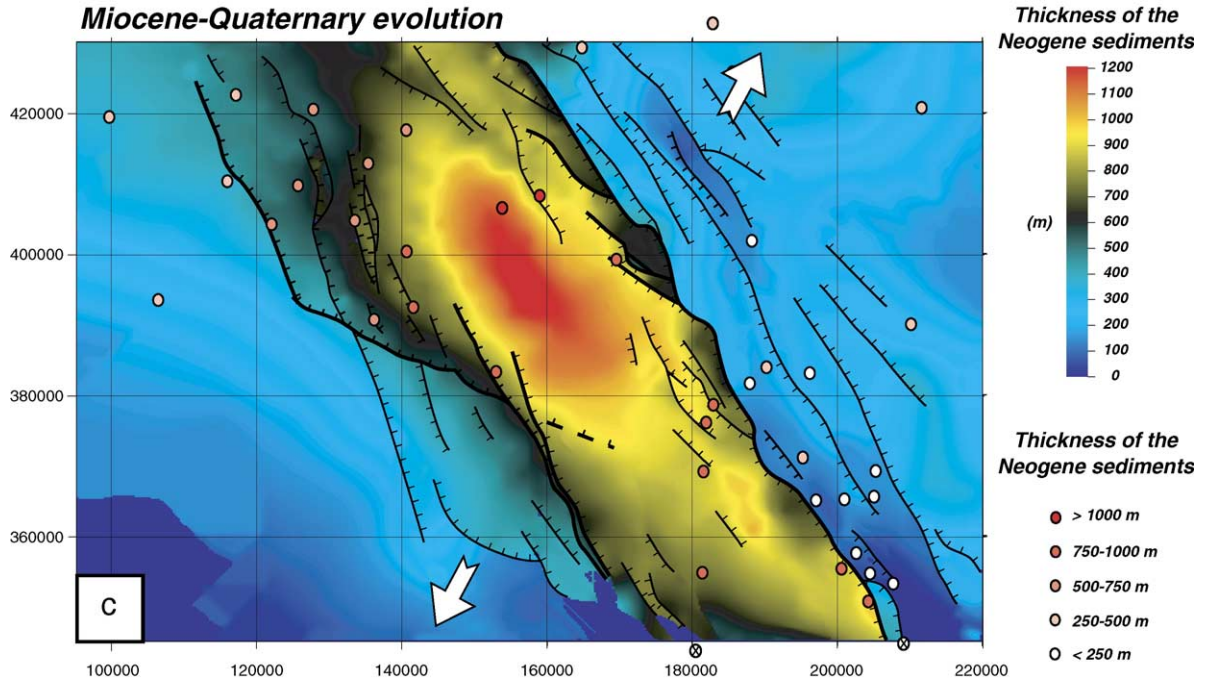

Fig. 42 (*continued*).

2004) and detailed analyses of industrial reflection-seismic and well data (Geluk et al., 1994; De Mulder et al., 2003), as well as geomechanical modeling of fault reactivation (e.g. Dirkzwager et al., 2000; Worum et al., 2004). These studies, which are based on subsurface data that were not yet available at the time Ahorner (1983) carried out his initial studies, reveal the prolongation of neotectonically active faults into the vulnerable coastal lowlands of the Netherlands (Fig. 40). These active faults largely coincide with Base Miocene faults. (Fig. 40 inset) (Geluk et al., 1994; De Mulder et al., 2003; Cloetingh et al., 2003; Worum et al., 2004; Cloetingh and Cornu, 2005).

Earthquake epicentre locations shown in Fig. 43 were extracted from the KNMI online seismicity database (http://www.knmi.nl/seismologie) that includes both natural and man-induced earthquakes. Fig. 43a illustrates that relatively large earthquakes occur in the intraplate domain of Northwest Europe. Pronounced earthquake activity occurs along the Peel Boundary fault zone that delimits the RVRS to the northeast (Fig. 43b). An example is the 1992 Roermond earthquake, that had a magnitude M_L=5.8 and a focal depth of 15 km (Camelbeeck et al., 1994).

According to Hinzen (2004), coal mining activities are responsible for part of the present-day seismic activity in the Lower Rhine Embayment and the adjacent east–west trending area coinciding with near-surface outcrops of the Variscan front (Fig. 43a, see also Fig. 6). Here, coal-bearing sedimentary strata are preserved at the rim of the Lower Rhine Embayment and in the subsurface of the adjacent central and northern Rurh Basin. As pointed out by Karg et al. (2005), Cenozoic exhumation and cooling of the Rhenish Massif appears to be an isostatic response to former erosion and major base level fall caused by subsidence in the Lower Rhine Embayment. It has been argued that the mining-induced seismic events have source depths of less than 500 m and do not involve reactivation of pre-existing deeper faults (see Hinzen, 2004). Furthermore, as pointed out by Klein et al. (1997), opencast coal mining to depths of several hundred meters may cause regional isostatic uplift in response to sediment unloading of the crust. On the other hand, withdrawal of ground water, to prevent flooding of the opencast mines, causes subsidence of the land surface.

By contrast, in the northern Netherlands natural gas extraction from Permian sandstone reservoirs (Rotliegend) at depths of some 3000 m causes gentle land subsidence (max. 45 cm up to present) that is accompanied by small earthquakes (Fig. 43a). These earthquakes, which occur at focal depths of the gas reservoir, attain M_L up to 3.5 and appear to be associated with faults both at the margins of the reservoirs (Dost and Haak, in press) as well as cutting through the reservoirs (Gussinklo et al., 2001), and thereby

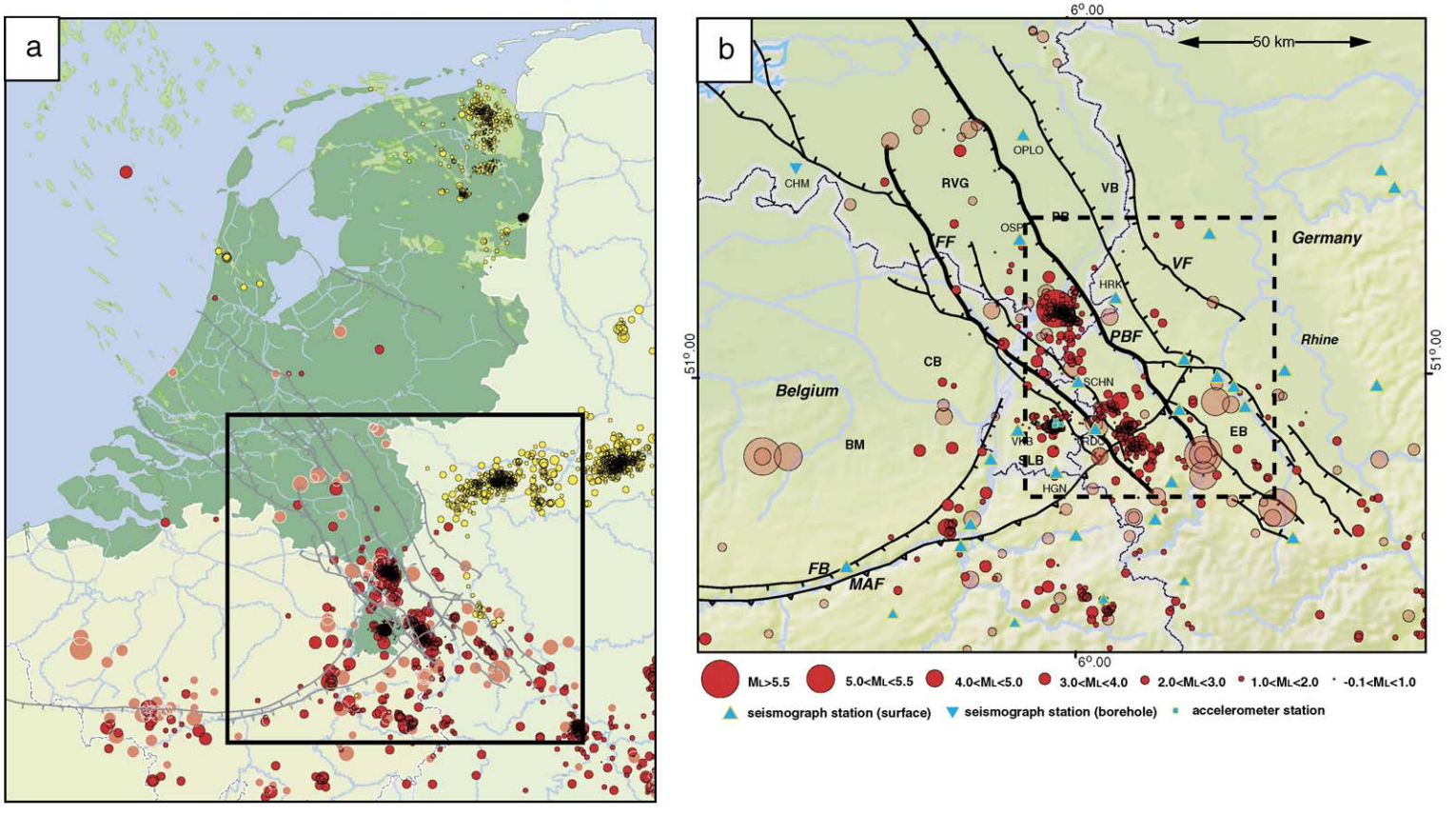

Fig. 43. (a) Distribution of seismicity since 1900 in the LRG and immediate surroundings, with red circles denoting natural seismicity and yellow circles denoting man-induced seismicity (after Van Eck et al., in press). The earthquakes are scaled according to magnitude. Gray lines indicate base-Tertiary faults. RVRS = Roer Valley Rift System; LRE = Lower Rhine Embayment; RB = Ruhr Basin; Box denotes area shown in Fig. 43b (modified after Van Eck et al., in press). (b) Epicentre map of natural seismicity in and around the Roer Valley Rift System for the period 1900–2005. Earthquakes are shown as red circles, scaled according to magnitude; events before 1980 in light red, after 1980 in dark red. Dashed box indicates area of Fig. 44. Tectonic structures: BM = Brabant Massif; RVG = Roer Valley Graben; PB = Peel Block; VB = Venlo Block; CB = Campine Block; EB = Erft Block; SLB = South Limburg Block; PBF = Peel Boundary Fault; FF = Feldbiss Fault; VF = Viersen Fault; FB = Faille Bordière; MAF = Midi-Aachen Thrust Fault (modified after Dost and Haak, in press).

may possibly affect the sealing capacity at reservoir levels. Stress relaxation induced by gas extraction-related earthquakes occurs in a pre-stressed intraplate lithospheric setting (Fig. 4; Dèzes et al., 2004). Across these pre-stressed faults, additional stresses induced by gas production-related differential reservoir pressure drawdown and associated reservoir compaction, are apparently sufficient to reduce their frictional angle to the degree that they are reactivated (Van Wees et al., 2003). There, earthquakes induced by gas extraction are controlled by the intraplate stress field. Moreover, these faults may possibly be weakened by fluid flow along them (Bense et al., 2003).

Therefore, man-induced seismicity appears to occur preferentially along pre-existing faults that can be mapped on industrial reflection-seismic data and that do not necessarily have topographic expressions (for further details see Cloetingh, 2000; Cloetingh et al., 2004; Cloetingh and Cornu, 2005).

In order to better understand the seismic activity in the area of the LRG, it is important to analyze the relationship between mapped basement faults and the distribution of natural and man-induced earthquake epicentres and focal depths (Dirkzwager et al., 2000). Obviously, in the seismotectonically active LRG, a pre-stressed crust is affected by mining-induced stresses. The tectonically active faults of the LRG, including the RVRS, extend from the Palaeozoic basement up to the surface.

Interestingly, at shallow levels these faults form barriers to groundwater flow (Bense et al., 2003; Bense and Van Balen, 2004). Their sealing capacity is controlled by a combination of aquifer offsets and clay smears, grain reorientation and iron oxide precipitation along the fault planes. In the Netherlands, sealing faults give rise to metric-scale groundwater table steps. In Germany, near Cologne, opencast brown-coal mining, to depths of several hundreds of meters, has severely affected hydraulic heads both in plan view and depth, with sealing faults accounting for large steps in hydraulic head values (Fig. 44; Bense and Van Balen, 2004).

6.3. Fault scarp analyses and displacement rates

In the RVRS, neotectonically active faults are associated with distinct fault scarps. These scarps, which are clearly visible on satellite images, topographic maps and DEM's (see Houtgast and Van Balen, 2000), have been investigated by geophysical methods and trenching in order to extent the seismic catalogue from historical times into the geological past. These studies were carried out in the framework of the PALEOSIS (e.g. Camelbeeck et al., 2000, 2001; Vanneste and Verbeeck, 2001) and NEESDI (Houtgast et al., 2003, 2005) programs. Detailed data on neotectonic fault movements during the last 30 ky are now available. Although several faulting events have been identified, based on inferred fault offsets and liquefaction structures, it is difficult to provide clear-cut evidence for distinct palaeo-seismic events (Houtgast et al., 2003, 2005). Furthermore, surface ruptures induced by earthquakes inferred from fault offsets, are not likely, given the large earthquake focal depths, and the absence of such ruptures during the 1992 Roermond earthquake. Almost all trenches show a faulting event or an increase in fault displacement rates around 10–15 ky ago. This is interpreted as reflecting the collapse of the flexural forebulge of the Weichselian ice-sheet (Houtgast et al., 2003).

The anastomosing pattern of the major fault zones of the RVRS (Figs. 41–44) has been interpreted in terms of strike-slip motions (Van den Berg et al., 2002; Camelbeeck and Meghraoui, 1998). However, careful analyses of Meuse river terrace offsets (Houtgast et al., 2002) and structural analyses of trenches across fault scarps provided only evidence for normal faulting. To resolve this controversy, a high precision DEM (5×5 m horizontal resolution, cm's vertical resolution; acquired by laser-altimetry from planes) was analyzed, in an effort to characterize and quantify neotectonic activity along the PBFZ and the FFZ. Results revealed that the morphology is clearly affected by faulting, with individual faults showing exclusively normal offsets (Fig. 45). This indicates, that neotectonic movement along the border faults of the RVRS is purely extensional with extension being NE–SW-directed, essentially normal to the graben axis. However, segmented reactivation of faults along the FFZ shows that in the Sittard area the extension direction is slight oblique (northward) to the planes of the normal faults (Houtgast et al., 2003; Michon and Van Balen, 2005). The NE–SW extension is compatible with fault-plane solutions for instrumentally recorded earthquakes (Ahorner, 1994; Plenefisch and Bonjer, 1997; Hinzen, 2003), and with the results of trenching (Houtgast et al., 2003). Quantification of offsets inferred from the high-resolution DEM, combined with age estimates for geomorphic markers, permits to determine displacement rates along individual fault segments (Michon and Van Balen, 2005). In the SE part of the RVRS, vertical displacement rates inferred for the FFZ and the PBFZ range between 55–65 mm/ky and about 65 mm/ky, respectively. By contrast, displacement rates determined for the northwestern segment of the PBFZ are

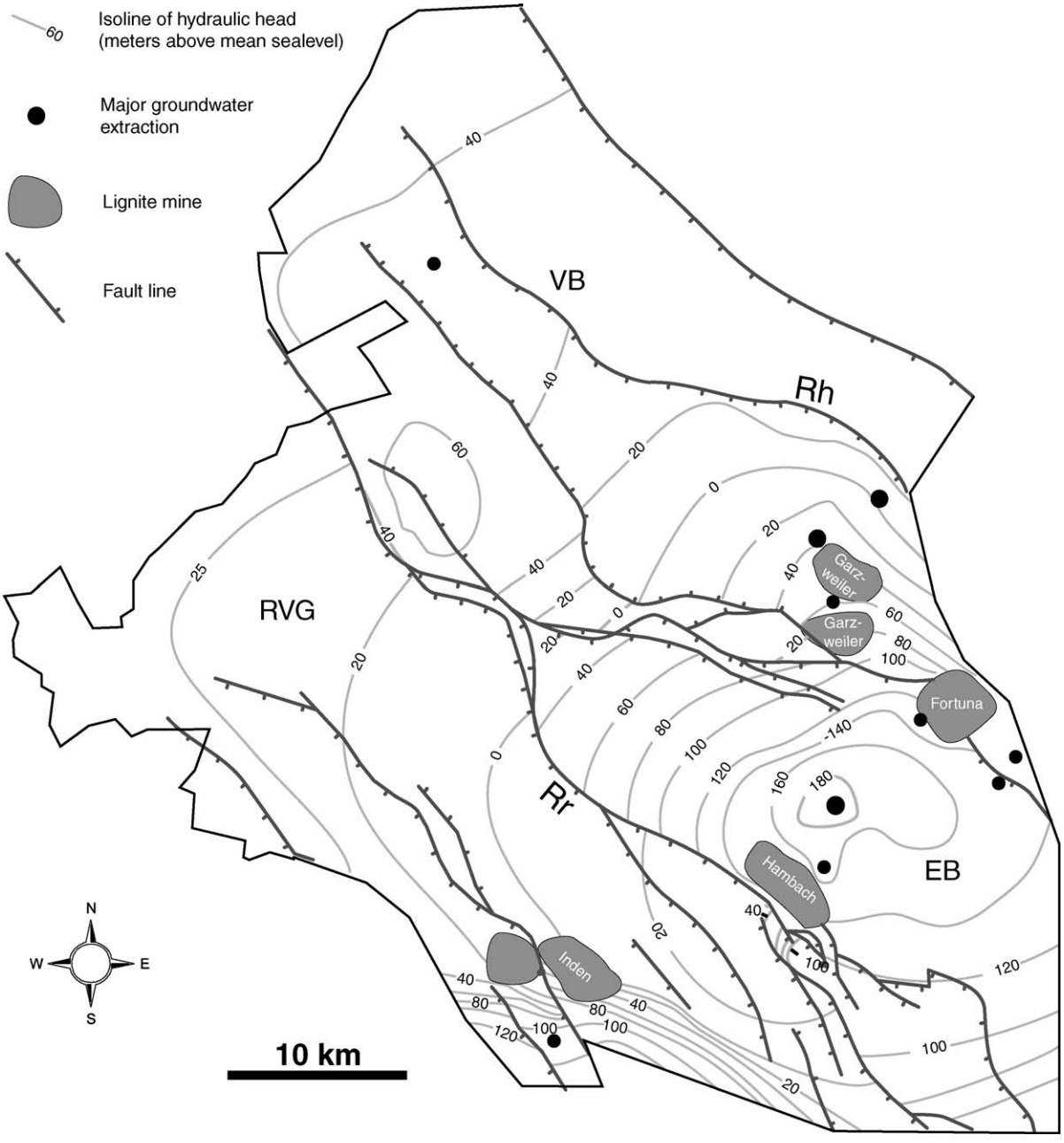

Fig. 44. Map of hydraulic head distribution in one the deeper aquifers (no. 5) of the Lower Rhine Embayment (contours in m, situation as of October 1987; after Bense and Van Balen, 2004). For location see Fig. 43b. Groundwater levels are artificially lowered to prevent flooding of opencast mines. The hydraulic head distribution clearly demonstrates the strong impact of faults on the groundwater flow system. This map is based on a dense network of groundwater observation wells that monitors the regional effects of groundwater lowering. Abbreviations: Rh = Rheindahlen Fault, Rr = Rurrand Fault, RVG = Roer Valley Graben, EB = Erft Block, VB = Venlo Block.

around 200 mm/ky. These differences between the NW and SE parts of the RVRS can be explained by the fact that the rifting style changes from a half-graben in the NW to a more or less symmetrical full graben to the SE. Thus, extensional strain is accommodated in the NW almost exclusively along the PBFZ whereas in the SE it is partitioned between the PBFZ and the FFZ. Moreover, the thickness of Neogene sediments in the NW part of the RVRS implies a larger amount of extensional strain. However, the SE part of the RVRS

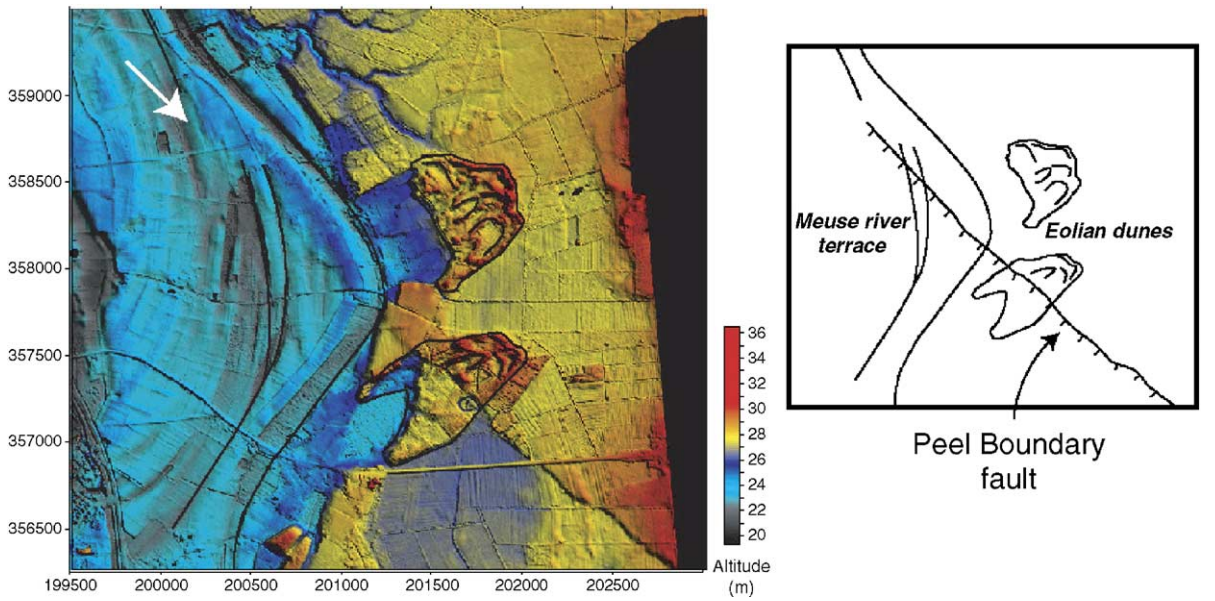

Fig. 45. Digital Elevation Model (5 m step interval) of the Peel Boundary Fault Zone (PBFZ) in the southeastern part of the RVRS (illumination from the NE). The white arrow indicates the trace NE–SW trending scarp that reflects neo-tectonic activity of the PBFZ. Note that the eolian dune is vertically offset, suggesting normal faulting only.

is marginally affected by the thermal uplift of the Rhenish Massif (Van Balen et al., 2000) that counteracted its tensional subsidence. Towards the NW, extensional strain across the RVRS progressively decreases and eventually reaches zero in the coastal areas of the Netherlands where this rift loses its identity (Worum et al., 2005). Yet, the differential subtle crustal movements have a systematic and important effect on coastal progradation and retrogradation (Fig. 46; Van Balen et al., 2005).

7. Conclusions

Using the North-Alpine foreland as a natural laboratory, the EU sponsored ENTEC network addressed the effects of neotectonics on three highly populated areas in Europe, with contributions coming from different solid Earth science disciplines, applied at various spatial and temporal scales. The three areas that were selected as specific natural laboratories are located in extensional to transtensional, neotectonically active basins that are characterized by an elevated seismic hazard potential. The rifting history of the Vienna Basin and of the Upper and Lower Rhine Graben has been extensively studied. The Vienna Basin developed during the middle Miocene as a sinistral pull-apart structure on top of the East Alpine nappe stack, whereas the Upper and Lower Rhine grabens are typical intracontinental rifts.

Whereas the Upper Rhine Graben opened during its Late Eocene and Oligocene initial rifting phase by nearly orthogonal crustal extension, its Neogene evolution was controlled by oblique extension. Lithosphere-scale tomography suggests that during extension the mantle-lithosphere was partially decoupled from the upper crust at the level of the lower crust. However, whole lithospheric folding apparently controlled the mid-Miocene to Pliocene uplift of the Vosges–Black Forest Arch, whereas thermal thinning of the mantle-lithosphere above a mantle plume contributed substantially to the past and present uplift of the Rhenish Massif.

By contrast, evolution of the Lower Rhine Graben was controlled by oblique extension during its late Oligocene initial subsidence stage and, from the transition to the Neogene onward by orthogonal extension.

The neotectonic deformation of these three natural sub-laboratories is now well documented, and various databases have been assembled. Coupled with insights gained from geodetic data, this provides for a better understanding of the kinematics controlling on-going deformation of these areas. The inventory of the different fault networks, the description of their activity and interaction, coupled with numerical modelling, clearly shows that improved seismic hazard assessment of neo-tectonically active zones requires the integration not only of major but also of minor faults.

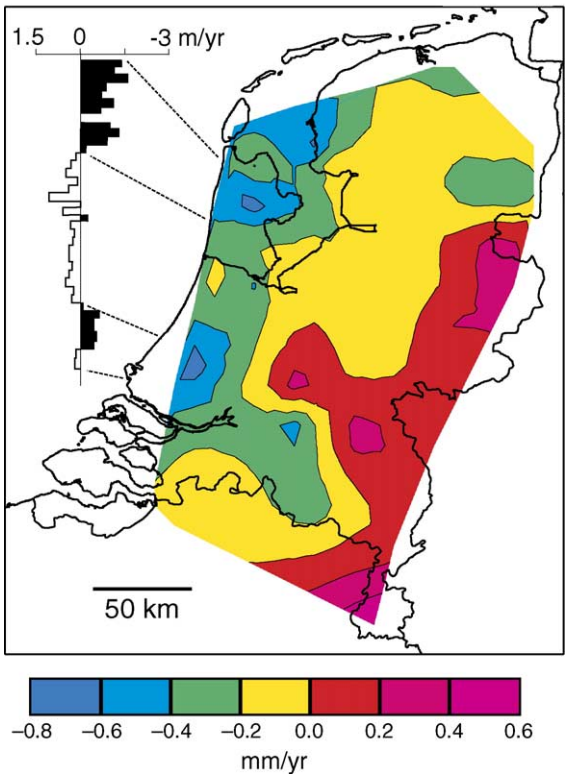

Fig. 46. Differential vertical land movement in The Netherlands during the last 100 years. The diagram on the left shows the measured coastal progradation (positive) and retrogradation velocities during the last 100 years correlated to the vertical movements (after Van Balen et al., 2005). Note the northwest–southeast trends in subsidence, coinciding with the orientation of the main fault systems of the LRG (see also Fig. 40).

Modelling shows that minor faults can have an impact on the kinematics of the major faults, or are reactivated owing to motion on major faults.

The integration of tectonic, geomorphologic and geodetic data, supported by local and regional studies, leads, step by step, toward an improved understanding of the longer and short-term deformation of a given area and the related geohazards in which the interaction between tectonics and climate change plays an important role.

Acknowledgements

Funding by the European Commission Program Improving Human Potential through contract HPRN-CT-2000-00053 to the Geosciences Training and Research Network and by Swiss grant BBW 99-0567-1 is gratefully acknowledged. ENTEC (http://www.geo.vu.nl/~entec) was developed in the context of the EUCOR-URGENT network (http://www.unibas.ch/eucor-urgent/). Rigorous reviews by A. Demoulin and an anonymous reviewer, and thoughtful comments by the Editor G. Panza are gratefully acknowledged.

Appendix A. The four-block model: calculation of the pole of rotation

In order to calculate the rotation vector (ω) of each block in which was divided the area of study, we applied Eq. (1) to each GPS point, knowing their position (r_i) and velocity (v_i):

$$\mathbf{v}_i = \omega \times \mathbf{r}_i = -\mathbf{r}_i \times \omega = \mathbf{R}_i \omega \tag{1}$$

with

$$\mathbf{R}_i = -\mathbf{R}_i^T \tag{2}$$

The position vector is:

$$\mathbf{r}_i^T = (r_{1i}, r_{2i}, r_{3i}) \tag{3}$$

and the corresponding skew symmetric matrix ($\boldsymbol{R}_i$) is:

$$\mathbf{R}_i = \begin{pmatrix} 0 & r_{3i} & -r_{2i} \\ -r_{3i} & 0 & r_{1i} \\ r_{2i} & -r_{1i} & 0 \end{pmatrix} \tag{4}$$

The observation equations can be summarised in a system in the following way:

Number of observed points: n

Number of observation equations: $3n$

Number on unknowns (ω): 3

$$\underbrace{\begin{pmatrix} \boldsymbol{v}_1 \\ \dots \\ \dots \\ \dots \\ \boldsymbol{v}_n \end{pmatrix}}_{f} = \underbrace{\begin{pmatrix} \boldsymbol{R}_1 \\ \dots \\ \dots \\ \dots \\ \boldsymbol{R}_n \end{pmatrix}}_{\mathrm{A}} \omega \tag{5}$$

Therefore, from the least-squares adjustment the rotation vector (ω) can be calculated as:

$$\omega = \left(\mathbf{A}^T \mathbf{P} \mathbf{A}\right)^{-1} \mathbf{A}^T \mathbf{P} \mathbf{f} = \mathbf{N}^{-1} \mathbf{F} \tag{6}$$

where $\boldsymbol{P}$ is the weight matrix of observations. If $\boldsymbol{P}=diag[\boldsymbol{P_1}, \boldsymbol{P_2}, \boldsymbol{P_3}, \dots, \boldsymbol{P_i}, \dots, \boldsymbol{P_n}]$, $\boldsymbol{N}$ and $\boldsymbol{F}$ can be evaluated by summing up over all points:

$$\mathbf{N} = \sum_{i=1}^{n} \mathbf{R}_i^T \mathbf{P}_i \mathbf{R}_i \tag{7}$$

$$\mathbf{F} = \sum_{i=1}^{n} \mathbf{R}_i^T \mathbf{P}_i \mathbf{v}_i \tag{8}$$

Appendix B. Numerical modeling assumptions

The following equation addresses the problem of quasi-static equilibrium and perfect contact for multi-body domain (Bittencourt and Creus, 1998). If we consider a set of bodies $\Omega_{i,i=1,N}$, the variational equality of the equilibrium equations leads to the following formulation:

$$\int_{\Omega_i} \overline{\overline{\sigma}} : \left(\frac{\partial \delta \underline{u}}{\partial \underline{X}}\right) dV = \int_{\Omega_i} \underline{f}.\delta \underline{u} dV + \int_{\partial \Omega_i^F} \overline{\overline{\sigma}}.\underline{n}.\delta \underline{u} dS + \int_{\partial \Omega_i^C} \underline{T}.\delta \underline{g} dS$$

Where $\overline{\overline{\sigma}}$ is the stress tensor, $\overline{\overline{\sigma}}.\underline{n}$ and $\underline{f}$ are the prescribed traction and body forces respectively, $\underline{T}$ is a penalty parameter which represents the contact traction on the contact border, and $\underline{\delta u}$ and $\underline{\delta g}$ are virtual variations of the displacement and gap onto contact borders vectors.

In addition, the gap function and the contact forces must verify the following conditions:

$$g(\underline{X},t) \leq 0$$

$$t_{\mathrm{n}}(\underline{X},t) 0$$

$$t_{\mathrm{n}}(\underline{X},t) g(\underline{X},t) = 0$$

where t_{n} is the normal component of the contact force (parallel to the normal vector of the contact surface).

Definition of the contact problem

The reference frame in which the contact problem is solved has first to be defined. The contact elements are extracted from the faces of the 3D elements where fault contacts occur, and define a linear contact surface. In case of brick elements, the four-node faces are split into two triangles, with a normal vector n. This definition of the contact surface has been tested in previous kinematic studies (Cornu et al., 2003) and proved to be precise enough. On each face a local rotation matrix is defined:

$$\eta = \begin{bmatrix} q_x & q_y & q_z \\ r_x & r_y & r_z \\ n_x & n_y & n_z \end{bmatrix}$$

where q and r are the tangential vector of the contact surface, normal to n.

The gap function is the normal projection of the slave node onto the target surface:

$$g(\underline{X},t) = (\underline{X}^t - \underline{X}^s).\underline{n}$$

and the contact forces are defined, onto the contact element, according to the penalty matrix and the gap vector[5]:

$$\underline{t} = \overline{\overline{k}}.\underline{g}$$

with the penalty matrix defined as: $\overline{\overline{k}} = \begin{bmatrix} k_t & 0 & 0 \\ 0 & k_t & 0 \\ 0 & 0 & k_n \end{bmatrix}$.

The normal penalty parameter k_{n} represents the stiffness of the material to penetration, and the tangential penalty parameter k_{t} the stiffness of the surface to tangential displacement.

The forces exerted on the contact surface have to be expressed in the global reference coordinate system according to the following relation:

$$\begin{Bmatrix} T_x \\ T_y \\ T_z \end{Bmatrix} = \begin{bmatrix} q_x & r_x & n_x \\ q_y & r_y & n_y \\ q_z & r_z & n_z \end{bmatrix} \begin{Bmatrix} t_q \\ t_r \\ t_n \end{Bmatrix}$$

The traction T must then be integrated over the contact element. Due to convergence requirement, it may be useful to assume that the surface area of the contact element remains constant. In this case, the considered area of contact (i.e. A^{c}) is one fourth of the area of each element that contains the contact node, and the forces applied onto A^{c} are expressed by:

$$\underline{F}^{\mathrm{c}} = \underline{T} A^{\mathrm{c}}$$

In order to increase the convergence of the Newton–Raphson algorithm used to solve the non linear problem, one has to use a tangent stiffness matrix, defined as:

$$K_{ij}^c = \eta_{ki}\eta_{lj}k_{kl}A^{\mathrm{c}}$$

The full description of the calculus needed to obtain the tangent matrix can be found in Bittencourt and Creus (1998).

Plasticity

The general elastoplastic relations are formulated in their rate form. The sign convenience of solid mechanics is used (i.e. compression is counted negative, and traction positive). The strain rate is partitioned into an elastic and plastic component:

$$\dot{\varepsilon}_{ij} = \dot{\varepsilon}_{ij}^e + \dot{\varepsilon}_{ij}^p$$

The elastic part is linked to the stress tensor following Hooke's law:

$$\dot{\sigma}_{ij} = C_{ijkl}^e \dot{\varepsilon}_{kl}^e$$

[5] In the case of perfect contact, the penalty coefficient is null for the tangential component. For the normal component an often used value is the Young's modulus of the material.

where

$$C^{e}_{ijkl} = \lambda\delta_{ik}\delta_{jl} + 2\mu\delta_{ij}\delta_{kl}$$

Here the general framework of non associated plasticity is considered, meaning the rate of plastic flow is assumed perpendicular to a plastic potential g.

$$\dot{\varepsilon}^{p}_{ij} = \dot{\lambda}\frac{\partial g}{\partial \sigma_{ij}}$$

In the previous equation, the plastic potential g is defined in a similar way as the yield surface, but assuming zero cohesion. Combining the definition of strain and plastic flow gives:

$$\dot{\varepsilon}_{ij} = \dot{\varepsilon}^{e}_{ij} + \dot{\lambda}\frac{\partial g}{\partial \sigma_{ij}}$$

To define the yield surface f, the Drucker–Prager (DP) criterion is preferred to the Mohr–Coulomb (MC) criterion. The DP is an alternative to the MC and proposes a linear relationship between the first invariant of the stress tensor and the second invariant of the deviatoric stress tensor:

$$f = II_{\hat{\sigma}} + mI_{\sigma} - k = 0$$

Identification of the parameters m and k and the Mohr–Coulomb envelop as a function of the internal parameters c (cohesion) and ϕ (friction angle) leads to:

$$m = \frac{2\sin\phi}{\sqrt{3}(3-\sin\phi)}$$

$$k = \frac{6c\cos\phi}{\sqrt{3}(3-\sin\phi)}$$

Then the DP criterion becomes:

$$f = II_{\hat{\sigma}} + m\left(I_{\sigma} - \frac{3c}{\tan\phi}\right) = 0$$

If we now express the plastic potential g by analogy to the yield function f:

$$g = II\hat{\sigma} + m'I_{\sigma} = 0$$

with

$$m' = \frac{2\sin\psi}{\sqrt{3}(3-\sin\psi)}$$

where ψ is the dilatancy angle.

The general rate constitutive elastoplastic relation is then solved with a "return mapping algorithm"[6] (Ortiz and Simo, 1986).

[6] For a perfectly plastic surface as the DP, the yield criterion is reached after one iteration. In the general case, as the MC, several iterations are required to obtain a state of stress that satisfies the yield criterion "f=0" (Barnichon, 1998).

References

Ahorner, L., 1975. Present-day stress field and seismotectonic block movements along major fault zones in central Europe. Tectonophysics 29, 233–249.

Ahorner, L., 1983. Historical seismicity and present-day microearthquake activity of the Rhenish Massif, Central Europe. In: Fuchs, K., v. Gehlen, K., v. Mälzer, K., Murawski, H., Semmel, A. (Eds.), Plateau Uplift, the Rhenish Shield — A Case History. Springer, Berlin, pp. 198–221.

Ahorner, L., 1994. Fault-plane solutions and source parameters of the 1992 Roermond, the Netherlands, mainshock and its stronger aftershocks from regional seismic data. Neth. J. Geosci. 73, 119–214.

Aichroth, B., Prodehl, C., Thybo, H., 1992. Crustal structure along the central segment of the EGT from seismic-refraction studies. Tectonophysics 207, 43–64.

Altamimi, Z., Sillard, P., Boucher, C., 2002. ITRF2000: a new release of the international terrestrial reference frame for earth science applications. J. Geophys. Res. 107, 1–19.

Aric, K., Gutdeutsch, R., 1981. Seismotectonic and refraction seismic investigation in the border region between the Eastern Alps and the Pannonian Basin. Pure Appl. Geophys. 119, 1125–1133.

Artemieva, I.M., Mooney, W.D., 2001. Thermal thickness and evolution of Precambrian lithosphere. A global study. J. Geophys. Res. 106, 16387–16414.

Artemieva, I.M., Thybo, H., Kaban, M.K., in press. Deep Europe today: Geophysical synthesis of upper mantle structure and lithospheric processes over 3.5 Ga. In: Gee, D. and Stephenson, R.A. (Eds.), European Lithosphere Dynamics. Geol. Soc., London, Memoir.

Babuska, V., Plomerova, J., 1992. The lithosphere in central Europe — seismological and petrological aspects. Tectonophysics 207, 141–163.

Babuska, V., Plomerova, J., 1993. Lithospheric thickness and velocity anisotropy — seismological and geothermal aspects. Tectonophysics 225, 79–89.

Babuska, V., Plomerova, J., 2001. Subcrustal lithosphere around the Saxothuringian–Modanubian Suture Zone — a model derived from anisotropy of seismic wave velocities. Tectonophysics 332, 185–199.

Bada, G., Horvath, F., Cloetingh, S., Coblentz, D.D., Toth, T., 2001. Role of topography-induced gravitational stresses in basin inversion: the case study of the Pannonian Basin. Tectonics 20, 343–363.

Barnichon, J.D., 1998. Finite element modelling in structural and petroleum geology. Ph.D. thesis, University of Liège.

Bayer, U., Scheck, M., Rabbel, W., Krawczyk, C.M., Gotze, H.-J., Stiller, M., Beilecke, Th., Marotta, A.-M., Barrio-Alvers, L., Kuder, J., 1999. An integrated study of the NE German Basin. Tectonophysics 314, 285–307.

Becker, A., 2000. The Jura Mountains — an active foreland fold-and-thrust belt? Tectonophysics 321, 381–406.

Behrmann, J., Hermann, O., Horstmann, M., Tanner, D., Bertrand, G., 2003. Anatomy and kinematics of oblique continental rifting revealed: a 3D case study of the SE Upper Rhine Graben (Germany). AAPG Bull. 87, 1–17.

Behrmann, J.H., Ziegler, P.A., Schmid, S.M., Heck, B., Granet, M. (Eds.), 2005. EUCOR-URGENT Upper Rhine Graben evolution and neotectonics, Int. J. Earth Sci., vol. 94, pp. 505–778.

Bense, V., Van Balen, R.T., 2004. The effect of fault relay and clay smearing on groundwater flow patterns in the Lower Rhine Embayment. Basin Res. 16, 397–411.

Bense, V., Van Balen, R.T., De Vries, J., 2003. The impact of faults on hydrogeological conditions in the southeastern part of the Netherlands. Neth. J. Geosci. 82, 41–54.

Bergerat, F., 1977. La fracturation de l'avant-pay Jurassien entre la fossé de la Saône et du Rhin, analyse et essai d'interpretation dynamique. Rev. Géogr. Phys. Géol. Dyn. (2) XIX (4), 325–338.

Bergerat, F., 1987. Stress fields in the European Platform at the time of Africa–Eurasia collision. Tectonics 6, 99–132.

Bertrand, G., Horstmann, M., Hermann, O., Behrmann, J.H., 2005. 3D inverse modeling of the southern Upper Rhine Graben: new insights on continental oblique rifting. Quat. Sci. Rev. 24, 345–352.

Beutler, G., Bock, H., Brockmann, E., Dach, P., Fridez, P., Gurtner, W., Hugentobler, U., Ineichen, D., Johnson, J., Meindl, M., Mervart, L., Rothacher, M., Schaer, S., Springer, T., Weber, R., 2001. In: Hugentobler, U., Shaer, S., Fridez, P. (Eds.), Bernese GPS Software Version 4.2. Astronomical Institute, University of Berne.

Bittencourt, E., Creus, G.J., 1998. Finite element analysis of three-dimensional contact and impact in large deformation problems. Comput. Struct. 69, 219–234.

Blundell, D., Mueller, S., Friedman, R. (Eds.), 1992. A Continent Revealed. The European Geotraverse. Cambridge University Press.

Bonjer, K.-P., 1997. Seismicity pattern and style of seismic faulting at the eastern border fault of the Southern Rhine Graben. Tectonophysics 275, 41–69.

Bonnet, S., Guillocheau, F., Brun, J.-P., 1998. Relative uplift measured using river incisions: the case of the Armorican Basement (France). C. R. Acad. Sci. Paris, Earth. Planet. Sci. 327, 245–251.

Bonnet, S., Guillocheau, F., Brun, J.-P., van Den Driessche, J., 2000. Large scale relief development related to Quaternary tectonic uplift of a Proterozoic–Paleozoic basement: the Armorican Massif, NW France. J. Geophys. Res. 105, 19273–19288.

Brockmann, E., Grunig, S., Schneider, D., Wiget, A., Wild, U., 2001. Introduction and first applications of a real time precise positioning service using the Swiss Permanent Network 'AGNES.' National report of Switzerland. In: Torres, J.A., Hornik, H. (Eds.), Subcommission for the European Reference Frame (EUREF), Dubrovnik.

Brockmann, E., Hug, R., Signer, T., 2002. Geotectonics in the Swiss Alps using GPS. In: Torres, J.A., Hornik, H. (Eds.), Subcommission for the European Reference Frame (EUREF), EUREF Publication, vol. 11.

Brockmann, E., Grünig, S., Schneider, D., Wiget, A., Wild, U., 2002. Applications of the real-time Swiss GPS permanent network AGNES. Proceedings of the EGS XXVII General Assembly Nice, 21–26 April 2002, Session 9 on Evolving Space Geodesy Techniques, Physics and Chemistry of the Earth.

Brun, J.P., Dekorp-Ecors team, 1992. Deep crustal structure of the Rhine Graben from DEKORP-ECORS seismic reflection data: a summary. Tectonophysics 208, 139–147.

Brune, J.N., 1968. Seismic moment, seismicity, and rate of slip along major fault zones. J. Geophys. Res. 73, 777–784.

Brüstle, A., 2002. Morphostructural analyses in the region of Freiburg i. Br. (Upper Rhine Graben). University of Koln, Msc. Thesis.

Brüstle, A., Nivière, B., Bertrand, G., Gourry, J.-C., Carretier, S., Fracassi, U., Winter, T., 2003. Evidence of Pleistocene tectonic deformation along the SE border of the Upper Rhine Graben (Freiburg area, Germany). Geophys. Res. Abstr. 5, 05410.

Buchner, F., 1981. Rhinegraben: horizontal stylolites indicating stress regimes of earlier stages of rifting. Tectonophysics 73, 113–118.

Burov, E.B., Diament, M., 1995. The effective elastic thickness (T_e) of continental lithosphere: what does it really mean? J. Geophys. Res. 100, 3905–3927.

Calais, E., Gallison, L., Stephan, J.-F., Delteil, J., Deverchere, J., Larroque, C., Mercier de Lepinay, B., Popoff, M., Sosson, M., 2000. Crustal strain in the Southern Alps, France, 1948–1998. Tectonophysics 319, 1–17.

Calais, E., Noquet, J.-M., Jouanne, F., Tardy, M., 2002. Current strain regime in the Western Alps from continuous Global Positioning System measurements, 1996–2001. Geology 30, 651–654.

Calcagnile, G., Panza, G.F., 1987. Properties of the lithosphere–asthenosphere system in Europe with a view toward Earth conductivity. Pure Appl. Geophys. 125, 241–254.

Camelbeeck, T., Meghraoui, M., 1998. Geological and geophysical evidence for large paleo-earthquakes with surface faulting in the Roer Graben (northwest Europe). Geophys. J. Int. 132, 347–362.

Camelbeeck, T., Van Eck, T., Pelzing, R., Ahorner, A., Loohuis, J., Haak, H.W., Hoang-Trong, P., Hollnack, D., 1994. The 1992 Roermond earthquake, Netherlands, and its aftershocks. Geol. Mijnb. 73, 181–197.

Camelbeeck, T., Alexander, P., Vanneste, K., Meghraoui, M., 2000. Long term seismicity in regions of present day low seismic activity: the example of western Europe. Soil Dyn. Earthqu. Eng. 20, 405–414.

Camelbeeck, T., Martin, H., Vanneste, K., Verbeeck, K., Meghraoui, M., 2001. Morphometric analysis of active normal faulting in slow-deformation areas; examples of the Lower Rhine Embayment. Neth. J. Geosc. 80, 95–107.

Carretier, S., 2000. Cycle sismique et surrection de la chaine de Gurvan Bogd (Mongolie). Approche de la géomorphologie quantitative. Ph.D. thesis, Universite Montpellier 2.

Carretier, S., Lucazeau, F., Ritz, J.-F., 1998. Approche numérique des interactions entre climat, tectonique et erosion. Exemple de la faille de Bogd, Mongolie. C. R. Acad. Sci. 326, 1–7.

Carter, N.L., Tsenn, M.C., 1987. Flow properties of continental lithosphere. Tectonophysics 136, 27–63.

Cloetingh, S. (Ed.), 2000. Environmental Tectonics and Climate: NEESDI. Global Planet. Change, vol. 27, pp. 1–263.

Cloetingh, S., Burov, E.B., 1996. Thermomechanical structure of European continental lithosphere: constraints from rheological profiles and EET estimates. Geophys. J. Int. 124, 695–723.

Cloetingh, S., Cornu, T. (Eds.), 2005. Neotectonics and Quaternary fault reactivation in the Alpine foreland: an integrated approach. Quat. Sci. Rev., vol. 24, pp. 235–508.

Cloetingh, S., Ben-Avraham, Z., Sassi, W., Horvath, F. (Eds.), 2005. Dynamics of Extensional Basins and Inversion Tectonics, Tectonophysics, vol. 266, pp. 1–523.

Cloetingh, S., Boldreel, L.O., Larsen, B.T., Heinesen, M., Mortensen, L. (Eds.), 1998. Tectonics of sedimentary basin formation: models and constraints. The Ziegler Volume. Tectonophysics, vol. 300, pp. 1–387.

Cloetingh, S., Burov, E., Poliakov, A., 1999. Lithospheric folding: primary response to compression, from Central Asia to the Paris Basin. Tectonics 18, 1064–1083.

Cloetingh, S., Ziegler, P.A., ENTEC Working Group, 2003. Investigating environmental tectonics in the northern Alpine foreland of Europe. Eos, Trans. AGU 84, 349, 356–357.

Cloetingh, S., Ziegler, P.A., ENTEC Working Group, 2004. Reply to comments on investigating environmental tectonics in the north-

ern Alpine foreland of Europe. Eos, Trans., Am. Geophys. Union 85, 322.
Cornu, T., Bertrand, G., 2005a. Numerical backward and forward modelling of the Southern Upper Rhine Graben (France–Germany border): new insight on tectonic evolution of an intracontinental rift. Quat. Sci. Rev. 24, 353–362.
Cornu, T., Bertrand, G., 2005b. Backward modelling of the rifting kinematics in the Upper Rhine Graben: insights from an elastic-perfect contact law on the restoration of a multi-block domain. Int. J. Earth Sci. 94, 751–757. doi:10.1007/s00531-004-0452-1.
Cornu, T., Schneider, F., Gratier, J.-P., 2003. 3D discrete kinematic modelling applied to extensional and compressional tectonics. In: Nieuwland, D.A. (Ed.), New insights into structural interpretation and modelling. Geol. Soc., London, Spec. Pub., vol. 212, pp. 275–284.
Decker, K., Peresson, H., 1996. Tertiary kinematics in the Alpine–Carpathian–Pannonian system; links between thrusting, transform faulting and crustal extension. In: Wessely, G., Liebl, W. (Eds.), Oil and Gas in Alpidic Thrustbelts and Basins of Central and Eastern Europe. Spec. Publ. European Assoc. Petrol. Geosc., vol. 5, pp. 69–77.
Decker, K., Peresson, H., 1998. Miocene to present-day tectonics of the Vienna Basin transform fault. Links Between the Alps and the Carpathians, XVI Congress of the Carpathian–Balkan Geological Association. Geologische Bundesanstalt, Vienna, Austria, pp. 33–36.
Decker, K., Peresson, H., Hinsch, R., 2005. Active tectonics and Quaternary basin formation along the Vienna Basin Transfer fault. Quat. Sci. Rev. 24, 305–320.
Delouis, B., Haessler, H., Cisternas, A., Rivera, L., 1993. Stress tensor determination in France and neighbouring regions. Tectonophysics 221, 413–438.
Demoulin, A., 1998. Testing the tectonic significance of some parameters of longitudinal river profiles: the case of the Ardennes (Belgium, NW Europe). Geomorphology 24, 189–208.
Demoulin, A., 2004. Reconciling geodetic and geological rates of vertical crustal motion in intraplate regions. Earth Planet. Sci. Lett. 221, 91–101.
Demoulin, A., Pissart, A., Zippelt, K., 1995. Neotectonic activity in and around the Southwestern Rhenish Shield (West Germany): indications of a Levelling Comparison. Tectonophysics 249, 203–216.
De Mulder, E.F.J., Geluk, M.C., Ritsema, I., Westerhoff, W.E., Wong, T.E., 2003. The subsurface of the Netherlands. Netherlands Institute for Applied Geosciences — TNO, p. 379.
Dèzes, P., Ziegler, P.A., 2004. Moho depth map of Western and Central Europe. EUCOR-URGENT home page (http://www.unibas.ch/eucor-urgent).
Dèzes, P., Schmid, S.M., Ziegler, P.A., 2004. Evolution of the European Cenozoic rift system: interaction of the Alpine and Pyrenean orogens with their foreland lithosphere. Tectonophysics 389, 1–33.
Dirkzwager, J.B., Van Wees, J.D., Cloetingh, S., Geluk, M.C., Dost, B., Beekman, F., 2000. Geo-mechanical and rheological modelling of upper crustal faults and their near surface expression in the Netherlands. Glob. Planet. Change 27, 67–88.
Dost, B., Haak, H.W., in press. Seismicity. In: Wong, T., et al. (Eds.), Geology of the Netherlands.
Du, Z.J., Michelini, A., Panza, G.F., 1998. EurID, a regionalized 3-D seismological model of Europe. Phys. Earth Planet. Inter. 105, 31–62.
EUCOR-URGENT: http://comp1.geol.unibas.ch/.
Eva, E., Solarino, S., 1998. Variations of stress directions in the western Alpine arc. Geophys. J. Int. 135, 438–448.
Eva, E., Solarino, S., Eva, C., Neri, G., 1997. Stress tensor orientation derived from fault plane solutions in the southwestern Alps. J. Geophys. Res. 102 (B4), 8171–8185.
Eva, E., Pastore, S., Deichmann, N., 1998. Evidence for ongoing extensional deformation in the western Swiss Alps and thrust-faulting in the southwestern Alpine Foreland. J. Geodyn. 26, 27–43.
Gangl, G., 1975. Seismotektonische Untersuchungen am Alpenostrand. Mitt. Geol. Ges. Wien 1973–1974 (66–67), 33–48.
Garcia-Castellanos, D., Cloetingh, S., van Balen, R.T., 2000. Modelling the middle Pleistocene uplift in the Ardennes–Rhenisch Massif: thermo-mechanical weakening under the Eifel? Glob. Planet. Change 27, 39–52.
Geiger, A., 2003. Präzisionsnavigation. Lecture Notes Geomatics, ETH Zürich.
Geluk, M.C., Duin, E.J.T., Dusar, M., Rijkers, R.H.B., van den Berg, M.W., van Rooijen, P., 1994. Stratigraphy and tectonics of the Roer Valley Graben. Geol. Mijnb. 73, 129–141.
Giamboni, M., Ustaszewski, K., Schmid, S.M., Schumacher, M.E., Wetzel, A., 2004. Plio–Pleistocene transpressional reactivation of Paleozoic and Paleogene structures in the Rhine–Bresse transform zone (Northern Switzerland and Eastern France). Int. J. Earth Sci. 93, 207–223. doi:10.1007/s00531-003-0375-2.
Goes, S., Govers, R., Vachez, P., 2000a. Shallow upper mantle temperatures under Europe from P- and S-wave tomography. J. Geophys. Res. 105, 11153–11169.
Goes, S., Loohuis, J.J.P., Wortel, M.J.R., Govers, R., 2000b. The effect of plate stresses and shallow mantle temperatures on tectonics of northwestern Europe. Glob. Planet. Change 27, 23–38.
Gorshkov, A.I., Kuznetsov, I.V., Panza, G.F., Sololiev, A.A., 2000. Identification of future earthquake sources in the Carpatho-Balkan orogenic belt using morphostructural criteria. Pure Appl. Geophys. 157, 79–95.
Gorshkov, A.I., Panza, G.F., Sololiev, A.A., Aoudia, A., 2004. Identification of seismogenic nodes in the Alps and Dinarides. Boll. Soc. Geol. Ital. 123, 3–18.
Gourry, J.C., Nivière, B., Winter, T., 2001. Coupling of high-resolution electromagnetic and electrical methods for slow active faults detection in temperate environment (Upper Rhine Graben, France). Stephan Mueller Topical Conference of the European Geophysical Society, 22–26 September 2001, Balatonfuered, Hungary.
Granet, M., Wilson, M., Achauer, U., 1995. Imaging mantle plumes beneath the French Massif Central. Earth Planet. Sci. Lett. 136, 199–203.
Grenerczy, G., Kenyeres, A., Fejes, I., 2000. Present crustal movement and strain distribution in Central Europe inferred from GPS measurements. J. Geophys. Res. 105 (B9), 21835–21846.
Guggisberg, B., Kaminski, W., Prodehl, C., 1991. Crustal structure of the Fennoscandian Shield: a traveltime interpretation of the long-range Fennolora seismic refraction profile. Tectonophysics 195, 105–137.
Gussinklo, H.J., Haak, H.W., Quadvlieg, R.C.H., Schutjens, P.M.F.M., 2001. Subsidence, tremors and society. Neth. J. Geosci. 80, 121–136.
Gutdeutsch, R., Aric, K., 1988. Seismicity and neotectonics of the East Alpine–Carpathian and Pannonian Area. In: Royden, L.H., Horvath, F. (Eds.), The Pannonian Basin: A Study in Basin Evolution. AAPG Memoir, vol. 45, pp. 183–194.

Hanks, T.C., Kanamori, H., 1979. A moment magnitude scale. J. Geophys. Res. 84 (B5), 2348–2350.
Hinsch, R., Decker, K., 2003. Do seismic slip deficits indicate an underestimated earthquake potential along the Vienna Basin Transfer Fault System? Terra Nova 15, 343–349.
Hinsch, R., Decker, K., Peresson, H., 2005a. 3-D seismic interpretation and structural modeling in the Vienna Basin; implications for Miocene to recent kinematics. Austr. J. Earth Sci. 97, 38–50.
Hinsch, R., Decker, K., Wagreich, M., 2005b. 3-D mapping of segmented active faults in the southern Vienna Basin. Quat. Sci. Rev. 24, 321–336.
Hinzen, K.G., 2003. Stress field in the Northern Rhine area, Central Europe, from earthquake fault plane solutions. Tectonophysics 377, 325–356.
Hinzen, K., 2004. Investigating environmental tectonics in northern Alpine Foreland of Europe; discussion. Eos, Trans., Am. Geophys. Union 85, 318–322.
Holt, W.E., Chamot-Rooke, N., Le Pichon, X., Haines, A.J., Sheng-Tu, B., Ren, J., 2000. Velocity field in Asia inferred from Quaternary fault slip rates and Global Positioning System observations. J. Geophys. Res. 105 (B8), 19185–19209.
Houtgast, R.F., Van Balen, R.T., 2000. Neotectonics of the Roer Valley Rift System, the Netherlands. Glob. Planet. Change 27, 131–146.
Houtgast, R.F., Van Balen, R.T., Bouwer, L.M., Brand, G.B.M., Brijker, J.M., 2002. Late Quaternary activity of the Feldbiss Fault zone, Roer Valley Rift System, based on displaced fluvial terrace fragments. Tectonophysics 352, 295–315.
Houtgast, R.F., van Balen, R.T., Kasse, C., Vandenberge, J., 2003. Late Quaternary tectonic evolution and postseismic near surface fault displacements along the Geelen Fault (Feldbiss Fault Zone–Roer Valley Rift System, the Netherlands), based on trenching. Neth. J. Geosci. 82, 177–196.
Houtgast, R.F., Van Balen, R.T., Kasse, C., 2005. Late Quaternary tectonic evolution of the Feldbiss Fault. Quat. Sci. Rev. 24, 489–508.
Judenherc, S., Granet, M., Boumbar, N., 1999. Two dimensional anisotropic tomography of lithosphere beneath France using regional arrival times. J. Geophys. Res. 104, 13,201–13,215.
Kahle, H.-G., Cocard, M., Peter, Y., Geiger, A., Reilinger, R., Barka, A., Veis, G., 2000. GPS-derived strain field within the boundary zones of the Eurasian, African, and Arabian Plates. J. Geophys. Res. 105, 23,353–23,370.
Kaikkonen, P., Moisio, K., Heeremans, M., 2000. Thermomechanical lithospheric structure of the central Fennoscandian Shield. Phys. Earth Planet. Inter. 119, 209–235.
Karg, H., Carter, A., Brix, M.R., Littke, R., 2005. Late- and post-Variscan cooling and exhumation history of the northern Rhenish Massif and the southern Ruhr Basin: new constraints from fission-track analysis. Int. J. Earth Sci. 94, 180–192. doi:10.1007/s00531-005-0467-2.
Kastrup, U., 2002. Seismotectonics and stress field variations in Switzerland. Ph.D. thesis, 14527, ETH Zürich.
Kastrup, U., Zoback, M.L., Deichmann, N., Evans, K.F., Giardini, D., Andrew, J.M., 2004. Stress field variations in the Swiss Alps and the northern Alpine foreland derived from inversion of fault plane solutions. J. Geophys. Res. 109 (B1), B01402.
Klein, A., Jacoby, W., Smilde, P., 1997. Mining-induced crustal deformation in northwest Germany: modelling the rheological structure of the lithosphere. Earth Planet. Sci. Lett. 147, 107–123.
Klett, M., Eichhorst, F., Schäfer, A., 2002. Facies interpretation from well logs applied to the Tertiary Lower Rhine Basin fill. Neth. J. Geosci. 81, 167–176.
Kraus, M., Möbus, G., 1981. Korrelation zwischen der Tektonik des Untergrunds und den geomorphologischen Verhältnissen im Bereich der Ostsee. Z. Geol. Wiss. 9, 255–267.
Lagarde, J.L., Baize, S., Amorese, D., Delcaillau, B., Laville, E., 2000. Active tectonics, seismicity and geomorphology with special references to Normandy (France). J. Quat. Sci. 15, 745–758.
Lambert, J., Winter, T., Dewez, T.J.B., Sabourault, P., 2005. New hypotheses on the maximum damage area of the 1356 Basel earthquake (Switzerland). Quat. Sci. Rev. 24, 381–399.
Lankreijer, A.C., Bielik, M., Cloetingh, S., Majcin, D., 1999. Rheology predictions across the Western Carpathians, Bohemian Massif and the Pannonian basin: implications for tectonic scenarios. Tectonics 18, 1064–1083.
Larroque, J., Laurent, P., 1988. Evolution of the stress field pattern in the south of the Rhine Graben from the Eocene to the present. Tectonophysics 148, 41–58.
Larroque, J.M., Etchecopar, A., Philip, H., 1987. Evidence for the permutation of stresses s1 and s2 in the Alpine foreland: the example of the Rhine graben. Tectonophysics 144, 315–322.
Laubscher, H., 1992. Jura kinematics and the Molasse Basin. Eclogae Geol. Helv. 85, 653–675.
Linzer, H.-G., Moser, F., Nemes, F., Ratschbacher, L., Sperner, B., 1997. Build-up and dismembering of the eastern Northern Calcareous Alps. Tectonophysics 272, 97–124.
Linzer, H.-G., Decker, K., Peresson, H., Dell'Mour, R., Frisch, W., 2002. Balancing lateral orogenic float of the Eastern Alps. Tectonophysics 354, 211–237.
Lopes Cardozo, G., 2004. 3-D geophysical imaging and tectonic modelling of the active tectonics of the Upper Rhine Region. Ph.D. thesis Vrije Universiteit Amsterdam, 163 pp.
Lopes Cardozo, G., Granet, M., 2003. New insight in the tectonics of the Upper Rhine Graben–Jura region using local earthquake seismology. Tectonics 22, 1078.
Lopes Cardozo, G., Granet, M., 2005. A multi-scale approach to study the lithospheric structure of the southern Upper Rhine Graben; from seismic tomography through reflection seismics to surface geology. Int. J. Earth Sci. 94, 615–620. doi:10.1007/s00531-005-0476-1.
Lopes Cardozo, G., Granet, M., Edel, J.B., 2005. Detection of active crustal structures in the Upper Rhine Graben using Gravimetry and Local Earthquake Tomography. Quat. Sci. Rev. 24, 337–344.
Ludwig, A.O., 1995. The surface of the Holsteinian interglacial sediments as a base level for reconstruction of vertical neotectonic movements in Northern Germany. Tech. Poszuk. Geol., Geosynoptica Geoterm. 3, 31–36.
Marsch, F., Wessely, G., Sackmaier, W., 1990. Borehole-breakouts as geological indications of crustal tension in the Vienna Basin. In: Rossmanith, P. (Ed.), Mechanics of Jointed and Faulted Rock. A.A. Balkema, Rotterdam, pp. 113–120.
Meghraoui, M., Camelbeeck, T., Vanneste, K., Brondeel, M., Jongmans, D., 2000. Active faulting and paleoseismology along the Bree fault zone, Lower Rhine Graben (Belgium). J. Geophys. Res. 105, 13809–13841.
Meghraoui, M., Delouis, B., Ferry, M., Giardini, D., Huggenberger, P., Spottke, I., 2001. Active normal faulting in the Upper Rhine Graben and paleoseismic identification of the 1356 Basel earthquake. Science 293, 2070–2073.

Mengel, K., Sachs, P.M., Stosch, H.G., Wörner, G., Look, G., 1991. Crustal xenoliths from Cenozoic volcanic fields of West Germany: implications for structure and composition of the continental crust. Tectonophysics 195, 271–289.

Meyer, W., Stets, J., 1998. Junge tectonik im Rheinishe Schiefergebirge und ihre Quantifizierung. Z. Geol. Ges. 149, 359–379.

Meyer, B., Lacassin, R., Brulhet, J., Mouroux, B., 1994. The Basel 1356 earthquake: which fault produced it? Terra Nova 6, 54–63.

McKenzie, D.P., 1978. Some remarks on the development of sedimentary basins. Earth Planet. Sci. Lett. 40, 25–32.

Michon, L., Van Balen, R.T., 2005. Characterization and quantification of active faulting in the Roer Valley Rift system based on high precision digital elevation models. Quat. Sci. Rev. 24, 455–472.

Michon, L., Van Balen, R.T., Merle, O., Pagnier, H., 2003. The Cenozoic evolution of the Roer Valley rift system integrated at a European scale. Tectonophysics 367, 101–126.

Mosar, J., 2003. Scandinavia's North Atlantic passive margin. J. Geophys. Res. 108, 2360. doi:10.1029/2002JB002134.

Mueller, S., 1968. Geophysical aspects of Graben Formation. In: Illies, J.H., Mueller, S. (Eds.), Continental Rift Systems. Graben Problems, pp. 27–37.

Müller, W.H., Blümling, P., Becker, A., Clauss, B., 1987. Die Entkoppelung des tektonischen Spannungsfeldes an der Jura-Überschiebung. Eclogae Geol. Helv. 80, 473–489.

Müller, B., Zoback, M.L., Fuchs, K., Mastin, L., Gregersen, S., et al., 1992. Regional patterns of tectonic stress in Europe. J. Geophys. Res. 97, 11783–11803.

Müller, W.H., Naef, H., Graf, H.R. (Eds.), 2002. Geologische Entwicklung der Nordschweiz, Neotektonik und Langzeitszenarien, Zürcher Weinland. NAGRA Technischer Bericht, 99-08. NAGRA, Wettingen. 226 pp.

NEIC, 2004. National Earthquake Information Center, http://neic.usgs.gov/.

Nicolas, M., Santoire, J.P., Delpech, P.Y., 1990. Intraplate seismicity: new seismotectonic data in Western Europe. Tectonophysics 179, 27–53.

Nivière, B., Winter, T., 2000. Pleistocene northwards fold propagation of the Jura within the southern Upper Rhine Graben: seismotectonic implications. Glob. Planet. Change 27, 263–288.

Nocquet, J.-M., Calais, E., 2003. Crustal velocity field of western Europe from permanent GPS array solutions, 1996–2001. Geophys. J. Int. 154, 72–88.

ORFEUS, 2004. Observatories and Research Facilities for EUropean Seismology, http://orfeus.knmi.nl/.

Ortiz, M., Simo, J.C., 1986. An analysis of a new class of integration algorithms for elastoplastic constitutive relations. Int. J. Numer. Methods Eng. 23, 353–366.

Panza, G.F., 1983. Lateral variations in the European lithosphere and seismic activity. Phys. Earth Planet. Inter. 33, 194–197.

Peresan, A., Panza, G.F., Gorshkov, A.I., Aoudia, A., 2002. Pattern recognition methodologies and deterministic evaluation of seismic hazard: a strategy to increase earthquake preparedness. Boll. Soc. Geol. Ital. 1, 37–46.

Philippe, Y., Colletta, B., Deville, E., Mascle, A., 1996. The Jura fold-and-thrust belt: a kinematic model based on map-balancing. In: Ziegler, P.A., Horvàth, F. (Eds.), Structure and Prospects of Alpine Basins and Forelands. Peri-Tethys Mem. 2, Mém. Mus. natn. Hist. nat., Paris, vol. 170, pp. 235–261.

Plenefisch, T., Bonjer, K., 1997. The stress field in the Rhine Graben area inferred from earthquake focal mechanisms and estimation of frictional parameters. Tectonophysics 275, 71–97.

Plomerova, J., Kouba, D., Babuska, V., 2002. Mapping the lithosphere–asthenosphere boundary through changes in surface-wave anisotropy. Tectonophysics 358, 175–185.

Prodehl, C., Müller, St., Haak, V., 1995. The European Cenozoic rift system. In: Olsen, K.H. (Ed.), Continental Rifts: Evolution, Structures, Tectonics. Developments in Geotechnics vol. 25. Elsevier, Amsterdam, pp. 133–212.

Purcaru, G., Berckhemer, H., 1978. A magnitude scale for very large earthquakes. Tectonophysics 49, 189–198.

Ranalli, G., 1995. Rheology of the Earth. (2nd ed.)Chapman and Hall, London.

Ranalli, G., Murphy, D.C., 1987. Rheological stratification of the lithosphere. Tectonophysics 132, 281–295.

Ratschbacher, L., Frisch, W., Linzer, H.-G., Merle, O., 1991. Lateral extrusion in the Eastern Alps. Tectonics 10, 257–271.

Reinecker, J., 2000. Stress and Deformation: Miocene to Present-Day Tectonics in the Eastern Alps, Tübinger Geowissenschaftliche Arbeiten; Reihe A: Geologie, Paläontologie, Stratigraphie. Institut und Museum für Geologie und Paläontologie der Universität Tübingen, Tübingen, 128.

Reinecker, J., Lenhardt, W., 1999. Present-day stress field and deformation in eastern Austria. Int. J. Earth Sci. 88, 532–550.

Ritter, J.R.R., Achauer, U., Christensen, U.R., 2000. The teleseismic tomography experiment in the Eifel region, central Europe: design and first results. Seismol. Res. Lett. 71, 437–443.

Ritter, J.R.R., Jordan, M., Christensen, U.R., Achauer, U., 2001. A mantle plume below the Eifel Volcanic fields, Germany. Earth Planet. Sci. Lett. 186, 7–14.

Royden, L.H., 1988. Late Cenozoic tectonics of the Pannonian Basin system. In: Royden, L.H., Horvath, F. (Eds.), The Pannonian Basin: A Study in Basin Evolution. AAPG Memoir, vol. 45, pp. 27–48.

Royden, L.H., Horvath, F., Rumpler, J., 1983. Evolution of the Pannonian Basin System. Tectonics 2, 63–90.

Rosza, S., Heck, B., Mayer, M., Seitz, K., Westerhaus, M., Zippelt, K., 2005. Determination of displacements in the Upper Rhine Graben area from GPS and levelling data. Int. J. Earth Sci. 94, 538–549. doi:10.1007/s00531-005-0478-z.

Scholz, C.H., 1998. Earthquakes and friction laws. Nature 391, 37–42.

Scholz, C.H., 2002. The Mechanics of Earthquakes and Faulting. Cambridge Univ. Press, Cambridge, United Kingdom, 471 pp.

Schumacher, M.E., 2002. Upper Rhine Graben: role of preexisting structures during rift evolution. Tectonics 21, 1006. doi:10.1029/2001TC900022.

Sintubin, M., Vandycke, S., Camelbeek, T. (Eds.), 1999. Paleozoic to recent tectonics in the NW European Variscan front zone. Tectonophysics, vol. 309, pp. 1–277.

Sittler, C., 1969. Le fosse Rhenan en Alsace: aspect structural et histoire geologique. Rev. Géogr. Phys. Géol. Dyn., 2 XI, fasc. 5, 465–494.

Straub, Ch., 1996. Recent crustal deformation and strain in the Marmara Sea region, NW Anatolia inferred from GPS Measurements. Ph.D. thesis, ETH Zürich.

Sue, C., Tricart, P., 2003. Neogene to ongoing normal faulting in the inner western Alps: a major evolution of the late Alpine tectonics. Tectonics 22, 1–25.

Sue, C., Thouvenot, F., Frechet, J., Tricart, P., 1999. Widespread extension in the core of the western Alps revealed by earthquake analysis. J. Geophys. Res. 104, 25,611–25,622.

Suhadolc, P., Panza, G.F., 1989. Physical properties of the lithosphere–asthenosphere system in Europe from geophysical data. In: Boriani, A., Bonafede, M., Piccardo, G.B., Vai, G.B. (Eds.), The lithosphere in Italy — advances in earth science research. Acad. Naz. Lincei, vol. 80, pp. 15–40.

Tesauro, M., Hollenstein, C., Egli, R., Geiger, A., Kahle, H.-G., 2005. CGPS and broad-scale deformation across the Rhine Graben and the Alps. Int. J. Earth Sci. 94, 525–537. doi:10.1007/s00531-004-0453-0.

Ustaszewski, K., Schumacher, M.E., Schmid, S.M., 2005a. Contemporaneous faulting and extensional flexuring during Palaeogene rifting — a case study from the southern Upper Rhine Graben. Int. J. Earth Sci. 94, 680–696. doi:10.1007/s00531-004-0454-z.

Ustaszewski, K., Schumacher, M.E., Schmid, S.M., Nieuwland, D., 2005b. Fault reactivation in brittle-viscous wrench systems — dynamically scaled analogue models and application to the Rhine–Bresse Transfer Zone. Quat. Sci. Rev. 24, 363–380.

Van Balen, R.T., Houtgast, R.F., van der Wateren, F.M., Vandenberghe, J., Bogaart, P.W., 2000. Sediment budget and tectonic evolution of the Meuse catchment in the Ardennes and the Roer Valley Rift System. Glob. Planet. Change 27, 113–129.

Van Balen, R.T., Houtgast, R.F., Cloetingh, S.A.P.L., 2005. Neotectonics of the Netherlands. Quat. Sci. Rev. 24, 439–454.

Van den Berg, M.W., Vanneste, K., Dost, B., Lokhorst, A., Van Eijk, M., Verbeeck, K., 2002. Paleoseismological investigations along the Peel Boundary Fault: geological setting, site selection and trenching results. Geol. Mijnb. 81, 39–60.

Van Eck, T., Davenport, C., 1994. Seismotectonics and seismic hazard in the Roer Valley Graben; with emphasis on the Roermond earthquake of April 13, 1992. Geol. Mijnb. 73, 91–92.

Van Eck, T., Goutbeek, F., Haak, H., Dost, B., in press. Seismic hazard due to small shallow induced earthquakes. Engin. Seism.

Van Vliet-Lanoë, B., Laurent, M., Everaerts, M., Mansy, J.-L., Manby, G., 2000. Evolution Neogene et quaternaire de la Somme, une flexuration tectonique active. C. R. Acad. Sci. Paris 331, 151–158.

Vanneste, K., Verbeeck, K., 2001. Paleoseismological analysis of the Rurrand fault near Jülich, Roer Valley Graben, Germany: coseismic or aseismic history? Neth. J. Geosci. 80, 155–169.

Van Wees, J.-D., Cloetingh, S., 1996. 3D flexure and intraplate compression in the North Sea Basin. Tectonophysics 266, 343–359.

Van Wees, J.-D., Orlic, B., Van Eijs, R., Zijl, W., Jongerius, P., Schreppers, G.J., Hendriks, M., Cornu, T., 2003. Integrated 3D geomechanical modelling for deep subsurface deformation: a case study of tectonic and human-induced deformation in the eastern Netherlands. In: Nieuwland, D.A. (Ed.), New Insights into Structural Interpretation and Modelling. Geol. Soc., London, Spec. Publ., vol. 212, pp. 313–328.

Vigny, C., Chery, J., Duquesnoy, T., Jouanne, F., Amman, J., Ansdei, M., Avouac, J.-P., Barlier, F., Bayer, R., Briole, P., Calais, E., Cotton, F., Duquenne, F., Feigl, K.L., Ferhat, G., Flouzat, M., Gamond, J.-F., Geiger, A., Harmel, A., Kasser, M., Laplanche, M., Le Pape, M., Martinod, J., Menard, G., Meyer, B., Ruegg, J.-C., Scheubbel, J.-M., Scotti, O., Vidal, G., 2002. GPS network monitors the Western Alps' deformation over a five-year period: 1993–1998. J. Geod. 76, 63–76.

Villemin, Th., Alvarez, F., Angelier, J., 1986. The Rhinegraben: extension, subsidence and shoulder uplift. Tectonophysics 128, 47–59.

Wenzel, F., Brun, J.-P., ECORS-DECORP working group, 1991. A deep reflection seismic line across the Northern Rhine Graben. Earth Planet. Sci. Lett. 104, 140–150.

Wernicke, B., 1981. Low angle normal faults in basin and range province. Nappe tectonics in an extending orogen. Nature 291, 645–648.

Wessely, G., 1993. Geologischer Tiefbau Wiener Becken — Molasse Niederösterreichs. In: Brix, F., Schulz, O. (Eds.), Erdöl und Erdgas in Österreich, Vienna (Naturhistor. Museum).

Wilson, M., Patterson, R., 2001. Intraplate magmatism related to short-wavelength convective instabilities in the upper mantle: evidence from the Tertiary–Quaternary volcanic province of western and central Europe. Spec. Pap. - Geol. Soc. Am. 352, 37–58.

Wittenberg, A., Vellmer, C., Kern, H., Mengel, K., 2000. The Variscan lower continental crust: evidence for crustal delamination from geochemical and petrological investigations. In: Franke, W., Haak, V., Oncken, O., Tanner, D. (Eds.), Orogenic Processes: Quantification and Modelling in the Variscan Belt. Geol. Soc., London, Spec. Publ., vol. 179, pp. 401–414.

World Stress Map, 2004. http://www.world-stress-map.org/.

Worum, G., Van Wees, J.-D., Bada, G., Van Balen, R.T., Cloetingh, S., Pagnier, H., 2004. Slip tendency analysis as a tool to constrain fault reactivation: a numerical approach applied to three-dimensional fault models in the Roer Valley rift system (southeast Netherlands). J. Geophys. Res. 109, B02401. doi:10.1029/2003JB002586.

Worum, G., Michon, L., van Balen, R.T., van Wees, J.-D., Cloetingh, S., Pagnier, H., 2005. Comparison and Modelling of the present day fault activity in the west Netherlands Basin and Roer Valley Rift System (southern Netherlands) in light of their pre-Neogene evolution. Quat. Sci. Rev. 24, 473–488.

ZAMG, 2001. Earthquake catalogue of felt earthquakes (Austria). Computer File. Central Institute of Meteorology and Geodynamics (ZAMG), Vienna Austria.

Ziegler, P.A., 1988. Evolution of the Arctic–North Atlantic and the Western Tethys. Am. Assoc. Pet. Geol. Mem. 43, 198 pp.

Ziegler, P., 1990. Geological Atlas of Western and Central Europe. Geol. Soc. Publ. House, 2nd edition.

Ziegler, P.A., 1994. Cenozoic rift system of Western and Central Europe: an overview. Geol. Mijnb. 73, 99–127.

Ziegler, P.A., Cloetingh, S., van Wees, J.D., 1995. Geodynamics of intraplate compressional basin deformation: the Alpine foreland and other examples. Tectonophysics 252, 7–59.

Ziegler, P.A., van Wees, J.-D., Cloetingh, S., 1998. Mechanical controls on collision-related compressional intraplate deformation. Tectonophysics 300, 103–129.

Ziegler, P.A., Cloetingh, S., Guiraud, R., Stampfli, G.M., 2001. Peri-Tethyan platforms: constraints on dynamics of rifting and basin inversion. In: Ziegler, P.A., Cavazza, W., Robertson, A.H.F., Crasquin-Soleau, S. (Eds.), Peri-Thetys Mem. 6: Peri-Thetyan Rift/Wrench Basins and Passive Margins. Mem. Mus. Natl. Hist. Nat, Paris, vol. 186, pp. 9–49.

Ziegler, P.A., Bertotti, G., Cloetingh, S., 2002. Dynamic processes controlling foreland deformation: the role of mechanical (de)coupling of orogenic wedges and forelands. EGU Stephan Mueller Spec. Publ., vol. 1, pp. 29–91.

Ziegler, P.A., Schumacher, M.E., Dèzes, P., van Wees, J.D., Cloetingh, S., 2004. Post-Variscan evolution of the lithosphere in the Rhine Graben area: constraints from subsidence modelling. In: Wilson, B.M. (Ed.), Permo–Carboniferous Magmatism and Rifting in Europe. Geol. Soc., London, Spec. Publ., vol. 223, pp. 289–317.

Zimmer, W., Wessely, G., 1996. Exploration results in thrust and subthrust complexes in the Alps and below the Vienna Basin in Austria. In: Wessely, G., Liebl, W. (Eds.), Oil and Gas in Alpidic Thrustbelts and Basins of Central and Eastern Europe.

Special Publication of the European Assoc. Petrol. Geosci., vol. 5, pp. 81–107.
Zijerveld, L., Stephenson, R., Cloetingh, S., Duin, E., van den Berg, M.W., 1992. Subsidence analysis and modelling of the Roer Valley Graben (SE Netherlands). Tectonophysics 208, 159–171.
Zippelt, K., 1988. Modellbildung, Berechnungsstrategie und Beurteilung von Vertikalbewegungen unter Verwendung von Prazisionsnivellements. DGK Reihe C, Heft, Nr., vol. 343.
Zoback, M.L., Burke, K., 1993. Lithospheric stress patterns: a global view. EOS, Trans. Am. Geophys. Union 74, 609–618.